THERMODYNAMIC ANALYSIS OF MINERALS FROM CERRO GALAN AND CERRO BLANCO, NW ARGENTINA

by

JOAO CARLOS LUNA GONZALEZ

(Under the Direction of ALBERTO PATINO DOUCE)

ABSTRACT

Cerro Galan and Cerro Blanco are two large Plio-Pleistocene calderas from the Andes of NW Argentina located within 120 km of each other. Large ash flows erupted from both volcanoes are relatively-well preserved and minimally eroded. Multiple sections of ignimbrites from both volcanoes were sampled and form the basis of this study. Their mineralogical assemblage— biotite + plagioclase + sanidine + Fe-Ti oxides + quartz + apatite—makes them well suited for the estimation of pre-eruptive intensive variables (temperature, pressure) in large silicic sub-volcanic magma chambers. The presence of minerals that incorporate F, Cl, and OH such as apatite and biotite also makes them ideal for studying the relationship between these fluids species as function of vertical location and temperature within the pre-eruptive magma chamber. Results indicate both calderas were at a minimum pressure of 2 kbar based on an equilibrium temperature of about 700 ^{0}C and 4% H_2O saturation.

INDEX WORDS: Cerro Galan, Cerro Blanco, Feldspar thermometry, Fe-Ti oxides, Halogens, Thermodynamics

THERMODYNAMIC ANALYSIS OF MINERALS FROM CERRO GALAN AND CERRO BLANCO, NW ARGENTINA

by

JOAO CARLOS LUNA GONZALEZ

B.S., Barry University, 2010

A Thesis Submitted to the Graduate Faculty of The University of Georgia in Partial Fulfillment of the Requirements for the Degree

MASTER OF SCIENCE

ATHENS, GEORGIA

2013

THERMODYNAMIC ANALYSIS OF MINERALS FROM CERRO GALAN AND CERRO BLANCO, NW ARGENTINA

by

JOAO CARLOS LUNA GONZALEZ

Major Professor:	ALBERTO PATINO
Committee:	DOUG CROWE
	MICHAEL RODEN

Electronic Version Approved:

Maureen Grasso
Dean of the Graduate School
The University of Georgia
May 2013

DEDICATION

This thesis is dedicated to my family and fiancée Hannah James for the constant support and words of encouragement. I would like to specially thank my father Ignacio Luna for his unwavering support and words of wisdom.

ACKNOWLEDGEMENTS

I would like to acknowledge my advisor Alberto Patino Douce for all the help and guidance he has provided me during my graduate career. Thank you for your patience and for pushing me to become a better scientist. I would also like to acknowledge my committee members Doug Crowe and Michael Roden for their input on my research. Chris Fleisher is thanked for his help with microprobe analyses.

TABLE OF CONTENTS

Page

CHAPTER

LIST OF TABLES

Page

LIST OF FIGURES

Page

CHAPTER 1

Introduction

Previous Work: Cerro Galan

Cerro Galan is a large volcanic complex in the Altiplano-Puna plateau of northwest Argentina and has been the focus of numerous studies. Some of the early workers include Sparks et al. (1985) and Francis et al. (1989). Sparks et al. (1985) were pioneers in identifying, describing, dating, and petrologically characterizing the numerous ignimbrites of the Galan complex. Francis et al. (1989) were among the first investigators to emphasize geochemical studies in order to elucidate the mechanism by which the Cerro Galan complex was developed. Francis et al. (1989) concluded that the Cerro Galan caldera complex represents the development of a cordilleran plutonic complex in the Andean crust. They assert that basaltic magma provided the heat for triggering melting in the crust at mid to deep levels. Furthermore, they claimed that magma mixing generated the formation of the characteristic dacitic magmas erupted at Cerro Galan.

Recent investigators include Folkes et al. (2011) who building on the work of Francis et al. (1989) further emphasized the importance of crustal assimilation in the generation of the Cerro Galan ignimbrites. With the use of thermodynamics and traditional geochemical investigations Folkes et al. (2011) concluded that magma generation in the Galan complex comes from two sources within the crust. This was inferred from mineral barometry, geothermometry, and major and trace element analyses of 2 types of pumice clasts—which they term as white and grey—found in the Cerro Galan ignimbrite. They assert that the white pumice clasts equilibrated in the upper 10 km of the crust (<3 kbar), while the grey pumice clasts originated from a deeper (up to 18 km in the crust), hotter source than the white pumice magma. Furthermore, building on the work of Hildreth and Moorbath (as cited in Skewes and Sterns, 1995) this investigation proposes the existence of a lower-crustal MASH (melting, assimilation, storage, and homogenization) in the Cerro Galan system, where magmas are geochemically buffered (this buffering is a consequence of parental magmas being delivered to shallow crustal levels where MASH occurs prior to eruption), producing the underlying geochemical and isotopic signatures that characterize the compositionally similar ignimbrites in the Galan complex.

Another important recent study is that of Cas et al. (2011) who characterized the flow dynamics and eruption style of the latest ignimbrite—the Cerro Galan ignimbrite (CGI)—of the Cerro Galan complex as a low ‘boiling over’, fountain style eruption, with a relatively constant, sustained and high discharge rate. This investigation has important implications for post-emplacement magmatic processes including alteration and re-equilibration of mineral compositions. If the Cerro Galan and Cerro Blanco ignimbrites were not quenched effectively after eruption then minerals in these ash flow deposits may have altered. If this was the case then compositions of these minerals would not be useful for inferring conditions of the magma chambers prior to eruption.

Previous Work: Halogens applied to Cerro Galan

Other studies which have influenced this investigation are those of Boyce and Hervig (2008) and Patino Douce and Roden (2006). Boyce and Hervig (2008) showed that OH and Cl growth zonation in apatite grains recorded a multistage magmatic history before eruption. Based on apatite growth rates, they attributed the zoning profiles to H_2O degassing and recharge less than 400 days prior to eruption. Similarly, Patino Douce and Roden (2006) demonstrate the utility of apatite as a probe for F, Cl, and OH volatiles in magmatic systems. These workers demonstrated the importance of using apatite equilibria in conjunction with other minerals –in this case merrillite—in order to calculate halogen and water fugacities in planetary magmas. Merrillite is not present in Cerro Galan or Cerro Blanco however the thermodynamic concepts utilized in the previously described study can be applied to the apatite-biotite phase equilibria in order to elucidate pre-eruptive conditions in the sub-volcanic magma chambers.

Purpose of Investigation

No previous studies have tried to use volatile compositions (halogens and water) in conjunction with thermodynamic calculations in order to elucidate the pre-eruptive magma conditions in the silicic magma chambers of Cerro Galan and Cerro Blanco. This investigation sought to estimate pressure, temperature, and volatile budget (F, Cl, and OH) in both calderas as a function of vertical location within the magma chambers in order to infer possible correlations and differences in the evolution of the individual magma chambers. To this end, compositions of apatite, biotite, Fe-Ti oxides, and feldspars (plagioclase and alkali-feldspar) were chosen from a mineral assemblage in both calderas consisting of plagioclase, sanidine, Fe-Ti oxides, biotite, quartz, apatite, and rare zircon.

An attempt was made to use Fe-Ti oxides and feldspars as geothermometers in order to track the evolution of the Cerro Galan and Cerro Blanco magma chambers. Compositions of the iron-titanium oxide pairs magnetite (Fe_3O_4)–ulvospinel (Fe_2TiO_4) and ilmenite ($FeTiO_3$)–hematite (Fe_2O_3), present in both ashflows, were utilized as geothermometers. Thermodynamic calculations were performed to estimate the equilibrium temperature of coexisting oxide solutions in order to determine the pre-eruptive temperatures of Cerro Galan and Cerro Blanco magma chambers. Feldspar thermometry was used as an independent method for the determination of equilibrium temperatures in the magmatic chambers of Cerro Galan and Cerro Blanco. A minimum pressure of 2 kb was inferred based on an equilibrium temperature of about 700 ^{0}C and 4% H_2O saturation in both magma chambers (refer to chapter on feldspar thermometry).

Background information

Altiplano-Puna Plateau

The Altiplano-Puna Plateau of the Central Andes is the highest plateau in the world associated with arc magmatism, and it is second only to the Tibetan plateau in height and extent (Folkes et al. 2011; Allmendinger 1997). The plateau stretches for 1800 km along the central Andes and has widths ranging from 350 to 450 km as depicted in fig.1.1 from Allmendinger (1997).

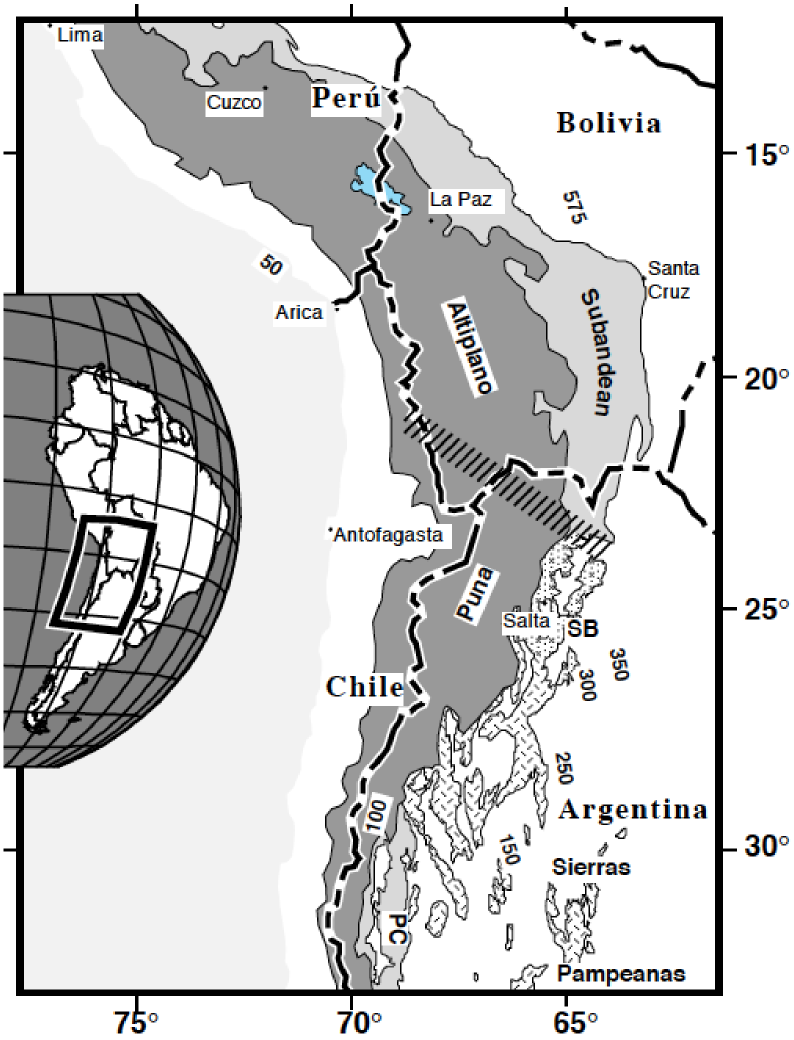

Fig.1.1. Location map showing the extent of the high plateau of the Central Andes. Dark gray shows areas above 3km elevation; the plateau is defined by the wide area above 3km between 13 and 27 ^{0}S (modified from Allmendingger 1997).

This geologic structure can be divided into two main segments: Altiplano of Bolivia and the Puna of northwest Argentina and adjoining parts of Chile, which differ in topography, and magmatism. It is generally accepted that a major episode of plateau uplift—which ultimately led to its current appearance—started sometime between 15 and 20 Ma (Francis and Hawkesworth 1994; Allmendinger 1997). This plateau correlates in time and space to Andean arc magmatism but it was formed mainly thru crustal shortening (70-80 %) with a subordinate portion associated with magmatism (Allmendinger, 1994;

Isacks, 1988). In order to accommodate this non-collisional plateau (not formed from continent-continent collision like the Tibetan Plateau) crustal thickening from 40 to 65 km and thermal thinning of the lithosphere from 140 to 70 km had to occur in order to form the 4-km-high plateau (Isacks 1988).

Magmatism

There are 4 areas of volcanism in the Andean cordillera: the northern zone in Ecuador and Colombia (5^0 N-2^0 S), the central zone (also known as the Central Volcanic Zone or CVZ) in Chile, Peru, Bolivia, and northernmost Argentina (16-28^0 S), and southern and austral zones in southernmost Chile (33-52^0 S). Cerro Galan and Cerro Blanco are located in the CVZ, which is underlain by exceptionally thick crust up to 70 km (Francis and Hawkesworth, 1994).

As pointed out by Francis and Hawkesworth (1994), the CVZ—focus of this study—presents three distinct components of volcanism: a well-defined zone of calc-alkaline andesite volcanism that defines the classical Andean cordillera; a volumetrically insignificant scatter of calk-alkaline, high-K and shoshonitic (potassic trachyandesite, composed of olivine, augite and plagioclase phenocrysts in a groundmass with calcic plagioclase and sanidine and some dark-colored volcanic glass) back-arc volcanoes; and a diffuse zone of voluminous silicic volcanism, characterized by ignimbrite-erupting calderas such as Cerro Galan and Cerro Blanco, NW Argentina. Figure 1.2 below is a schematic cross section from Francis and Hawkesworth (1994) that shows the three distinct volcanic components in the CVZ.

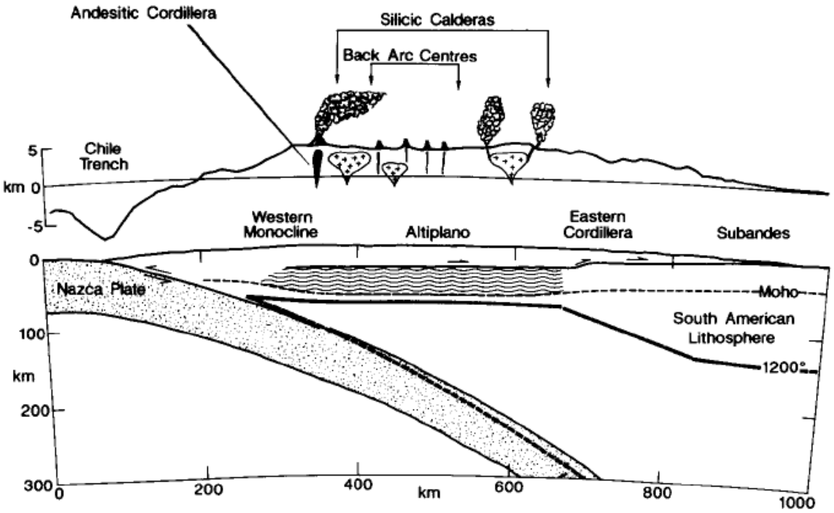

Fig.1.2. Cross section through the Central Andes showing exaggerated topography and distribution of andesitic volcanoes, back arc centers and large silicic calderas. From Francis and Hawkesworth (1994).

As noted by Francis and Thorpe (as cited in Francis and Hawkesworth, 1994), crustal thickness had a key role in influencing the character of the CVZ magmas. More specifically, they assert that the compositional differences between volcanic centers in the CVZ could be ascribed to the differences in mixing proportions of deep and sub-crustal components, the average ages and compositions of lower crustal source rocks, and the depths at which interactions between mantle-derived and crust-derived components take place. Moreover, other studies such as that of Folkes et al. (2011) suggest that at Cerro Galan there is a zone between mantle magma and upper crustal chambers, where magmas are geochemically buffered, producing the underlying geochemical and isotopic signatures. Building on the work of Hildreth and Moorbath's (as cited in Skewes and Sterns, 1995) on the existence of MASH (magma mixing, assimilation, storage, and homogenization) zones within the Andean crust that produce repeated ignimbrites of similar compositions, Folkes et al. (2011) asserts that a lower-crustal MASH beneath the Cerro Galan complex is responsible for the repeated production of magmas with very similar compositions as observed from the Toconquis Formation and Cerro Galan Ignimbrites.

This study concentrates on the Cerro Galan (CGI) and Cerro Blanco Ignimbrites, which are part of extensive ignimbrite sheets located at elevations around 4000 m that dominate the topography of the Central Andes (Francis and Hawkesworth 1994). The ignimbrite source calderas are located up to 200 km east of the arc (fig.1.2); show a restricted range of compositions (mainly dacitic); are sites of huge eruptions (2000-3000 km^3 of dacitic ignimbrites in the case of Cerro Galan complex), and show evidence of sporadic activity over millions of years (Sparks et al. 1985; Francis and Hawkesworth 1994; Folkes et al. 2011).

The Cerro Galan Complex started volcanic activity about 6 Ma with the eruption of several ignimbrites known as the Toconquis Formation. Following a 2 Ma period of volcanic quiescence after the eruption of the Toconquis Formation, the Cerro Galan complex had a major eruption of rhyodacitic magma of >650 km^3, forming the modern day caldera (Cas et al. 2011). This major eruption is known as the Cerro Galan Ignimbrite (CGI) and along with the Cerro Blanco Ignimbrite (less than 1 Ma in age) are the focus of this investigation. There appears to be no published work on the Cerro Blanco caldera.

Geologic Setting and Petrology

The Cerro Galan and Cerro Blanco caldera complexes are located on the eastern edge of the Altiplano-Puna plateau of northwest Argentina. The oldest and largest of the two calderas is Cerro Galan, located at 67^0 W and 26^0 S, and it is located approximately 120 km NW of Cerro Blanco as depicted in figure 3 below.

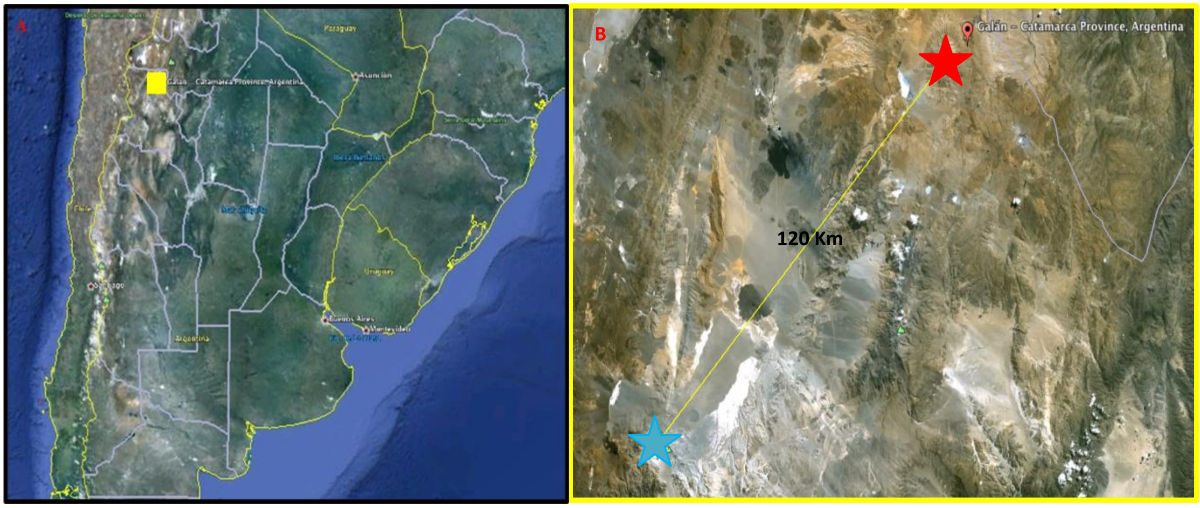

Fig.1.3. Regional view of the Cerro Galan and Cerro Blanco calderas. Panel B on the right shows a close-up view of the Cerro Galan and Cerro Blanco ignimbrites and calderas. Red and blue stars represent the location of the Cerro Galan and Cerro Blanco calderas respectively.

Large ash flows erupted from both volcanoes that are reasonably-well preserved and minimally eroded. The Cerro Galan Ignimbrite forms a 30-200 m thick outflow sheet that extends up to 100 km from the caldera rim. The CGI overlies basement rocks composed of greenschist to amphibolites facies metagraywackes, metapelites, amphibolites and granitoid augen-gneiss (Sparks et al. 1985). The locations of the analyzed stratigraphic sections along with a depiction of the CGI distribution taken from Cas et al. (2011) are shown in panels A thru C of figure 1.4.

Fig.1.4. Distribution of the Cerro Galan ignimbrite. Panel A shows the CGI distribution (taken from Cas et al. 2011). Panels B and C show the location of the sampled stratigraphic sections. Red dots represent the location of section 1(closer to the caldera) and section 2 (further away from the caldera) of the CGI. Blue dot represents the location of the section at Campo de Piedra Pomez of the Cerro Blanco ignimbrite.

The ignimbrites are crystal rich (40-55%) but lithic-and pumice poor (Francis et al. 1989). The mineralogical assemblage—in order of decreasing abundance—for both Cerro Galan and Cerro Blanco calderas is composed of plagioclase, sanidine, Fe-Ti oxides, biotite, quartz, apatite, and rare zircon. Grains sizes vary greatly with plagioclase crystals being the largest (up to 5 mm in diameter) and apatite being the mineral with the smallest size overall (grain as small as 30 µm in diameter).

Plagioclase and sanidine grains in both calderas are visibly fractured but otherwise present a homogeneous appearance with no visible alteration. The feldspars do not show any evidence of exsolution and compositions are consistent between samples—between samples from different vertical locations in the ash flow deposits—and within samples from the same vertical location. This leads to the conclusion that feldspar grains most likely have preserved equilibrium compositions, which would reflect magma chamber conditions prior to eruption of the calderas.

Conversely, apatite and the Fe-Ti oxides show significant exsolution. The Fe-Ti oxides present exsolution of rutile, while apatite presents exsolution of an iron-rich phase. Apatite, biotite, and the iron oxides show great variability in composition between samples of different vertical location in the ash flow deposits, and also within samples of the same vertical location. These characteristics may indicate that these minerals re-equilibrated at subsolidus temperatures. If this were the case, compositions obtained from these minerals would no longer be viable to estimate the pre-eruptive conditions in the sub-volcanic magma chambers of Cerro Galan and Cerro Blanco.

Summary of the Investigation

In this study halogens vs. vertical location within magma chambers, feldspar thermometry, and Fe-Ti oxide geothermometry were used in order to infer the pre-eruptive conditions in the magma chambers of Cerro Galan and Cerro Blanco. Results indicate that apatite, biotite, and the Fe-Ti oxides were affected by post-emplacement processes that affected the equilibrium compositions of these minerals. The wide variability in compositions of the previously mentioned minerals along with the presence of strong exsolution (only seen in apatite and the Fe-Ti oxides) indicated that these minerals are unable to provide insight into the conditions of the calderas prior to eruption.

Due to their homogeneous appearance, the lack of visible chemical alteration, and the lack of variation in composition of the feldspars (plagioclase and alkali-feldspar) it is inferred that these phases preserved pre-eruptive equilibrium compositions. Feldspar thermometry indicates that both Cerro Galan and Cerro Blanco sub-volcanic chambers were at a minimum pressure of 2 kb, based on an equilibrium temperature of about 700 ^{0}C and 4% H_2O saturation.

Some of the initial objectives that went unfulfilled in this project include the estimation of pressure and volatile (F, Cl, OH) and oxygen fugacities through the use of thermodynamics. These objectives could not be achieved due to presence of post-emplacement phenomena that disrupted the equilibrium compositions of apatite, biotite and Fe-Ti oxides.

CHAPTER 2

Feldspar thermometry

Introduction

Ternary-feldspar thermometry is based on compositions of the coexisting phases (plagioclase and K-feldspar) at equilibrium along the solvus (Hokada 2001, Elkins and Grove 1990). At or above the critical temperature (T_c) of the solution, the pairs $NaAlSi_3O_8$ (albite) - $CaAl_2Si_2O_8$ (anorthite), and $KAlSi_3O_8$ (K-feldspar) – $NaAlSi3O_8$ exist as a single supercritical phase; however, at temperatures below the critical temperature of the solution two distinct phases coexist at equilibrium (Patino 2011). Temperatures obtained by this method represent temperatures at which cation exchange ceased due to diffusion rates being too slow relative to cooling rate (cooling was very fast and this hindered cation exchange). This technique was used as an independent method for the determination of equilibrium temperatures in the magmatic chambers of Cerro Galan and Cerro Blanco. The results from this technique were compared to equilibrium temperatures obtained from oxide compositions.

Analytical Procedures

Electron Microprobe Analyses

Individual feldspar crystals were analyzed with the University of Georgia Department of Geology JEOL 8600 electron microprobe using a 15 kV accelerating voltage and 15 nA beam current. Quantitative analyses were performed with wavelength dispersive spectrometers (WDS) automated with a dQant control system from Geller MicroAnalytical Laboratory, Inc. Calibrations and analyses were done using 10 second counting times, and natural and synthetic mineral standards. Analyses were calculated using the Armstrong (1988) Phi-Rho-Z matrix correction model. Backscattered electron (BEI) and secondary electron images were acquired using dPict imaging software. Tables 2.1—2.6 show plagioclase and sanidine compositions for sections 1 & 2 of Cerro Galan and Cerro Blanco.

Table 2.1. Section 1 Cerro Galan plagioclase compositions obtained by electron microprobe analyses

Plagioclase oxide weight percent										
Sample	**SiO2**	**TiO2**	**Al2O3**	**MgO**	**FeO**	**MnO**	**CaO**	**K2O**	**Na2O**	**BaO**	**Total**
A0737F1	59.28	0.00	25.35	0.00	0.07	0.00	7.70	0.70	6.21	0.00	99.7
A0737F5	60.21	0.00	25.05	0.00	0.26	0.00	7.24	0.75	6.47	0.09	100.5
A0738F1	59.34	0.03	25.64	0.00	0.00	0.00	7.88	0.66	6.74	0.05	100.6
A0738F2	59.62	0.00	25.41	0.02	0.09	0.08	7.16	0.78	6.31	0.01	99.9
A0738F3	56.70	0.02	27.24	0.00	0.37	0.03	9.91	0.47	5.34	0.00	100.5
A0739F2	59.81	0.04	25.11	0.00	0.33	0.00	7.28	0.67	6.41	0.18	100.1
A0739F3	59.44	0.01	25.89	0.00	0.11	0.00	7.69	0.66	6.46	0.00	100.5
A0740F1	59.17	0.00	24.83	0.00	0.17	0.00	7.11	0.76	6.62	0.00	99.0
A0740F2	58.26	0.07	25.98	0.04	0.17	0.13	8.62	0.57	5.91	0.02	100.1
A0740F3	59.94	0.05	24.97	0.01	0.17	0.00	7.85	0.67	6.66	0.00	100.6
A0740F4	59.46	0.09	25.72	0.00	0.13	0.18	7.44	0.64	6.59	0.00	100.6
A0741F2	60.57	0.02	24.29	0.00	0.24	0.00	6.94	0.75	6.72	0.00	99.8
A0741F5	59.63	0.00	25.79	0.02	0.22	0.00	7.84	0.60	6.20	0.10	100.9
A0742F3	59.63	0.02	25.76	0.01	0.15	0.21	7.37	0.56	6.85	0.00	100.9
A0742F4	59.15	0.03	25.33	0.00	0.28	0.05	7.27	0.63	6.18	0.00	99.2
A0742F5	60.66	0.03	24.79	0.00	0.24	0.03	7.22	0.73	7.02	0.06	101.1
A0742F6	59.30	0.07	26.17	0.00	0.24	0.05	7.78	0.64	6.28	0.09	101.0
A0743F2	59.53	0.00	24.87	0.00	0.17	0.00	6.73	0.72	6.92	0.00	99.1
A0743F3	58.57	0.00	25.64	0.00	0.25	0.04	7.25	0.66	6.56	0.00	99.4
A0743F4	60.29	0.07	24.65	0.00	0.12	0.00	6.02	0.80	7.19	0.00	99.4
A0743F5	59.31	0.04	25.05	0.00	0.28	0.12	6.82	0.66	6.73	0.00	99.3
A0744F1	49.99	0.04	30.17	0.07	0.42	0.01	12.03	0.13	4.45	0.00	97.5

A0744F1	43.10	0.39	13.25	7.82	20.53	0.25	11.71	0.71	1.46	0.00	99.4
A0744F1A	61.54	0.03	24.33	0.00	0.11	0.03	5.44	0.23	7.99	0.00	99.9
A0744F1B	50.48	0.04	30.60	0.00	0.29	0.09	13.06	0.10	4.10	0.00	99.0
A0744F2A	50.47	0.07	30.42	0.02	0.97	0.07	13.10	0.09	3.87	0.00	99.3
A0744F2B	54.99	0.03	28.10	0.02	0.85	0.03	9.95	0.10	5.44	0.00	99.7
A0744F2C	61.26	0.02	24.96	0.00	0.22	0.07	4.82	0.51	8.10	0.00	100.3
A0744F3A	54.31	0.11	28.87	0.09	0.73	0.04	10.48	0.15	5.21	0.00	100.2
A0744F3B	58.73	0.00	23.42	0.00	0.10	0.05	4.23	0.29	7.90	0.00	94.9
A0744F4	48.72	0.08	31.24	0.00	0.24	0.00	13.82	0.04	3.71	0.00	98.1
A0745F2	59.69	0.02	24.82	0.03	0.19	0.00	7.02	0.61	6.95	0.00	99.6
A0745F3	58.91	0.00	25.41	0.00	0.19	0.00	7.31	0.56	6.81	0.00	99.5
A0745F5	57.65	0.03	24.86	0.00	0.23	0.00	6.72	0.68	7.33	0.00	97.8
A0743F4	60.29	0.07	24.65	0.00	0.12	0.00	6.02	0.80	7.19	0.00	99.4

Table 2.2. Section 1 Cerro Galan sanidine compositions obtained by electron microprobe analyses

Sanidine oxide weight percent											
Sample	**SiO2**	**TiO2**	**Al2O3**	**MgO**	**FeO**	**MnO**	**CaO**	**K2O**	**Na2O**	**BaO**	**Total**
A0737F2	61.57	0.02	18.63	0.00	0.17	0.05	0.23	11.69	2.04	0.40	95.26
A0737F3	64.38	0.12	19.09	0.00	0.17	0.05	0.14	12.47	2.29	0.49	99.57
A0737F6	66.10	0.05	18.81	0.00	0.02	0.00	0.16	12.82	2.55	0.58	101.49
A0738F4	64.74	0.00	19.29	0.00	0.24	0.03	0.20	12.75	2.14	0.88	100.69
A0738F5	65.83	0.03	18.79	0.00	0.07	0.00	0.17	12.58	2.15	0.00	99.93
A0738F6	65.91	0.05	19.02	0.00	0.13	0.00	0.12	12.77	2.31	0.64	101.26
A0739F1	65.94	0.00	19.31	0.00	0.26	0.00	0.22	12.34	2.33	0.30	101.04

A0739F4	65.93	0.02	18.88	0.00	0.09	0.05	0.16	12.52	2.43	0.47	101.00
A0739F5	66.03	0.03	19.10	0.05	0.15	0.03	0.14	12.82	2.13	0.28	101.07
A0739F6	66.17	0.10	19.00	0.00	0.20	0.00	0.21	12.26	2.33	0.55	101.30
A0740F5	63.59	0.03	18.95	0.01	0.02	0.08	0.14	12.76	2.16	0.20	98.41
A0740F6	65.66	0.02	18.61	0.00	0.11	0.05	0.19	12.64	2.59	0.31	100.44
A0741F1	65.29	0.00	18.60	0.01	0.13	0.10	0.17	13.07	2.21	0.52	100.49
A0741F3	65.74	0.05	18.86	0.00	0.00	0.18	0.15	12.72	2.52	0.45	100.90
A0741F4	66.15	0.02	19.01	0.00	0.00	0.00	0.14	12.62	2.43	0.56	101.34
A0741F6	66.15	0.00	18.75	0.01	0.13	0.05	0.15	13.00	2.21	0.30	101.24
A0742F1	65.99	0.03	18.93	0.00	0.07	0.05	0.16	12.72	2.17	0.12	100.65
A0742F2	65.16	0.00	19.13	0.00	0.11	0.13	0.25	12.41	2.18	0.79	100.55
A0743F1	65.16	0.02	19.06	0.00	0.13	0.01	0.11	12.75	2.18	0.29	100.21
A0743F6	64.49	0.05	19.48	0.00	0.12	0.08	0.15	12.93	2.16	0.41	100.24
A0745F1	64.98	0.04	19.28	0.00	0.20	0.17	0.20	12.53	2.14	0.56	100.52
A0745F4	64.62	0.00	18.69	0.00	0.17	0.00	0.11	13.37	2.06	0.32	99.77
A0745F6	65.14	0.02	19.12	0.02	0.12	0.03	0.16	13.24	2.29	0.18	100.72

Table 2.3. Section 2 Cerro Galan plagioclase compositions obtained by electron microprobe analyses

Plagioclase oxide weight percent										
Sample	**SiO2**	**TiO2**	**Al2O3**	**MgO**	**FeO**	**MnO**	**CaO**	**K2O**	**Na2O**	**BaO**	**Total**
A0701F3	56.72	0.01	24.64	0.01	0.00	0.00	7.25	0.77	6.86	0.11	96.38
A0701F4	55.29	0.00	25.21	0.00	0.08	0.05	7.12	0.80	6.44	0.03	95.03
A0701F6	59.30	0.02	24.99	0.00	0.23	0.00	6.77	0.83	6.78	0.00	98.91
A0702F1	59.54	0.01	25.38	0.00	0.08	0.00	7.22	0.68	6.95	0.00	99.86

A0702F3	59.93	0.03	25.61	0.00	0.19	0.00	7.28	0.67	6.77	0.00	100.47
A0702F4	56.39	0.02	28.20	0.00	0.33	0.03	9.78	0.38	5.57	0.02	100.71
A0702F5	60.70	0.00	25.33	0.00	0.04	0.00	6.19	0.87	7.14	0.02	100.29
A0703F2	57.70	0.00	27.01	0.00	0.25	0.00	8.48	0.54	6.17	0.00	100.15
A0703F3	59.53	0.05	26.90	0.00	0.10	0.05	7.86	0.60	6.18	0.00	101.27
A0703F4	59.80	0.01	26.07	0.00	0.06	0.03	6.78	0.65	7.16	0.04	100.60
A0703F5	60.16	0.02	25.77	0.00	0.08	0.00	6.78	0.70	6.77	0.00	100.28
A0704F1	99.42	0.09	0.06	0.00	0.02	0.00	0.03	0.02	0.01	0.00	99.64
A0704F1	55.65	0.02	26.26	0.00	0.37	0.03	6.78	0.74	6.81	0.00	96.66
A0704F3	52.96	0.00	26.26	0.00	0.08	0.00	7.10	0.70	6.77	0.00	93.88
A0704F5	59.94	0.00	25.94	0.01	0.25	0.03	7.09	0.65	6.77	0.00	100.67
A0705F2	59.47	0.04	26.48	0.03	0.00	0.03	7.25	0.69	6.62	0.10	100.71
A0705F3	59.78	0.00	26.79	0.00	0.50	0.13	7.37	0.65	6.25	0.12	101.59
A0705F4	60.24	0.00	25.96	0.01	0.19	0.13	7.06	0.69	6.48	0.01	100.76
A0706F3	59.90	0.00	26.10	0.01	0.04	0.11	6.62	0.79	7.05	0.00	100.62
A0706F4	59.15	0.00	26.80	0.00	0.31	0.08	7.72	0.64	6.72	0.00	101.42
A0707F1	59.87	0.05	24.67	0.00	0.37	0.00	6.66	0.75	7.33	0.00	99.70
A0707F2	59.18	0.01	25.11	0.00	0.10	0.00	6.59	0.66	6.89	0.05	98.60
A0707F4	59.56	0.02	25.46	0.00	0.06	0.03	6.95	0.66	7.06	0.00	99.79
A0707F5	59.20	0.00	25.24	0.00	0.14	0.00	6.87	0.77	7.35	0.04	99.62
A0707F6	58.92	0.00	25.50	0.00	0.27	0.08	7.45	0.69	6.80	0.00	99.70

Table 2.4. Section 2 Cerro Galan sanidine compositions obtained by electron microprobe analyses

Sanidine oxide weight percent										
Sample	**SiO2**	**TiO2**	**Al2O3**	**MgO**	**FeO**	**MnO**	**CaO**	**K2O**	**Na2O**	**BaO**	**Total**
A0701F1	64.89	0.05	18.97	0.00	0.00	0.03	0.19	12.59	2.52	0.31	99.55
A0701F5	64.53	0.00	19.08	0.04	0.12	0.00	0.19	13.20	2.19	0.35	99.70
A0702F2	64.81	0.02	18.96	0.07	0.04	0.13	0.21	12.20	2.35	1.12	99.90
A0703F1	64.88	0.00	19.34	0.00	0.14	0.00	0.17	13.17	2.52	0.44	100.67
A0704F2	63.43	0.02	19.93	0.06	0.16	0.16	0.13	12.68	2.51	0.50	99.58
A0704F4	63.46	0.02	19.58	0.02	0.25	0.00	0.14	12.42	2.59	0.16	98.64
A0705F1	61.99	0.06	18.84	0.00	0.25	0.00	0.19	13.08	2.33	0.22	96.96
A0705F5	65.68	0.00	19.69	0.00	0.04	0.11	0.12	13.20	2.26	0.31	101.40
A0706F1	64.56	0.02	18.87	0.04	0.06	0.08	0.12	11.74	2.84	0.22	98.56
A0706F2	64.62	0.08	19.74	0.00	0.06	0.00	0.14	12.95	2.24	0.70	100.53
A0706F5	64.68	0.04	19.97	0.01	0.06	0.08	0.18	13.02	2.24	0.50	100.78
A0707F3	64.77	0.01	19.07	0.03	0.10	0.03	0.14	13.20	2.28	0.62	100.24

Table 2.5. Cerro Blanco plagioclase compositions obtained by electron microprobe analyses

Plagioclase oxide weight percent											
Sample	**SiO2**	**TiO2**	**Al2O3**	**MgO**	**FeO**	**MnO**	**CaO**	**K2O**	**Na2O**	**BaO**	**Total**
A0763F2	63.36	0.02	22.75	0.00	0.05	0.00	4.36	1.29	7.66	0.07	99.56
A0763F3	62.24	0.03	23.36	0.00	0.23	0.00	5.35	1.05	7.44	0.04	99.75
A0764F1	61.09	0.00	24.09	0.00	0.28	0.04	6.07	0.82	7.03	0.00	99.42
A0764F4	62.18	0.00	24.03	0.03	0.33	0.00	5.36	1.13	7.80	0.00	100.86
A0764F5	62.29	0.04	23.88	0.00	0.16	0.00	5.14	1.19	7.13	0.00	99.84
A0765F1	57.64	0.01	26.74	0.00	0.15	0.00	9.03	0.48	6.14	0.00	100.18

A0765F3	60.12	0.02	24.66	0.01	0.10	0.03	6.42	0.83	6.95	0.04	99.17
A0766F3	60.99	0.03	24.67	0.00	0.26	0.03	6.09	0.86	7.17	0.00	100.10
A0766F5	58.97	0.03	25.56	0.02	0.21	0.00	7.34	0.64	6.40	0.06	99.23
A0767F1	59.63	0.00	25.42	0.00	0.21	0.00	7.31	0.71	6.71	0.05	100.04
A0767F4	62.08	0.02	24.45	0.00	0.22	0.00	5.64	1.01	7.56	0.06	101.04
A0767F5	61.08	0.00	24.27	0.01	0.20	0.04	6.18	0.87	6.84	0.01	99.51
A0768F1	59.18	0.06	25.71	0.00	0.27	0.00	7.42	0.70	6.53	0.03	99.90
A0768F4	61.16	0.00	24.50	0.00	0.29	0.00	6.01	0.85	7.56	0.02	100.40
A0768F5	60.94	0.02	24.67	0.00	0.22	0.00	6.00	0.97	6.92	0.00	99.75

Table 2.6. Cerro Blanco sanidine compositions obtained by electron microprobe analyses

Sanidine oxide weight percent											
Sample	**SiO2**	**TiO2**	**Al2O3**	**MgO**	**FeO**	**MnO**	**CaO**	**K2O**	**Na2O**	**BaO**	**Total**
A0763F1	66.06	0.00	18.68	0.00	0.01	0.00	0.22	11.92	2.85	0.07	99.81
A0763F4	64.98	0.04	19.45	0.00	0.18	0.00	0.24	10.87	3.06	1.48	100.30
A0763F5	64.64	0.01	19.36	0.03	0.21	0.00	0.36	10.88	3.14	1.39	100.02
A0764F2	65.50	0.04	18.51	0.02	0.17	0.00	0.28	11.52	3.02	0.61	99.67
A0764F3	65.55	0.02	19.68	0.00	0.13	0.03	0.32	11.21	3.01	1.20	101.15
A0765F2	64.78	0.04	19.10	0.00	0.22	0.00	0.32	10.81	3.07	1.68	100.01
A0765F4	66.09	0.00	18.50	0.00	0.11	0.08	0.15	11.62	3.02	0.49	100.05
A0765F5	64.77	0.00	19.69	0.01	0.23	0.03	0.27	11.03	3.30	1.31	100.64
A0766F1	65.82	0.00	18.88	0.00	0.02	0.00	0.21	11.07	3.28	0.12	99.40
A0766F2	66.36	0.00	19.41	0.02	0.18	0.00	0.22	11.39	3.04	0.12	100.74
A0766F4	65.94	0.00	18.73	0.00	0.12	0.00	0.25	11.90	2.93	0.00	99.87

A0767F2	64.54	0.03	19.20	0.00	0.21	0.00	0.35	10.92	3.18	1.41	99.84
A0767F3	64.40	0.07	19.66	0.00	0.13	0.01	0.25	10.65	2.96	1.62	99.75
A0768F2	64.15	0.00	19.40	0.00	0.10	0.00	0.27	10.50	3.33	1.27	99.02
A0768F3	64.40	0.02	19.61	0.00	0.15	0.03	0.25	10.54	3.39	1.48	99.87

Feldspar Structural Formulae Calculations

Feldspar oxide concentrations were recalculated to 16 charges and 5 cations based on the structural formula of plagioclase ($CaAl_2Si_2O_8$ – $NaAl_3SiO_8$) and alkali-feldspar (KAl_3SiO_8 – $NaAl_3SiO_8$) solid solutions. Feldspar analyses to be used for thermodynamic calculations and feldspar thermometry were selected on the basis of two main parameters: the oxide total obtained from electron microprobe analyses close to 100 (+/- 1), and cation total close to 5 (+/- 0.1).

Feldspars were separated into plagioclase and alkali-feldspar based on the amount of K and Ca content. Plagioclase was selected based on minimal concentration of K and a significant amount of Ca. Alkali-feldspar was selected using the reverse situation than that used for selecting plagioclase.

Feldspar Compositions

Ternary plots were made using Ca, K, and Na molar concentrations for each analysis. Plots for each of the sections (sections 1and 2 of Cerro Galan and Cerro Blanco) were made separately utilizing all analysis from tables 2.1—2.6 that satisfied the above described criteria. Each of the samples representing a single vertical location were color-coded to aid visualization (figs.2.1—2.3).

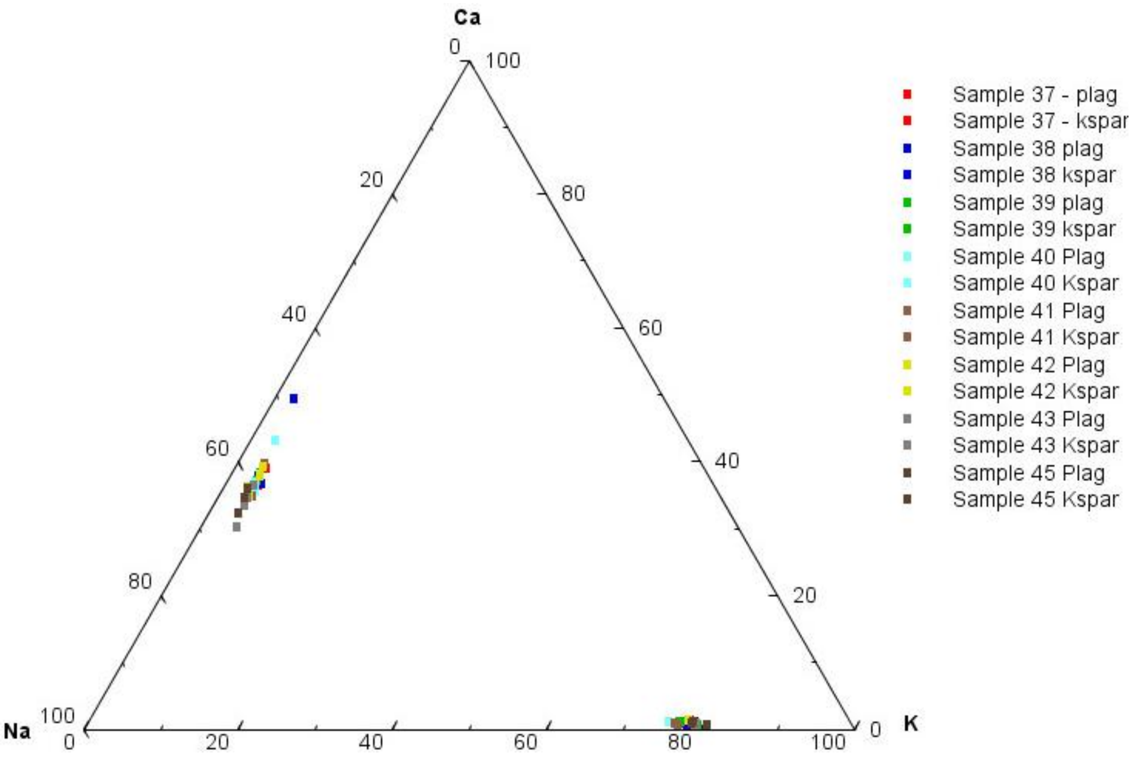

Fig.2.1. Ternary diagram of feldspar samples from section 1 of Cerro Galan

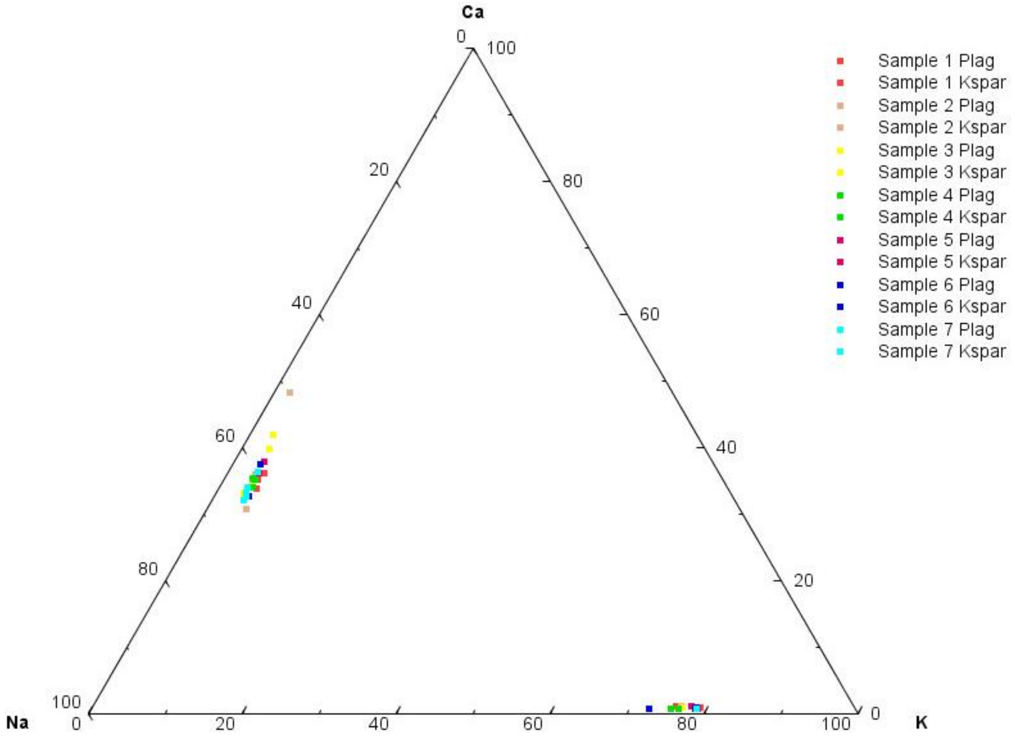

Fig.2.2. Ternary diagram of feldspar samples from section 2 of Cerro Galan

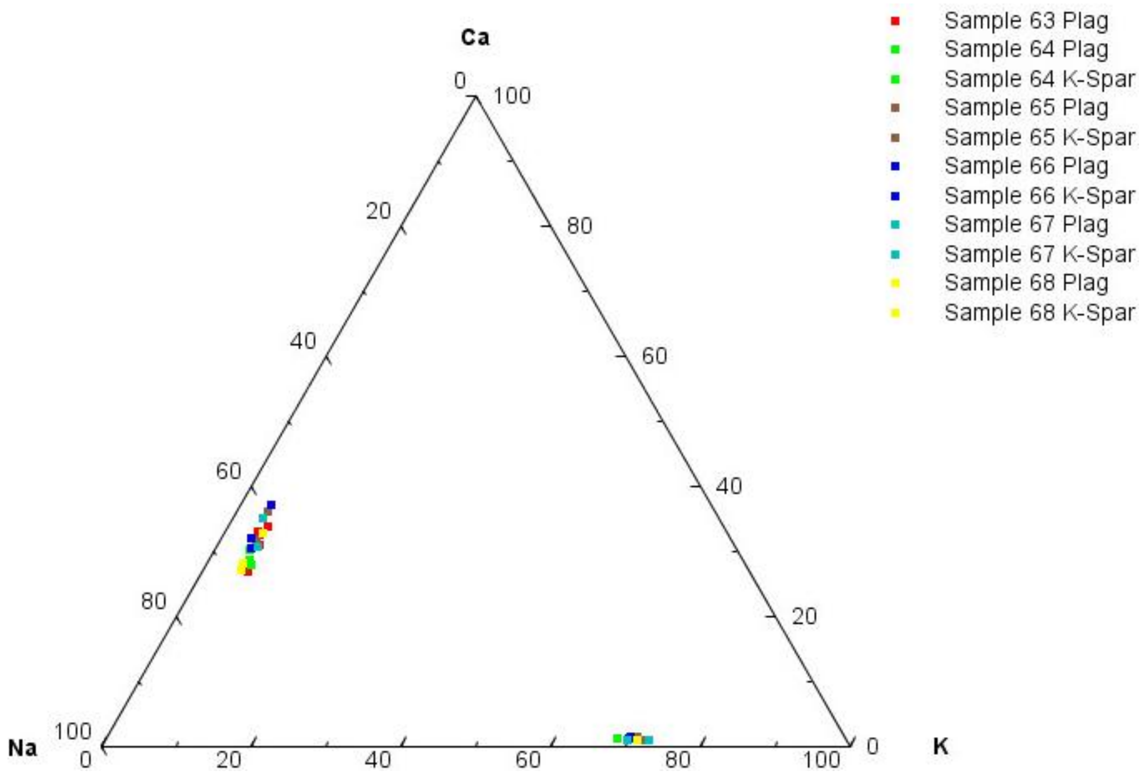

Fig.2.3. Ternary diagram of feldspar samples from Cerro Blanco

Compositions of coexisting feldspars were compared to Hokada's (2001) ternary feldspar model with calculated isotherms—which represent a projection of the feldspar solvus onto the three-component compositional coordinates—in order to estimate the temperatures at which cation exchange between the two feldspar phases ceased. Folkes et al. (2011) calculated pressures in Cerro Galan using hornblende as a mineral barometer. Pressures obtained by this method ranged from 1 to 5 kb, which corresponds to estimated depths ranging from 6-18 km, based on simple hydrostatic pressure (P = ρgh) calculations, assuming a crustal density of 2700 kg/m^3 (Folkes 2011).

Based on the pressure range stated above, feldspar thermometry for the Cerro Galan and Cerro Blanco samples was done using ternary-feldspar models at 1kb. This is a reasonable approach because the shape of the temperature-composition solvus for ternary feldspars is greatly affected by temperature changes—higher temperatures leads to a greater solubility and therefore narrower T-X solvus curve—but only slightly with pressure changes (Nekvasil 1994). Hence, the use of ternary models with isotherms at different pressures, 1-5 kb, will not significantly affect temperature calculations for the analyzed samples. Estimated temperatures from feldspar compositions in this study would have an uncertainty of (+/-) 15 ^{0}C, if the magmatic pressures were within the range of 1 and 5 kb as seen on figure 4 (Fuhrman and Lindsley 1988).

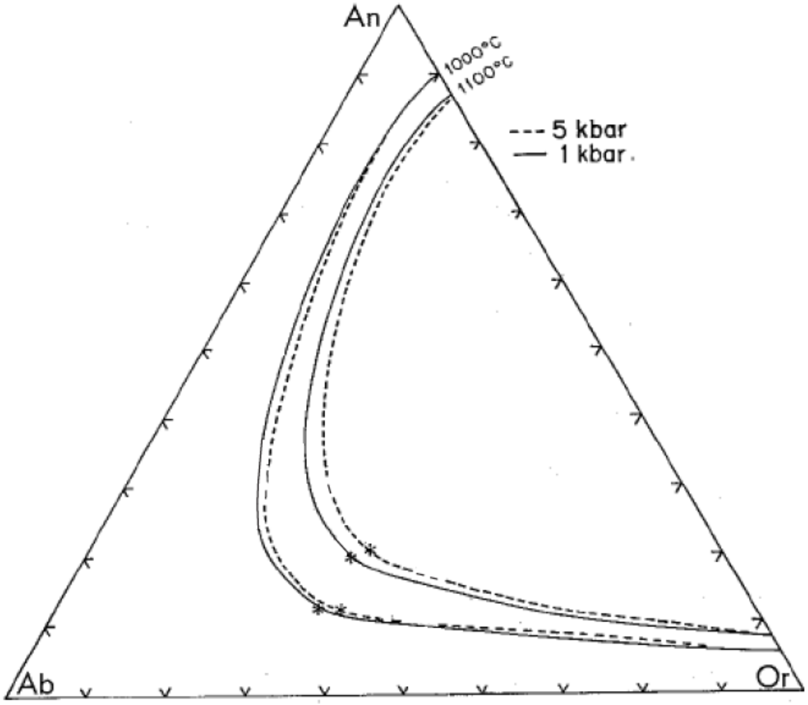

Fig.2.4. Feldspar ternary diagram modified from Fuhrman and Lindsley (1988). Isotherms at 1000 and 1100 ^{0}C and pressures of 1 and 5 kb.

Figures 2.5–2.7 are ternary plots for sections 1&2 of Cerro Galan and Cerro Blanco. These plots were obtained by plotting data points of the different sections onto Hokada's (2001) ternary-feldspar model at 1Kb.

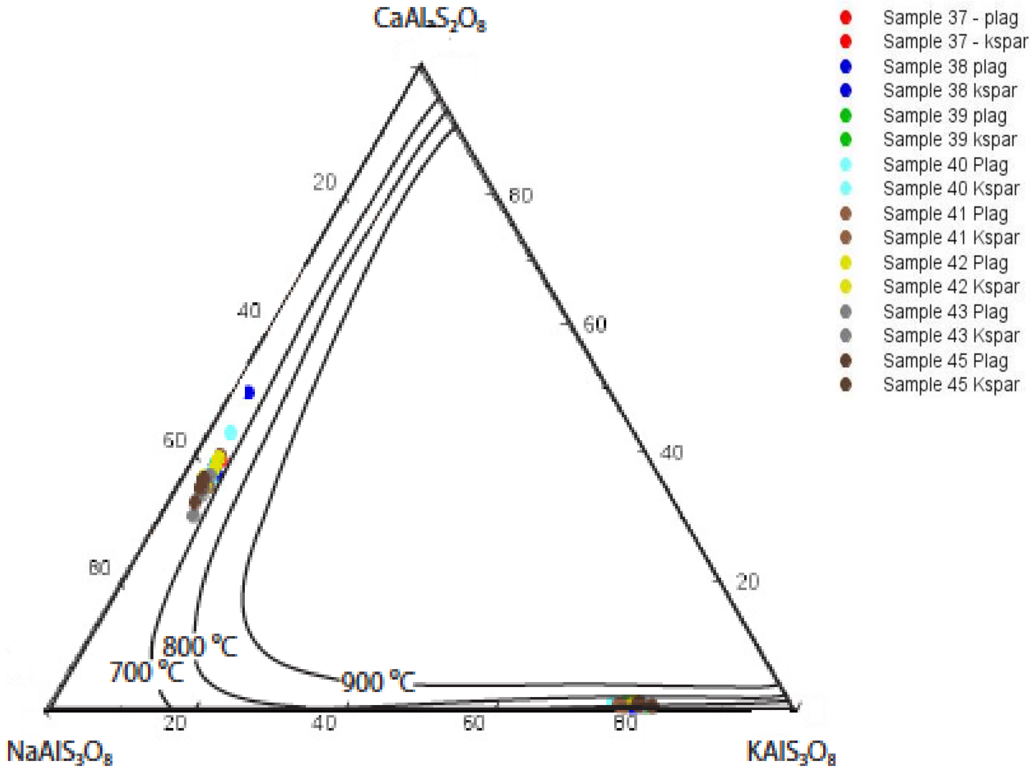

Fig.2.5. Ternary diagram of feldspar samples from section 1 of Cerro Galan compounded to Hokada's 2001 ternary feldspar model with calculated isotherms.

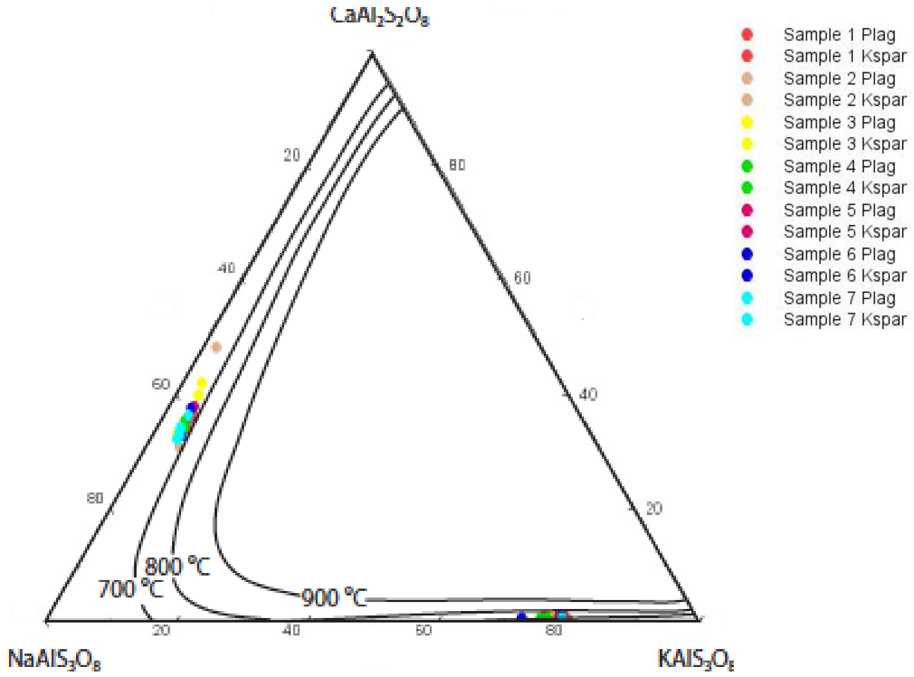

Fig.2.6. Ternary diagram of feldspar samples from section 2 of Cerro Galan compounded to Hokada's 2001 ternary feldspar model with calculated isotherms.

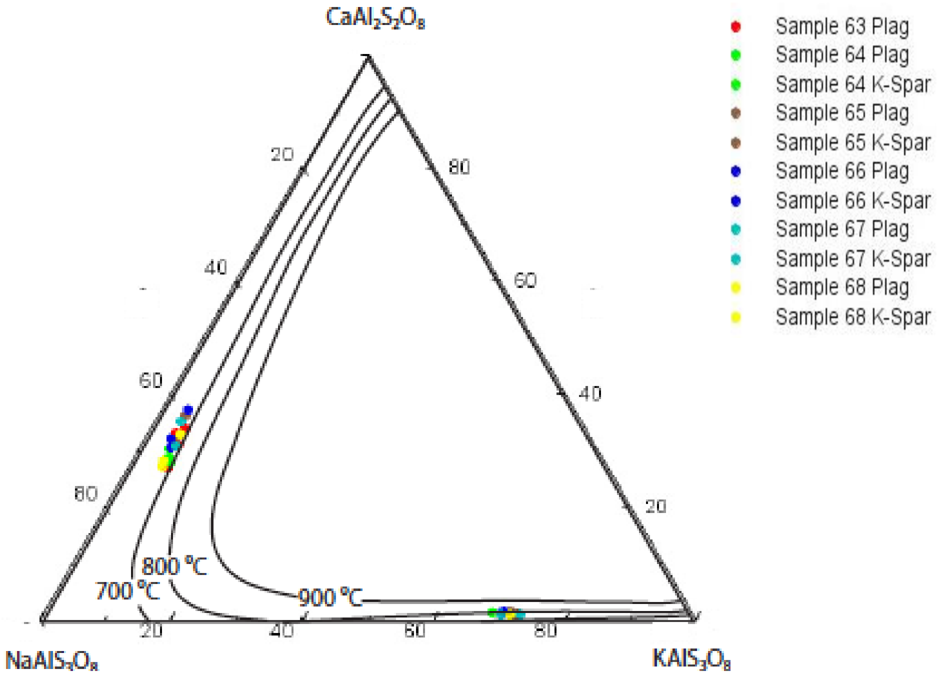

Fig.2.7. Ternary diagram of feldspar samples from Cerro Blanco compounded to Hokada’s 2001 ternary feldspar model with calculated isotherms.

Results and Discussion

The results of feldspar thermometry indicate magmatic temperatures for Cerro Galan (sections 1 and 2) and Cerro Blanco ranged from 650 ^{0}C to 700 ^{0}C. Temperatures among the two Cerro Galan sections, as well as temperatures between calderas present consistent results with little variability. This is in contrast to the Fe-Ti oxide minerals which show a great variability between sections and among samples. As discussed in the Fe-Ti oxide chapter, these minerals present a clear indication of post-emplacement, high-temperature oxidation which greatly altered the compositions of the titanomagnetites and titanohematites. Nonetheless, from figs 2.5—2.7 and compositional data of the feldspars, it is observed that the erratic trend in compositions seen in the Fe-Ti oxides is not present in the feldspars. This could signify that either the feldspars analyzed in this study kept pre-eruptive equilibrium compositions of cation exchange, or that both ignimbrite flows followed similar post-eruptive cooling histories that led to similar cation concentrations in the feldspars.

One of the lines of evidence in support of the first scenario are SEM images of alkai–feldspar and plagioclase from the three sections as depicted in figs.2.8–2.10.

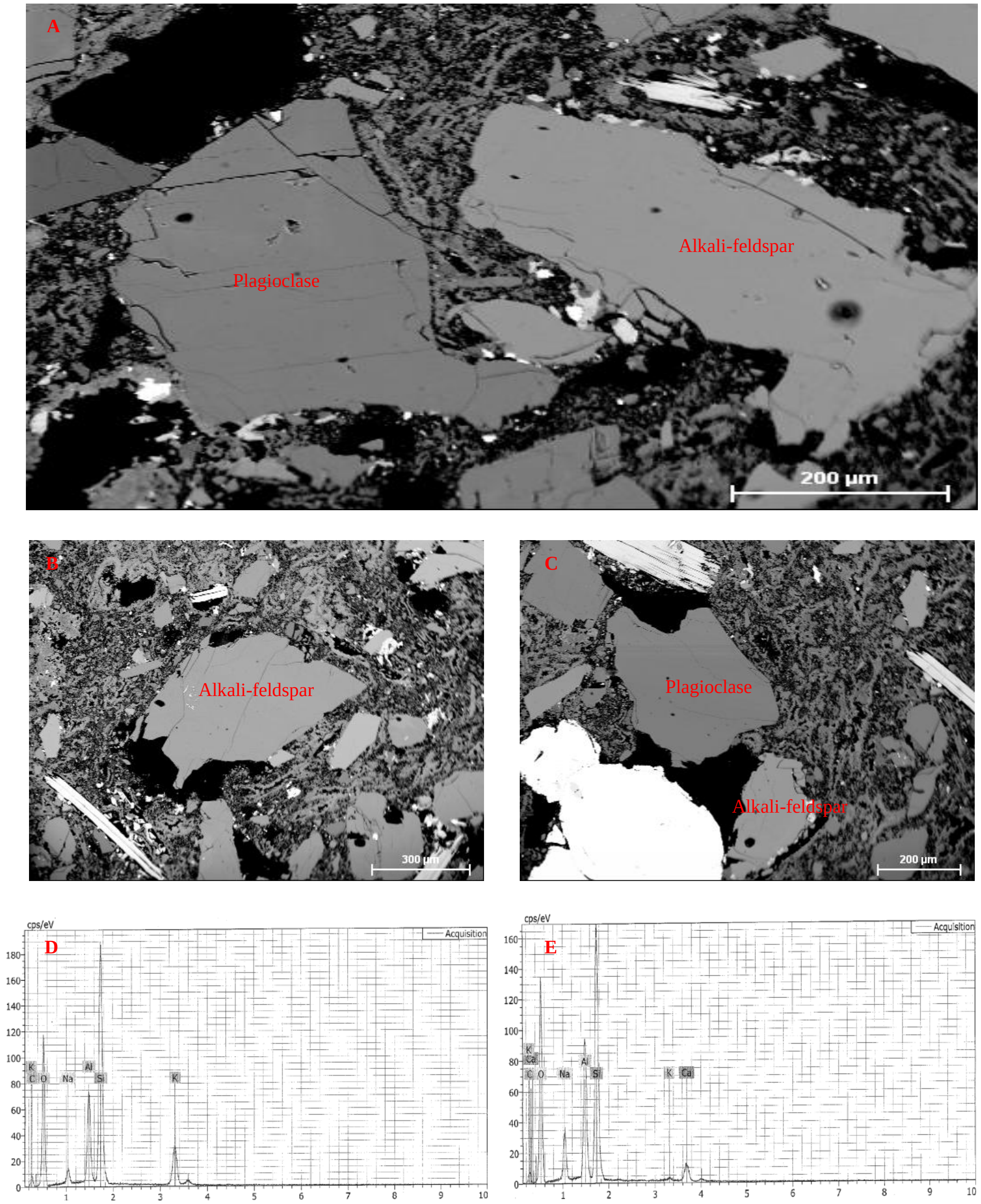

Fig.2.8. Panels A- C are SEM images of alkai-feldspar and plagioclase from section 1 of Cerro Galan. Panels D and E are representative X-Ray spectra of alkali-feldspar and a plagioclase grains respectively.

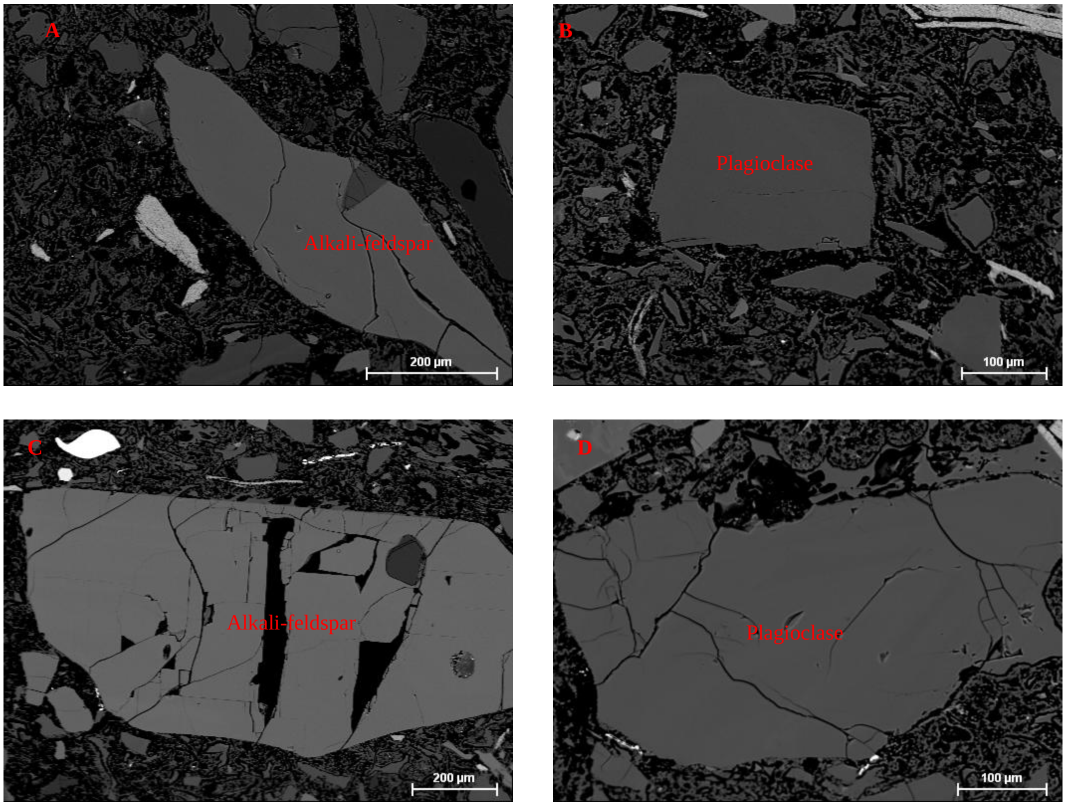

Fig.2.9. Panels A-D are SEM images of alkai-feldspar and plagioclase from section 2 of Cerro Galan

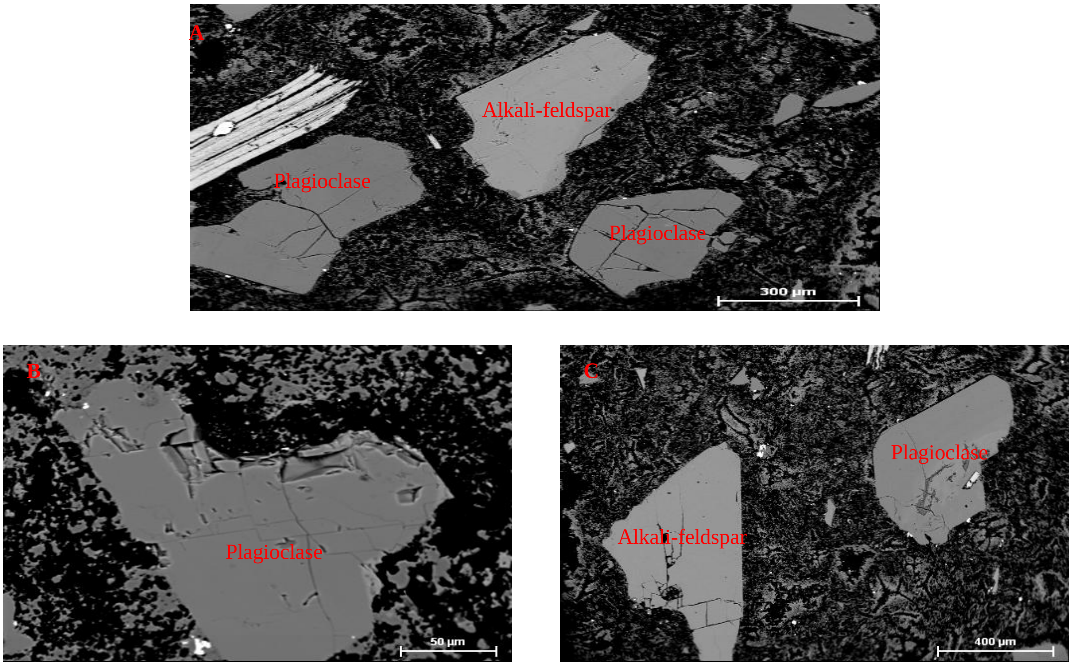

Fig.2.10. Panels A- C are SEM images of alkai-feldspar and plagioclase from Cerro Blanco

As can be seen from figs. 2.8–2.10 feldspar crystals from both sections present signs of mechanical abrasion in the form of fractured grains—which is to be expected due the mechanical abrasion among grains in the ash flow—but no sign of chemical disequilibrium, as would be seen by rims on the feldspar crystals. Rims would be potassium-poor in the case of plagioclase and potassium-rich in the case of alkali-feldspar.

Implications for Equilibrium Temperatures

If feldspar grains preserved cation concentrations at equilibrium before eruption of the ash flow, then the temperatures obtained from feldspar thermometry yield pre-eruptive temperatures of the magma chambers. If this was the case it may have implications for the composition of the magma. As seen from fig. 2.11 (modified from Winter 2001), dry silicic melts at pressures of 1 to 2 kb (equivalent to 0.1 and 0.2 GPa) exist at temperatures above 1000 ^{0}C. However, as the concentration of water increases in the system, eutectic melting—melting at an invariant point in which pressure, temperature, and phase composition remain fixed until a phase is lost, gaining a degree of freedom— shifts towards lower temperatures.

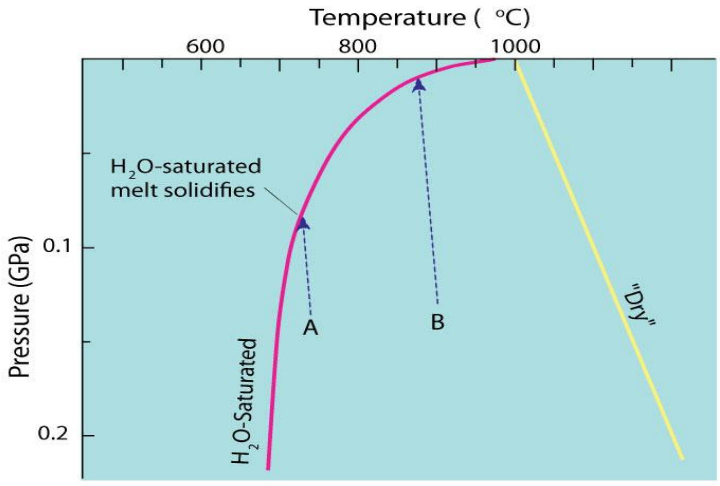

Fig.2.11. Pressure-temperature phase diagram showing the solidus curves for H_2O-saturated and dry granite (taken from Winter, 2001). An H_2O-saturated granitoid just above the solidus at A will quickly intersect the solidus as it rises and will therefore solidify. A hotter, H_2O-undersaturated granitoid at B will rise further before solidifying.

This means that in order for temperatures obtained from feldspar thermometry (650-700 ^{0}C) to represent magmatic equilibrium temperatures—as opposed to temperatures at which cation diffusion stopped—at the inferred pressures for both magmatic chambers the melts in both calderas had to be water-saturated , or close to water saturation. For pressures of 1-2 kb and approximate temperatures of 650-700 ^{0}C a water-saturated rhyolitic magma must contain approximately 3–4 % H_2O as seen on fig. 2.12. This H_2O concentration is consistent with previous estimates of 4% H_2O content in the Cerro Galan ignimbrite by Folkes et al. (2011) who analyzed melt inclusion in the quartz grains of the CGI.

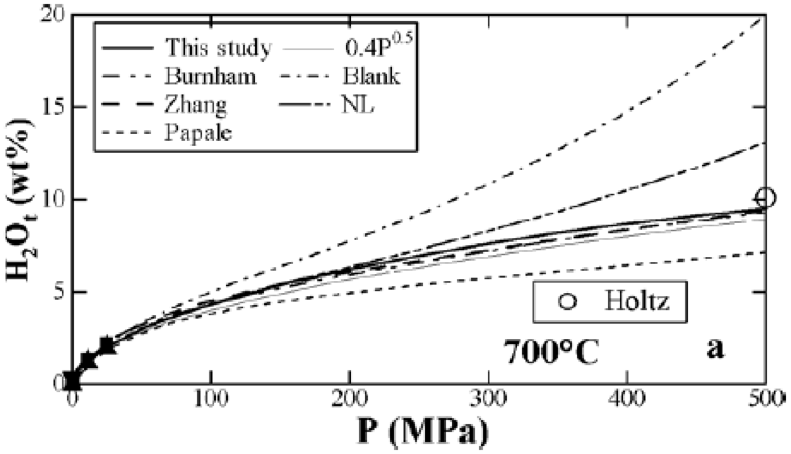

Fig.2.12. H_2O solubility in rhyolitic melts at 700 ^{0}C modified from Liu et al. (2005)

Comparison with Other Studies

Temperatures obtained in this work contrast other studies that report temperatures ranging from 770 – 840 ^{0}C for the Cerro Galan Ignimbrite (Folkes et al. 2011). In order to test whether the temperature difference between both studies could be due to analytical and sample variation errors, plots were made in which these errors were accounted for. These plots were made by using standard deviations of standard sample analyses—in order to account for analytical error—and the standard deviation of actual samples—in order to account for variation within the samples—for each of the stratigraphic sections.

These errors were compounded and two plots with errors were made (one plus the error and one minus the error) for each of the stratigraphic sections at 1Kb. Figs. 2.13—2.15 show Sections 1 and 2 of Cerro Galan and Cerro Blanco plots with errors.

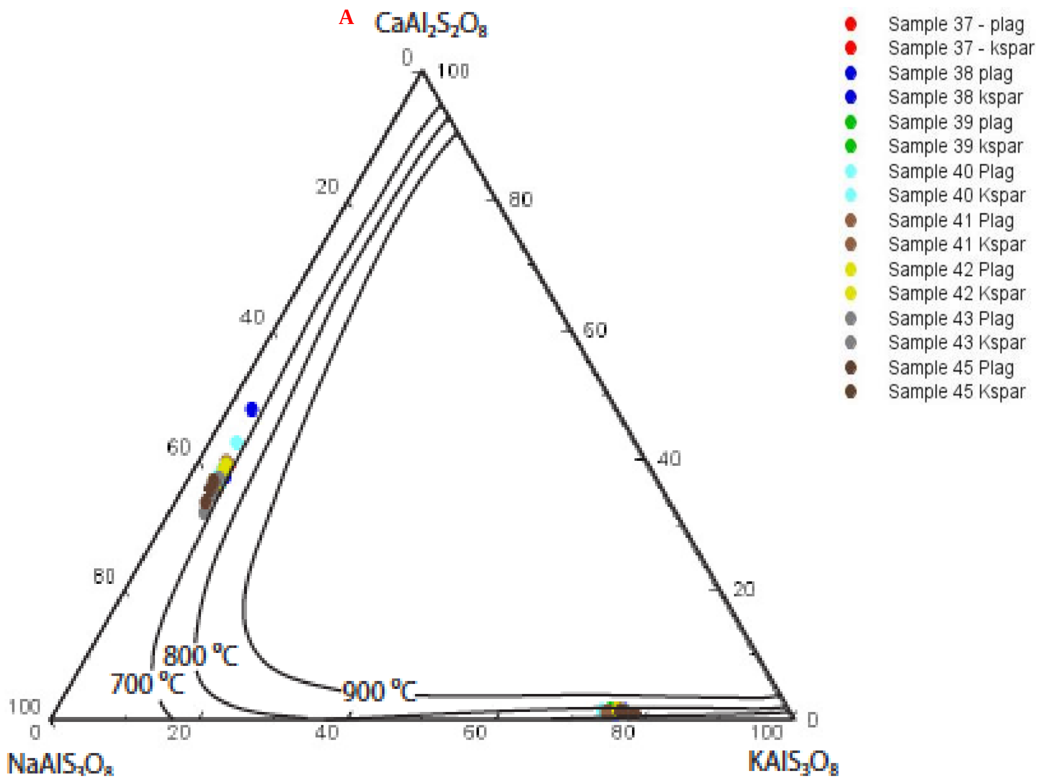

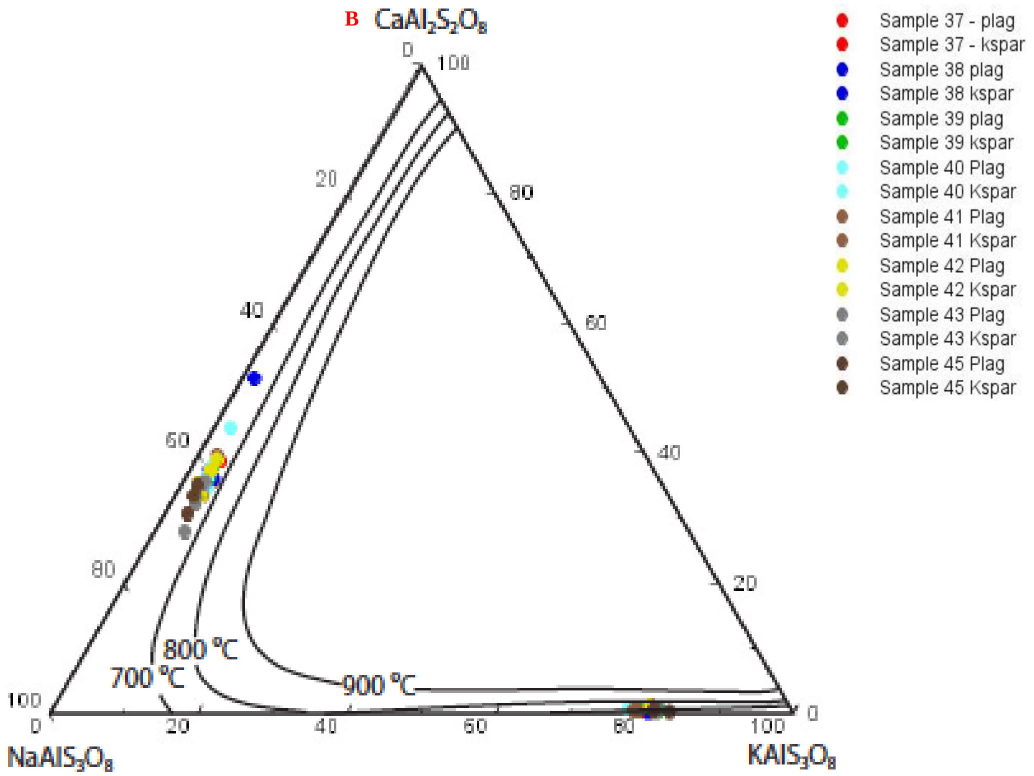

Fig.2.13. Section 1 feldspar thermometry (A) Plus error and (B) Minus error

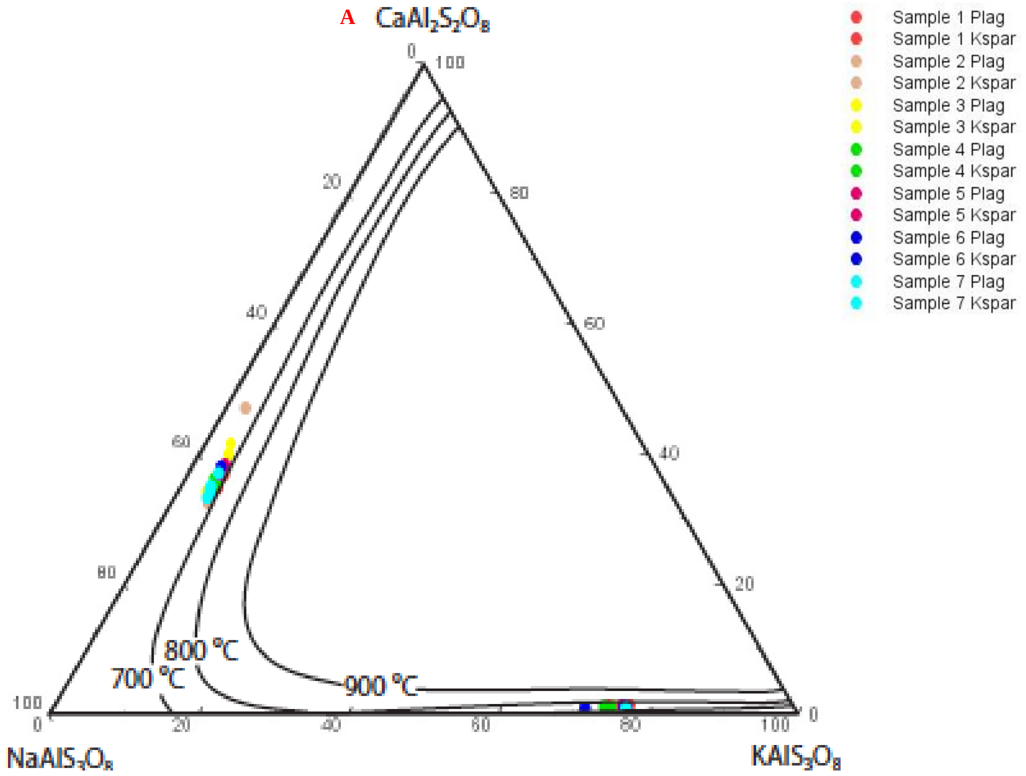

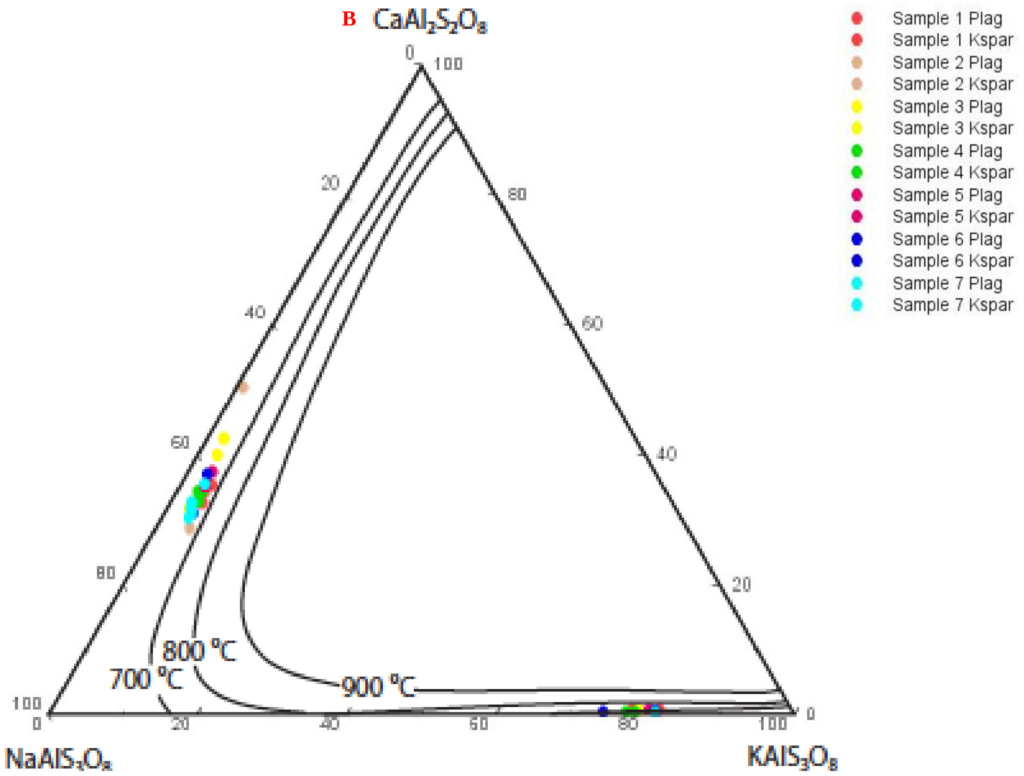

Fig.2.14. Section 2 feldspar thermometry (A) Plus error and (B) Minus error

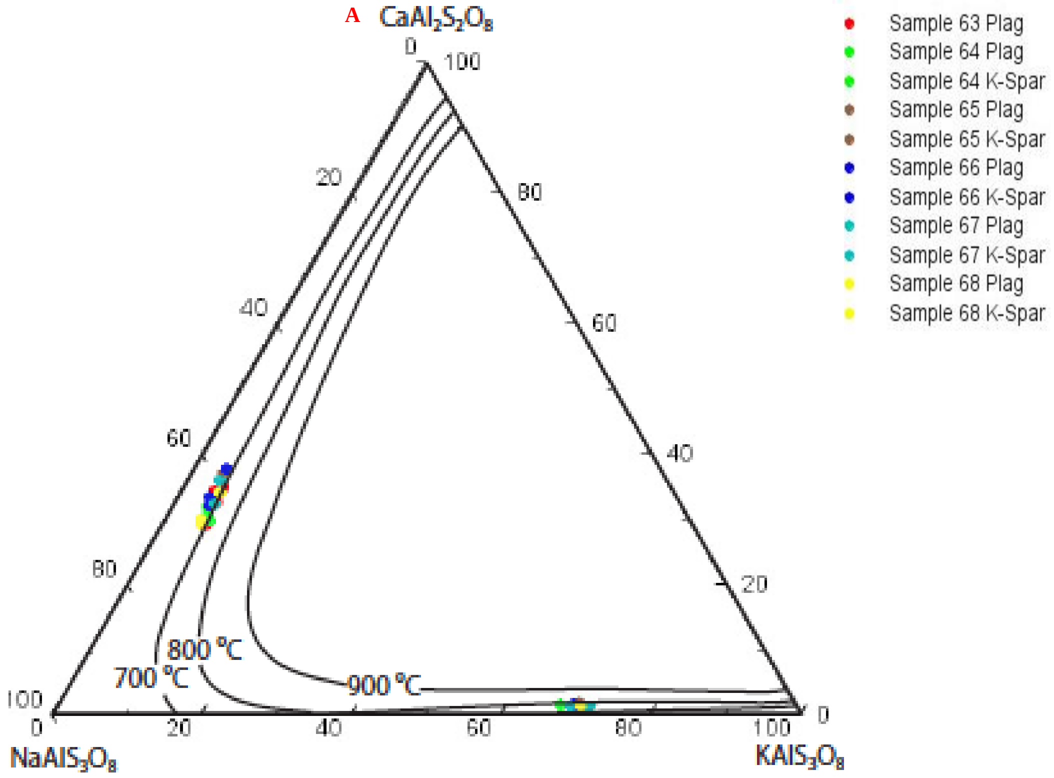

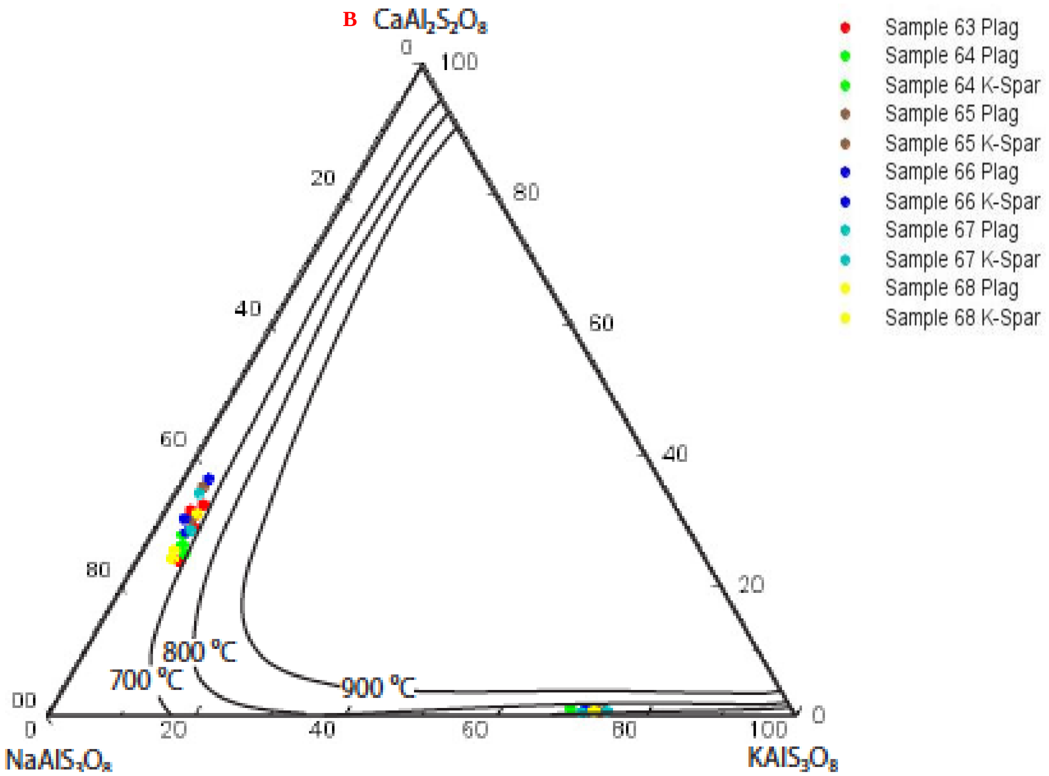

Fig.2.15. Cerro Blanco thermometry (A) Plus error and (B) Minus error

From figs. 2.13—2.15 it is observed that the temperature difference between this study and that of Folkes et al. (2011) cannot be explained by analytical and sample variation errors. In the A panels of figs. 2.13—2.15 a slight temperature increase of a few degrees is observed relative to plots without errors in figs. 2.1—2.3. Adding 15 ^{0}C, which is the estimated error obtained from calculating temperatures at 1 and 5 kb we obtain a maximum equilibrium temperature of approximately 715 ^{0}C. This temperature falls short of the 770-840 ^{0}C estimated by Folkes et al. (2011).

A possible source for temperature discrepancies between this and Folkes et al.'s (2011) study may be related to the minerals used to calculate equilibrium temperatures. Folkes et al. (2011) used Fe-Ti oxide minerals found in pumice clasts in order to estimate equilibrium temperatures in the CGI. Their temperatures may be incorrect because oxidation of the Fe-Ti oxides after emplacement is common in these minerals. The Fe-Ti oxide section of this investigation demonstrates that these minerals have been altered to various degrees. This alteration phenomenon is further supported by Francis et al.'s (1989) investigation which concluded that the Fe-Ti oxides in the CGI are commonly altered. Nonetheless, if temperatures calculated by Folkes et al. (2011) are right, then this may mean that the oxides analyzed in Folkes et al.'s (2011) study recorded a much earlier crystallization stage than the feldspars (which recorded eutectic crystallization of an H_2O rich magma).

Finally, ternary feldspar thermometry conducted in this investigation shows that equilibrium temperatures in Cerro Galan and Cerro Blanco were in the range of 650-700 ^{0}C at an inferred minimum pressure of 2kb. Moreover, feldspars analyzed in this study are interpreted to have recorded eutectic crystallization of magmas with approximately 4% H_2O. The fact that both calderas are very similar in terms of feldspar compositions and by consequence temperatures may indicate that both magma chambers underwent similar processes before their final eruption.

CHAPTER 3

Fe-Ti Oxides

Introduction

The occurrence and composition of the Fe-Ti oxides is a function of temperature, as well as oxygen fugacity (Andersen and Lindsley 1988; Frost 1991). At very low oxygen fugacities, such as those encountered in meteorites and the earth's core iron can exist with oxidation state of 0, however, with increasing oxygen fugacity iron occurs in minerals such as magnetite (Fe_3O_4) and hematite (Fe_2O_3) as either a divalent (ferrous) or trivalent (ferric) cation (Frost, Ronald 1991). In addition, the existence and composition of hematite and magnetite is directly related to magmatic temperatures, as these minerals represent end-members of two distinct solid solutions.

The ilmenite-hematite end-members are part of a solid solution series in which there is Fe-Ti cation exchange. Ilmenite is the ordered version of hematite in which cation sites are occupied with Fe^{2+} and Ti^{4+} instead of Fe^{3+}. In the case of the $FeTiO_3$ end member, Fe^{2+} and Ti^{4+} form alternating layers, known as A and B layers respectively. In the case of Fe_2O_3 A- and B-layers are both occupied by Fe^{3+} and are symmetrically equivalent (Harrison et al. 2000). Both end-members have rhombohedral (trigonal) structure based on the hexagonal closed packing (HCP) oxygen packing scheme (Lindsley 1991).

Similarly, magnetite forms a solid solution with ulvospinel (Fe_2TiO_4) in which Ti substitution takes place. Titanomagnetites have a spinel structure with 32 O atoms per unit cell arranged in cubic close-packed (CCP) layers forming (111) planes of a face-centered cubic lattice, defining two distinct cation sites—known as A and B—with four or six nearest O neighbors (Pearce et al. 2010).

Temperatures obtained by utilizing Fe-Ti concentration of the above mentioned solid solutions are a direct reflection of the equilibrium temperatures at which these minerals coexisted, assuming that no post-crystallization cation exchange or exolution occurred in the analyzed samples.

An attempt was made in this study to use compositions of the iron-titanium oxide pairs magnetite (Fe_3O_4)–ulvospinel (Fe_2TiO_4) and ilmenite ($FeTiO_3$)–hematite (Fe_2O_3), present in both ashflows, as geothermometers. Thermodynamic calculations were performed to estimate the equilibrium temperature of coexisting oxide solutions in order to determine the pre-eruptive temperatures of Cerro Galan and Cerro Blanco magma chambers. The most important aspect of this method is the assumption that the mineral pairs were at equilibrium at the time of the volcanic eruption.

A further implied assumption for the successful implementation of this method is that individual crystals in the area of study were under the same temperature and pressure conditions, (which is a safe assumption given that crystals-pairs had a maximum separation of only a few millimeters in the analyzed samples), and that post eruptive conditions did not adversely affect the original (pre-eruptive) Fe-Ti ratios. Finally, due to the geographical environment, weathering of samples—which would affect equilibrium composition of minerals—is not expected to be significant because these deposits were emplaced at high altitude where the climate is very dry. The floor of the caldera is approximately 4.5 km above sea level (Sparks et al. 1985) where chemical weathering is minimal.

Analytical Procedures

Electron Microprobe Analyses

Fe-Ti oxides microprobe analyses were performed following the same procedures described in feldspar thermometry. Tables 3.1—3.6 show ilmenite and magnetite oxide compositions for sections 1 & 2 of Cerro Galan and Cerro Blanco.

Table 3.1. Section 1 Cerro Galan ilmenite compositions obtained by electron microprobe analyses

Ilmenite oxide weight percent									
Label	**SiO2**	**TiO2**	**Al2O3**	**MgO**	**FeO**	**CaO**	**MnO**	**Cr2O3**	**Ni**	**Total**
A07_37OX_2	0.00	33.04	0.72	1.52	56.06	0.00	0.83	0.00	0.00	92.16
A07_37OX_5	0.00	45.74	0.50	1.04	44.94	0.00	0.79	0.00	0.00	93.00
A07_38OX_1	0.00	44.39	0.53	1.29	47.82	0.00	0.44	0.00	0.00	94.48

A07_38OX_2	0.00	44.77	0.64	1.13	45.89	0.00	0.39	0.00	0.00	92.82
A07_38OX_3	0.00	30.52	0.56	1.21	49.42	0.00	0.55	0.00	0.00	82.27
A07_38OX_4	0.00	43.80	0.56	0.87	40.74	0.00	0.66	0.00	0.00	86.62
A07_39OX_2	0.06	32.59	1.35	1.78	55.81	0.00	0.83	0.00	0.00	92.42
A07_39OX_4	0.00	42.12	0.45	1.20	47.53	0.00	0.67	0.00	0.00	91.96
A07_39OX_5	0.00	33.47	0.70	1.49	55.40	0.00	0.68	0.00	0.00	91.74
A07_40OX_4	0.00	43.46	0.39	1.09	48.25	0.00	0.60	0.00	0.00	93.79
A07_41OX_2	0.05	44.92	0.45	1.05	46.56	0.03	0.45	0.00	0.02	93.53
A07_42OX_1	0.03	43.80	0.29	0.99	47.03	0.02	0.50	0.03	0.13	92.83
A07_42OX_2	1.46	39.54	0.85	1.42	46.88	0.07	0.44	0.00	0.09	90.75
A07_42OX_3	0.82	32.50	0.28	1.68	54.71	0.04	0.34	0.04	0.00	90.41
A07_42OX_4	1.67	40.08	0.49	2.10	45.97	0.01	0.46	0.00	0.00	90.78
A07_43OX_1	0.00	24.94	1.18	1.97	63.05	0.00	0.66	0.06	0.05	91.91
A07_43OX_2	0.01	41.83	0.37	1.11	48.46	0.03	0.43	0.06	0.00	92.29
A07_43OX_4	0.00	35.52	0.25	1.02	55.05	0.01	0.50	0.00	0.00	92.35
A07_43OX_3	0.00	48.75	0.24	1.14	42.39	0.00	0.40	0.01	0.00	92.93
A07_44Ox_6	0.00	44.48	0.06	0.34	49.62	0.18	1.55	0.00	0.00	96.22
A07_45Ox_1	0.00	37.76	0.42	0.93	55.50	0.00	0.39	0.00	0.00	95.00
A07_45Ox_2	0.00	36.00	0.20	1.15	56.75	0.03	0.50	0.00	0.00	94.63

Table 3.2. Section 1 Cerro Galan magnetite compositions obtained by electron microprobe analyses

Magnetite oxide weight percent										
Label	**SiO2**	**TiO2**	**Al2O3**	**MgO**	**FeO**	**CaO**	**MnO**	**Cr2O3**	**Ni**	**Total**
A07_37OX_1B	0.00	9.50	0.82	1.95	76.97	0.00	0.75	0.00	0.00	89.98
A07_37OX_3	0.00	2.78	1.66	0.55	83.49	0.00	0.33	0.00	0.00	88.81
A07_37OX_4	0.12	6.55	1.96	0.46	80.41	0.00	0.25	0.00	0.00	89.75
A07_38OX_4B	0.00	3.73	2.28	1.37	81.34	0.00	0.84	0.00	0.00	89.56
A07_38OX_5	0.06	2.30	2.87	0.71	82.78	0.00	0.59	0.00	0.00	89.30
A07_39OX_1	0.00	6.32	2.23	0.69	81.72	0.00	0.45	0.00	0.00	91.41
A07_39OX_3	0.10	7.75	2.43	0.63	79.40	0.00	0.51	0.00	0.00	90.82
A07_40OX_1	0.08	4.66	2.36	0.51	83.32	0.00	0.24	0.00	0.00	91.18
A07_40OX_2	0.00	5.73	2.76	0.59	81.08	0.00	0.20	0.00	0.00	90.36
A07_40OX_3	0.09	3.03	2.44	0.49	83.33	0.05	0.44	0.00	0.00	89.87
A07_41OX_5	0.10	1.82	9.48	2.59	77.50	0.00	0.09	0.20	0.05	91.83
A07_42OX_5	1.35	2.62	1.86	0.67	76.87	0.06	0.54	0.39	0.09	84.44
A07_43OX_6	0.10	5.16	3.02	0.64	79.40	0.00	0.06	0.13	0.05	88.56

A07_44B_5	3.99	0.22	3.11	2.54	84.40	1.25	0.17	0.00	0.00	95.67
A07_44Ox_1	3.29	0.67	2.14	1.94	82.99	0.80	0.29	0.00	0.00	92.13
A07_44Ox_2	0.07	0.00	0.03	0.00	90.59	0.14	0.00	0.00	0.00	90.83
A07_44Ox_3	0.18	0.00	0.29	0.08	87.97	0.17	0.00	0.00	0.85	89.54
A07_44Ox_4	0.73	0.18	0.37	0.13	87.40	0.20	0.00	0.00	0.56	89.57
A07_44Ox_5	3.33	0.53	2.50	1.04	85.14	1.00	0.00	0.00	0.00	93.55
A07_45Ox_3	0.00	20.80	0.24	1.06	70.00	0.00	0.37	0.01	0.00	92.48
A07_45Ox_4	0.31	0.29	3.52	0.31	87.09	0.04	0.52	0.00	0.00	92.07

Table 3.3. Section 2 Cerro Galan ilmenite compositions obtained by electron microprobe analyses

Ilmenite oxide weight percent										
Label	**SiO2**	**TiO2**	**Al2O3**	**MgO**	**FeO**	**CaO**	**MnO**	**Cr2O3**	**Ni**	**Total**
A07_02_OX_3	0.07	48.28	0.11	1.45	47.01	0.04	1.22	0.00	0.00	98.17
A07_02_OX_4	5.39	42.73	2.18	1.33	44.64	0.57	1.28	0.14	0.05	98.31
A07_02_OX_5	0.08	47.58	0.25	1.42	46.95	0.02	1.14	0.04	0.03	97.50
A07_03_OX_2	0.04	35.81	0.27	1.03	57.94	0.01	0.55	0.00	0.00	95.65
A07_03_OX_5	0.04	34.33	0.24	0.84	60.34	0.01	0.62	0.04	0.00	96.45
A07_04_OX_2	0.08	42.35	0.19	1.38	50.24	0.06	1.12	0.00	0.01	95.44
A07_04_OX_3	0.10	39.78	0.22	1.14	52.42	0.02	1.06	0.03	0.00	94.77
A07_04_OX_4	0.07	35.69	0.17	0.86	57.76	0.01	0.67	0.08	0.00	95.32
A07_04_OX_5	0.04	35.94	0.22	0.80	58.12	0.01	0.85	0.10	0.00	96.08
A07_05_OX_2	0.01	36.98	0.16	0.98	55.49	0.02	1.25	0.08	0.00	94.97
A07_05_OX_4	0.00	35.53	0.20	1.12	55.63	0.02	1.33	0.04	0.01	93.88
A07_05_OX_5	0.15	34.21	0.25	0.71	57.75	0.13	0.68	0.10	0.00	93.98
A07_06_OX_3	0.09	36.90	0.23	0.94	55.60	0.03	1.49	0.06	0.00	95.34
A07_06_OX_4	0.07	35.04	0.22	0.87	56.64	0.04	1.52	0.00	0.00	94.39
A07_07_Ox_1	0.00	35.93	0.15	0.82	58.37	0.02	1.10	0.00	0.02	96.42
A07_07_Ox_3	0.03	35.42	0.20	0.91	58.68	0.00	0.79	0.07	0.04	96.14
A07_07_Ox_5	0.06	36.14	0.25	0.92	56.10	0.02	1.05	0.00	0.08	94.60
A07_01_OX_1	0.04	37.31	0.15	1.05	57.22	0.00	0.96	0.02	0.04	96.80
A07_01_OX_2	0.05	37.35	0.19	1.17	55.66	0.04	0.99	0.06	0.00	95.50
A07_01_OX_3	0.09	37.14	0.20	1.10	55.58	0.08	1.10	0.00	0.03	95.33
A07_01_OX_4	0.03	37.39	0.16	0.98	56.67	0.03	0.97	0.00	0.00	96.23
A07_01_OX_5	0.07	37.57	0.21	1.12	56.18	0.04	0.91	0.07	0.01	96.19

Table 3.4. Section 2 Cerro Galan magnetite compositions obtained by electron microprobe analyses

Magnetite oxide weight percent										
Label	**SiO2**	**TiO2**	**Al2O3**	**MgO**	**FeO**	**CaO**	**MnO**	**Cr2O3**	**Ni**	**Total**
A07_02_OX_1	0.54	3.76	3.13	0.63	83.57	0.01	0.40	0.06	0.00	92.10
A07_03_OX_1	0.13	4.34	2.28	0.68	83.35	0.03	0.50	0.11	0.11	91.52
A07_03_OX_3	0.10	4.32	2.37	0.52	86.13	0.02	0.52	0.08	0.00	94.05
A07_03_OX_4	0.15	3.47	2.55	0.51	84.97	0.03	0.62	0.10	0.00	92.40
A07_04_OX_1	0.11	3.74	1.76	0.58	85.85	0.02	0.69	0.12	0.00	92.86
A07_05_OX_1	0.13	3.89	1.72	0.46	84.51	0.05	0.94	0.17	0.00	91.87
A07_05_OX_3	0.09	3.43	1.78	0.48	84.85	0.04	1.02	0.05	0.01	91.75
A07_06_OX_1	0.12	3.31	1.36	0.46	85.17	0.04	0.76	0.00	0.00	91.22
A07_06_OX_2	0.09	3.72	1.32	0.51	84.99	0.01	0.65	0.05	0.04	91.38
A07_07_Ox_2	0.08	6.20	0.99	0.57	82.35	0.06	0.99	0.17	0.00	91.40
A07_07_Ox_4	0.02	3.74	1.37	0.53	87.96	0.00	0.73	0.10	0.03	94.48
A07_07_Ox_6	0.03	3.94	1.36	0.64	84.97	0.02	0.67	0.02	0.00	91.65

Table 3.5. Cerro Blanco ilmenite compositions obtained by electron microprobe analyses

Ilmenite oxide weight percent										
Label	**SiO2**	**TiO2**	**Al2O3**	**MgO**	**FeO**	**CaO**	**MnO**	**Cr2O3**	**Ni**	**Total**
A07_65_Ox_1	0.00	36.11	0.22	2.14	56.34	0.00	1.34	0.00	0.00	96.14
A07_65_Ox_2	0.00	38.45	0.18	1.73	53.08	0.00	1.26	0.00	0.00	94.70
A07_65_Ox_3	0.00	37.50	0.22	1.35	53.15	0.00	0.79	0.00	0.00	93.01
A07_65_Ox_4	0.00	37.14	0.17	2.22	52.65	0.06	1.35	0.00	0.00	93.58
A07_64_Ox_2	0.00	39.21	0.20	0.97	53.56	0.06	0.80	0.00	0.00	94.80
A07_63_Ox_1	0.00	36.05	0.15	2.61	54.10	0.00	1.16	0.00	0.00	94.07
A07_63_Ox_4	0.00	43.25	0.21	4.59	40.37	0.05	2.20	0.00	0.00	90.67

Table 3.6. Cerro Blanco magnetite compositions obtained by electron microprobe analyses

Magnetite oxide weight percent									
Label	**SiO2**	**TiO2**	**Al2O3**	**MgO**	**FeO**	**CaO**	**MnO**	**Cr2O3**	**Ni**	**Total**
A07_68_Ox_1	0.30	2.16	0.23	0.22	85.20	0.00	0.33	0.00	0.00	88.45
A07_68_Ox_3	0.10	1.67	0.22	0.35	84.37	0.00	0.41	0.00	0.00	87.11
A07_68_Ox_4	0.00	10.20	0.52	0.67	74.06	0.00	0.32	0.00	0.00	85.77
A07_68_Ox_5	0.29	13.63	0.31	0.93	71.51	0.00	0.93	0.00	0.00	87.61
A07_67_Ox_1	0.59	6.70	0.80	2.84	73.36	0.26	3.13	0.00	0.00	87.68
A07_67_Ox_2	0.22	6.49	0.41	3.20	74.29	0.00	2.94	0.00	0.00	87.55
A07_67_Ox_3	0.00	6.78	0.46	3.50	74.41	0.00	2.74	0.00	0.00	87.89
A07_67_Ox_4	0.16	3.72	0.35	1.82	77.92	0.05	2.65	0.00	0.00	86.67
A07_67_Ox_5	0.37	5.57	0.68	2.17	74.58	0.00	2.83	0.00	0.00	86.20
A07_66_Ox_1	0.08	5.32	1.46	0.39	83.97	0.00	0.00	0.00	0.00	91.22
A07_66_Ox_1B	0.12	5.40	1.93	0.18	72.86	0.07	0.23	0.00	0.00	80.79
A07_66_Ox_2	0.08	0.00	0.00	0.00	89.51	0.00	0.00	0.00	0.00	89.59
A07_66_Ox_3	0.06	0.03	0.05	0.00	90.42	0.05	0.00	0.00	0.00	90.61
A07_66_Ox_4	0.06	0.00	0.00	0.00	88.53	0.00	0.00	0.00	0.00	88.59
A07_65_Ox_5	0.09	4.94	1.35	0.84	82.22	0.00	0.90	0.00	0.00	90.33
A07_64_Ox_1	0.05	3.96	0.15	0.31	84.32	0.00	0.84	0.00	0.00	89.63
A07_64_Ox_3	0.30	3.92	0.38	2.06	78.31	0.00	2.59	0.00	0.00	87.56
A07_64_Ox_4	0.06	5.12	1.28	0.98	82.88	0.00	1.27	0.00	0.00	91.59
A07_64_Ox_5	0.00	5.23	1.63	0.12	83.64	0.00	0.00	0.00	0.00	90.61
A07_63_Ox_2	0.05	4.47	0.96	1.37	84.44	0.00	1.04	0.00	0.00	92.32
A07_63_Ox_3	0.08	2.71	1.13	2.64	81.77	0.00	1.61	0.00	0.00	89.93
A07_63_Ox_5	0.00	2.58	0.58	0.43	85.53	0.00	0.31	0.00	0.00	89.43

Fe-Ti Oxide Structural Formulae Calculations

Ilmenite - hematite oxide concentrations were recalculated to 6 charges and 2 cations based on the structural formula of the solid solution $FeTiO_3$ - Fe_2O_3. Magnetite – ulvospinel oxide concentrations were recalculated to 8 charges and 3 cations based on the structural formula of the solid solution Fe_3O_4 - Fe_2TiO_4. In addition, oxide analyses to be used for thermodynamic calculations were selected on the basis of cation total—2 (+/- 0.1) for the hematite solid solution and 3 (+/- 0.1) in the magnetite solid solution series—and positive values for both Fe^{2+} and Fe^{3+} concentration.

Iron oxides were separated into ilmenite and magnetite based on the amount of FeO and TiO obtained from microprobe analyses following Deer et al.'s (1992) representative compositions for ilmenite and magnetite. Ilmenite was selected based on FeO weight percent ranging from 40-60 % with the remainder of the weight percent being mainly TiO_2 and minor traces of other elements. Magnetite was selected on the basis of FeO weight percent content greater than 70 with the remaining weight % being mostly titanium oxide with minor traces of other elements.

Fe-Ti Oxides vs. Vertical Location

Plots for Fe^{3+}, Fe^{2+}, and Ti were made for ilmenite and magnetite for each of the sections (sections 1and 2 of Cerro Galan and Cerro Blanco) as a function of vertical location. Each data point in (figs 3.1–3.6) represents the mode (most common) cation concentration for each of the vertical locations within a stratigraphic section In other words, each point in the graphs below represents a vertical location within a stratigraphic section and each point was selected from a number of analyses of the same vertical location.

Error for the Fe-Ti oxides was calculated based on the analytical error calculated from standard ilmenite and magnetite minerals. The standard deviations of Fe^{3+}, Fe^{2+}, and Ti concentrations were calculated for standard minerals and this value was added and subtracted to actual concentrations in order to define the high and low values of the analyses. These high and low values define the error bars depicted below. The errors for Fe^{3+}, Fe^{2+}, and Ti are (+/-) 0.057, 0.026, and 0.028 respectively for ilmenite cation concentrations. The errors for Fe^{3+}, Fe^{2+}, and Ti are (+/-) 0.006, 0.003, and 0.002 respectively for magnetite cation concentrations. In the case of magnetite analyses error bars are smaller than data point markers and therefore not visible.

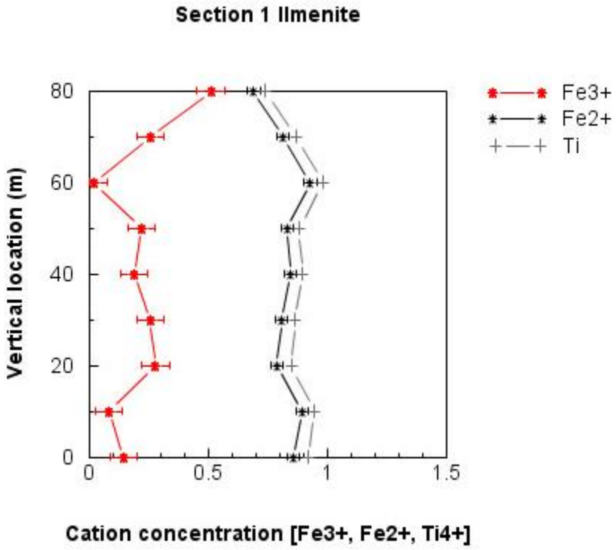

Fig.3.1. Section 1 Cerro Galan Fe^{2+}, Fe^{3+}, and Ti in ilmenite vs. vertical location

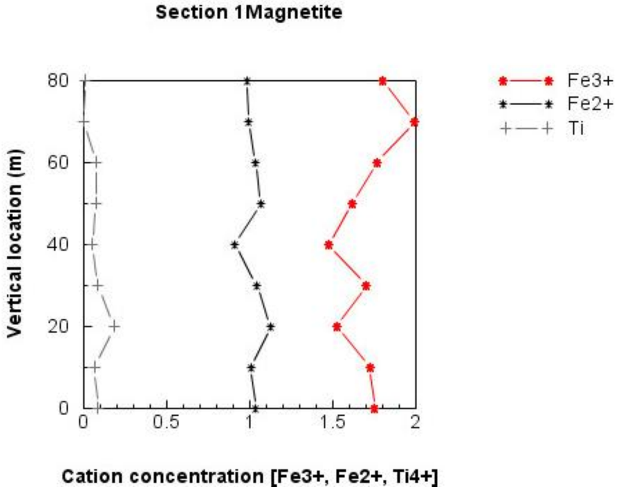

Fig.3.2. Section 1 Cerro Galan Fe^{2+}, Fe^{3+}, and Ti in magnetite vs. vertical location. Error bars are smaller than data point markers.

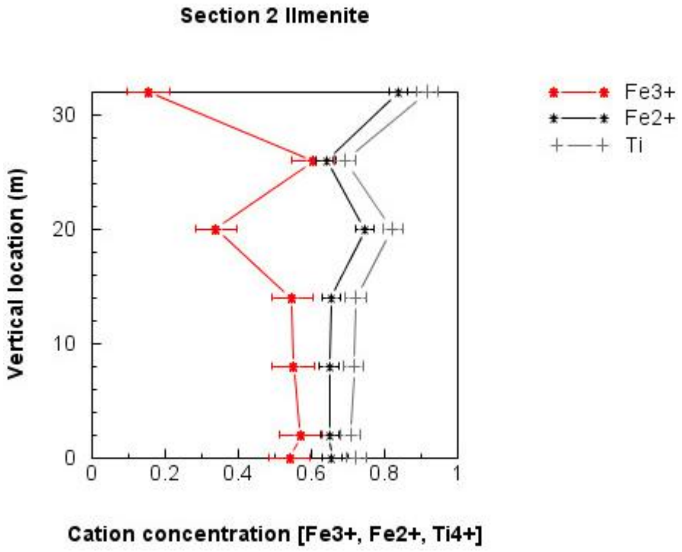

Fig.3.3. Section 2 Cerro Galan Fe^{2+}, Fe^{3+}, and Ti in ilmenite vs. vertical location

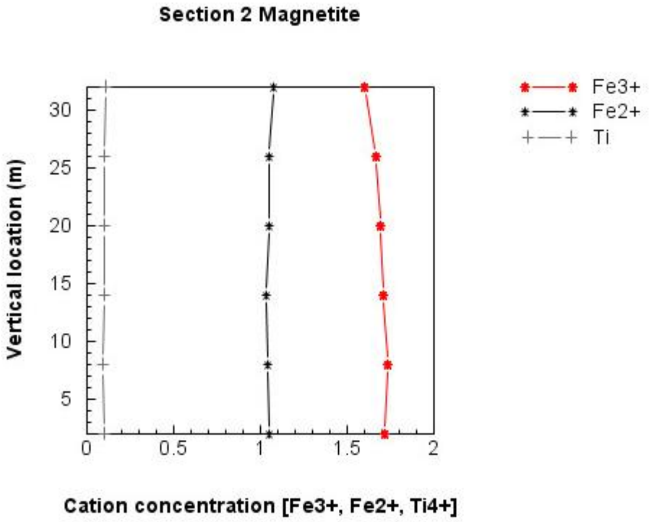

A07 01 (bottom of section) does not have a magnetite

Fig.3.4. Section 2 Cerro Galan Fe^{2+}, Fe^{3+}, and Ti in magnetite vs. vertical location. Error bars are smaller than data point markers.

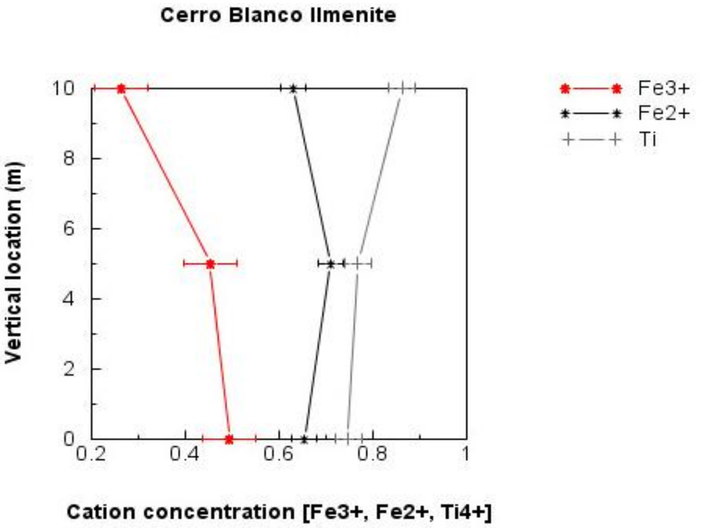

Samples A07 66-68 have no ilmenites

Fig.3.5. Cerro Blanco Fe^{2+}, Fe^{3+}, and Ti in ilmenite vs. vertical location

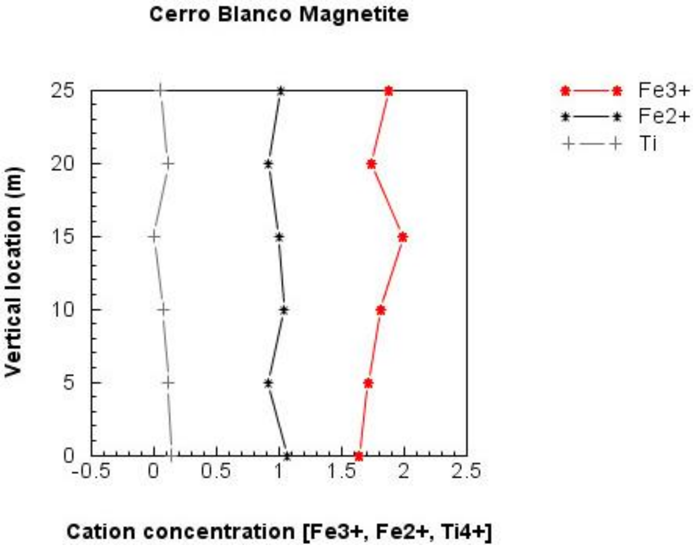

Fig.3.6. Cerro Blanco Fe^{2+}, Fe^{3+}, and Ti in magnetite vs. vertical location. Error bars are smaller than data point markers.

Thermodynamic Framework

The phase assemblage consists of a rhombohedral phase (ilmenite-hematite solid solution) and a cubic phase (magnetite-ulvospinel solid solution). Based on the mineralogy of this phase assemblage we can write the following phase equilibrium:

(1) $Fe_2TiO_4 + Fe_2O_3 \rightleftarrows FeTiO3 + Fe3O4$

Ulvospinel Hematite Ilmenite Magnetite

From this equation and the fact that the minerals (phases) represent solid solutions we can use thermodynamic equations in order to solve for the temperature at which the minerals in this study equilibrated. The key assumption for the following definitions is that the system was at equilibrium. From thermodynamics we know that at equilibrium:

(2) $\Delta G = \Delta G^0_{(P,T)} + RT \ln K = 0$

we also know that for solid phase equilibria,

(3) $\Delta G^0_{(P,T)} = \Delta G^0_{(1,T)} + (P-1)\Delta V_{(solids)}$

where the -1 in the equation is the result of integration of pressure from 1 bar (standard state) to the pressure of interest.

Moreover, from thermodynamics we know that for equilibria with only solid mineral phases,

(4) $\Delta G = \Delta G^0_{1,T} + (P-1)^* \Delta V_{solids} + RT\ln K = 0$

In addition, from eqn. 1 we can define K in terms of ideal activity as follows,

(5) $K = ([a_{ilm}]^*[a_{mag}] / [a_{ulv}]^*[a_{hem}])$

So,

(6) $\Delta G = \Delta G^0_{1,T} + (P-1)^* \Delta V_{solids} + RT\ln ([a_{ilm}]^*[a_{mag}] / [a_{ulv}]^*[a_{hem}]) = 0$

Where G =Gibbs free energy change for reaction (1); $G^0_{1,T}$ = standard state Gibbs free energy at 1bar and temperature T; P = pressure; R = ideal gas constant; T = temperature; and a = ideal activity;

Equation 6 allows us to calculate the crystallization temperature at equilibrium for an ideal solution. In this study nonetheless we seek to find the crystallization temperature for a real solution. In order to calculate temperatures for real solutions we must use real activities of the minerals (it should be noted that the temperature at which minerals crystallized in the magma chambers is fixed but the calculated temperature we obtain from using real vs. ideal activities changes when using one versus the other). Using real activities equation 6 becomes,

(7) $\Delta G = \Delta G^0_{1,T} + (P-1)* \Delta V_{solids} + RT\ln ([a_{ilm}]_{real}*[a_{mag}]_{real} / [a_{ulv}]_{real}*[a_{hem}]_{real}) = 0$

Data for real activities was obtained from Ghiorso and Sack (1991) at 800 ^{0}C. Based on the assumption that the oxides analyzed in this study equilibrated at magmatic conditions, 800 ^{0}C is a reasonable initial temperature to base excess mixing properties, considering that both calderas erupted silicic magmas. In order to accomplish this, the first step was to calculate mole fractions of hematite (or ilmenite) in the hematite-ilmenite solid-solution series and magnetite (or ulvospinel) in the magnetite-ulvospinel solid-solution series. These mole fractions were then plotted on real activity models at 800 ^{0}C (fig.3.7) from Ghiorso and Sack (1991) and activities were directly obtained.

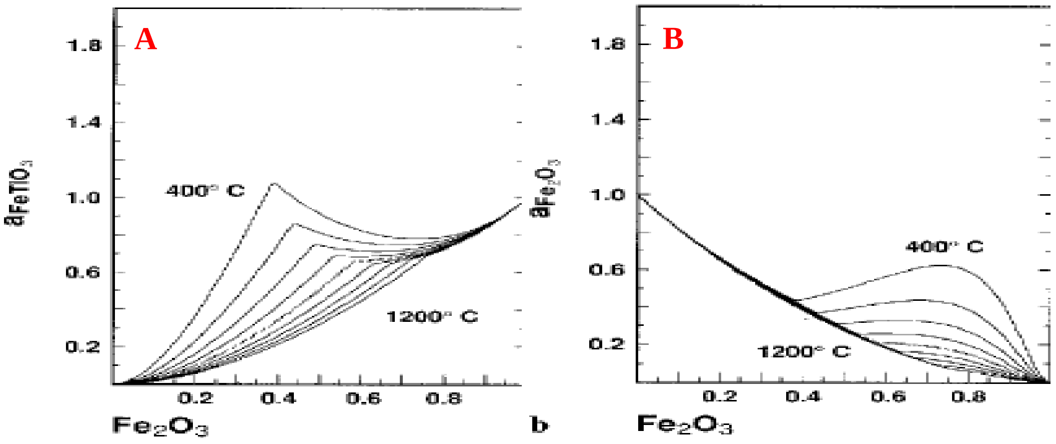

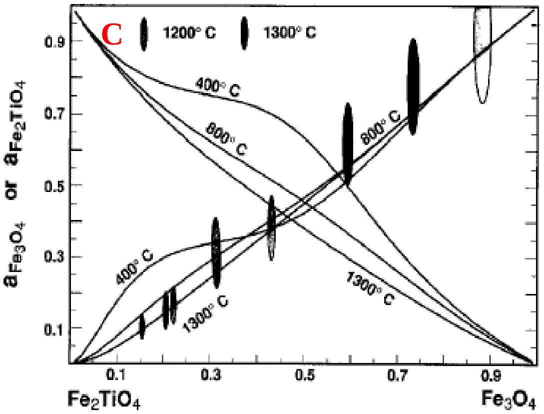

Fig.3.7. Real activity vs. mole fractions for ilmenite-hematite (A & B) and magnetite-ulvospinel (C) solid solutions. Taken from Ghiorso and Sack (1991).

From the above information we observe that we have one equilibrium reaction and two unknowns: pressure (P) and temperature (T). In order to solve for these independent variables we define one of the variables, in this case pressure at 1and 5 kb—which is the range at which these magmas are inferred to have existed before eruption (refer to feldspar section for more details)—and solve for temperature. Molar concentrations are obtained from recalculated microprobe data. Other parameters such as molar volumes (assumed constant for solids), enthalpy, entropy, and heat capacity needed to calculate Gibbs free energy of reaction at 1 and 5 bars and a temperature T ($G^0_{(1,T)}$) were obtained from Holland and Powell's (1998) thermodynamic data set compilation.

Finally, once all the thermodynamic data necessary to mathematically solve the phase equilibriums was obtained ©Maple 14 mathematical software was used in order to solve for temperature. Parameters other than temperature were specified in equation (7) and the mathematical software calculated a temperature that made $\Delta G = 0$ ($\Delta G = 0$ at equilibrium as discussed above). The temperatures obtained in these calculations represent equilibrium temperatures of the system as recorded by mineral compositions.

Results and Discussion

Tables 3.7–3.9 show temperatures calculated for each of both sections of Cerro Galan and Cerro Blanco.

Table 3.7. Section 1 Cerro Galan temperatures calculated at 1 and 5 kb

Sample_ilm#_mag#	**Temperature at 1kb (^{0}C)**	**Temperature at 5 kb (^{0}C)**
45_2 & 5	351.98	361.11
45_ 2 & 4	151.78	157.99
45_ 1 & 4	145.65	157.99
45_ 1 & 5	338.84	347.77
44_6 & 1	161.56	163.19
44_6 & 4	100.68	106.19
44_6 & 5	139.89	145.94
43_1 & 6	516.73	528.32
43_ 2 & 6	347.43	356.49
43_ 3 & 6	17.22	21.53
42_3 & 5	282.42	290.51
42_2 & 5	307.67	316.13
42_1 & 5	242.65	250.15
42_4 & 5	299.14	307.48
41_2 & 5	174.75	181.28
40_4 & 2	348.79	357.87
40_4 &1	303.85	312.26
40_4 &3	274.62	282.59
39_2 & 3	580.41	592.88
39_2 & 1	482.37	493.47
39_4 & 1	372.35	381.79
39_4 & 3	442.46	452.96
38_3 &B	369.85	379.25
38_3 & 5	281.48	289.56
38_1 & 4B	268.21	276.08
38_1 & 5	204.29	211.24
38_2& 4B	237.20	244.62
38_2 & 5	179.97	186.57
37_2 & 1B	624.1	637.13
37_2 & 3	337.19	346.09
37_2 & 4	518.11	529.72
37_5 & 1B	342.58	351.57
37_5 & 3	193.04	199.84
37_5 & 4	290.93	299.14

Table 3.8. Section 2 Cerro Galan temperatures calculated at 1 and 5 kb

Sample_ilm#_mag#	Temperature at 1 kb (^{0}C)	Temperature at 5 kb (^{0}C)
02_4 & 1	229.88	237.20
02_3 & 1	216.06	223.18
02_5 & 1	216.06	223.18
03_5 & 1	395.18	404.97
03_ 5 & 3	389.47	399.17
03_ 5 & 4	379.74	389.29
03_ 2 & 4	369.25	378.64
03_ 2 &1	384.19	393.80
03_ 2 &3	378.66	388.20
04_4 & 1	358.91	368.14
04_5 & 1	358.91	368.14
04_2 & 1	298.36	306.69
04_3 & 1	316.97	325.57
05_5 & 1	377.90	387.42
05_5 & 3	365.97	375.31
05_2 & 3	352.23	361.36
05_4 & 3	358.86	368.09
05_4 & 1	370.52	379.93
05_2 & 1	363.64	372.95
06_4 & 2	366.08	375.43
06_ 4 & 1	371.51	380.93
06_ 3 & 1	507.52	518.98
06_ 3 & 2	359.76	369.01
07_3 & 2	467.75	478.63
07_ 3 & 4	366.98	376.34
07_ 3 & 6	374.52	383.99
07_ 1 & 6	374.52	383.99
07_ 1 & 2	467.75	478.63
07_ 1 & 4	366.98	376.34
07_ 5 & 4	359.85	369.10
07_ 5 & 6	367.22	376.58
07_ 5 & 2	458.17	468.91

Table 3.9. Cerro Blanco temperatures calculated at 1 and 5 kb

Sample_ilm#_mag#	Temperature at 1 kb (^{0}C)	Temperature at 5 kb (^{0}C)
63_1 & 2	386.03	395.67
63_1 & 3	298.19	306.51
63_1 & 5	322.64	331.32
63_4 & 5	322.64	331.32
63_4 & 2	290.47	298.67
63_4 & 3	225.15	232.40
64_2 & 5	403.73	413.64
64_2 & 1	346.17	355.21
64_2 & 3	369.50	378.90
64_2 & 4	387.66	397.33
65_1 & 5	409.49	419.49

65_2 & 5	383.90	393.52
65_3 & 5	383.90	393.52
65_4 & 5	394.08	403.84

Crystallization conditions obtained from feldspar thermometry for both Cerro Galan and Cerro Blanco indicate that temperature for both calderas was about 700 ^{0}C at an inferred pressure of 2 kb and 4% H_2O (see feldspar section for a more in depth explanation). Tables 3.7—3.9 show that temperatures obtained from Fe-Ti oxide calculations for the three analyzed sections do not match those obtained from feldspar thermometry and are too low to represent magmatic temperatures. This combined with the erratic behavior seen within samples—which represent same vertical location—and also between samples suggests that there was extensive post-emplacement oxidation of the Fe-Ti oxides; thus, oxide temperatures cannot be used to make inferences about magmatic conditions.

In order to determine the source of variability, ilmenite vs. hematite, and magnetite vs. ulvospinel molar fractions for all samples in both calderas were plotted (figs.3.8—3.10).

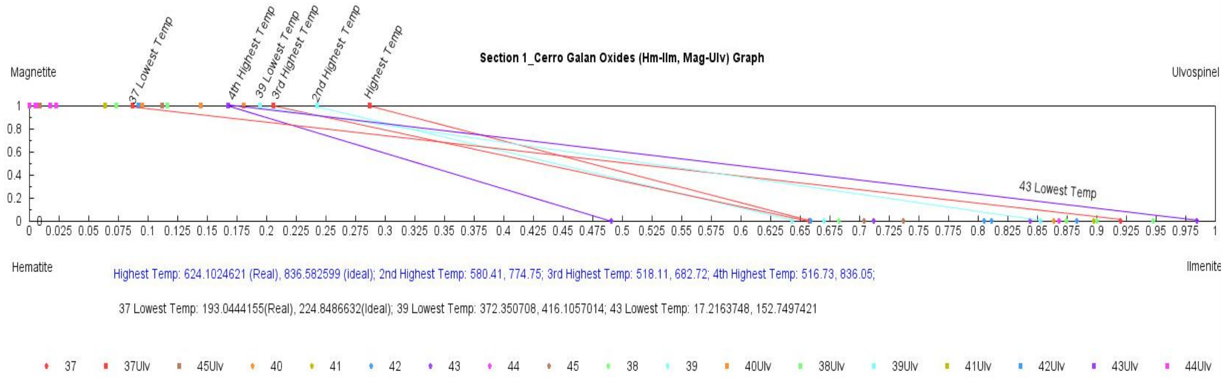

Fig.3.8. Section 1 Cerro Galan ilmenite-magnetite pairs used for thermodynamic calculations. Samples are color coded and numbered at the bottom of figure.

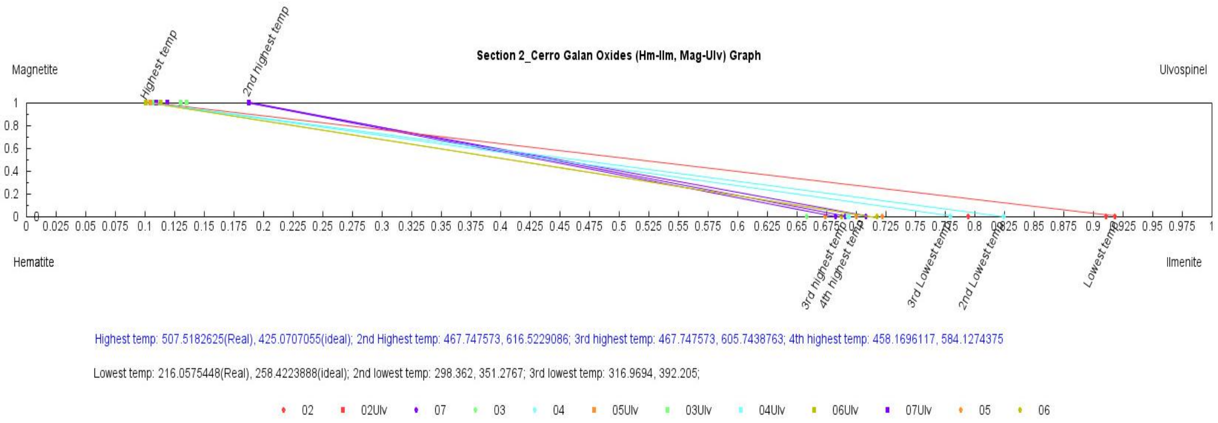

Fig.3.9. Section 2 Cerro Galan ilmenite-magnetite pairs used for thermodynamic calculations. Samples are color coded and numbered at the bottom of figure.

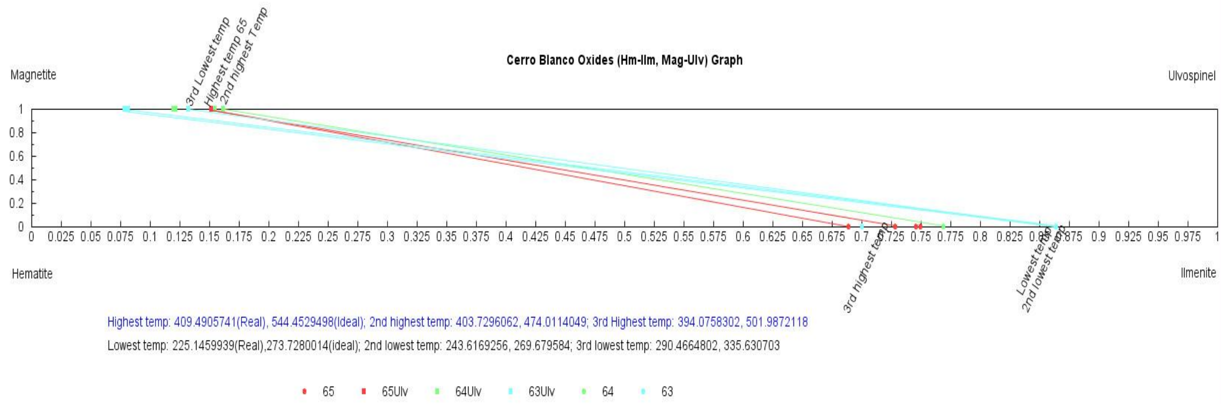

Fig.3.10. Cerro Blanco ilmenite-magnetite pairs used for thermodynamic calculations. Samples are color coded and numbered at the bottom of figure.

Variation in Fe-Ti Oxides

As can be seen from figures 3.8—3.10 the source of the variability in temperatures is due to the wide ranging compositions of ilmenite. This is likely due to exsolution in individual crystals to different degrees. This is further supported by the erratic trend in Fe^{3+}, Fe^{2+}, and Ti^{4+} vs. vertical location observed for ilmenites in figs. 3.1—3.6. Variation in ilmenites cannot be attributed to a compositional gradient in the magma chamber, but rather to external processes that influenced the evolution of compositions in the minerals present. This assertion is based on the fact that temperatures from the oxides are not high enough to represent magmatic temperatures –equilibrium temperatures were estimated to be about 700 ^{0}C for both calderas from feldspar thermometry—as well as investigations from previous workers in the Cerro Galan ignimbrite, which found no evidence that suggests the occurrence of compositional zonation in the Cerro Galan magma chamber (Sparks 1985, Francis et al. 1989).

As described by Ghiorso and Evans (2008), the quench provided by explosive eruption justifies the use of pyroclastic rocks rather than plutonic rocks for oxide thermometry that yields temperatures prior to eruption. Based on the previously described principle that volcanic rocks are effectively quenched upon eruption it was originally assumed that cation exchange was effectively quenched by the explosion and eruption of the minerals analyzed in this study. This in turn justified the use of molar fractions of cations (Fe-Ti) in order to estimate the conditions in the magma chambers prior to eruption. Nonetheless, Cerro Galan and Cerro Blanco samples most likely were affected by post-eruptive processes that ultimately lead to alteration of these minerals. The evidence for the previously mentioned post-emplacement phenomena can be seen in figs. 3.11, 3.12, and 3.13.

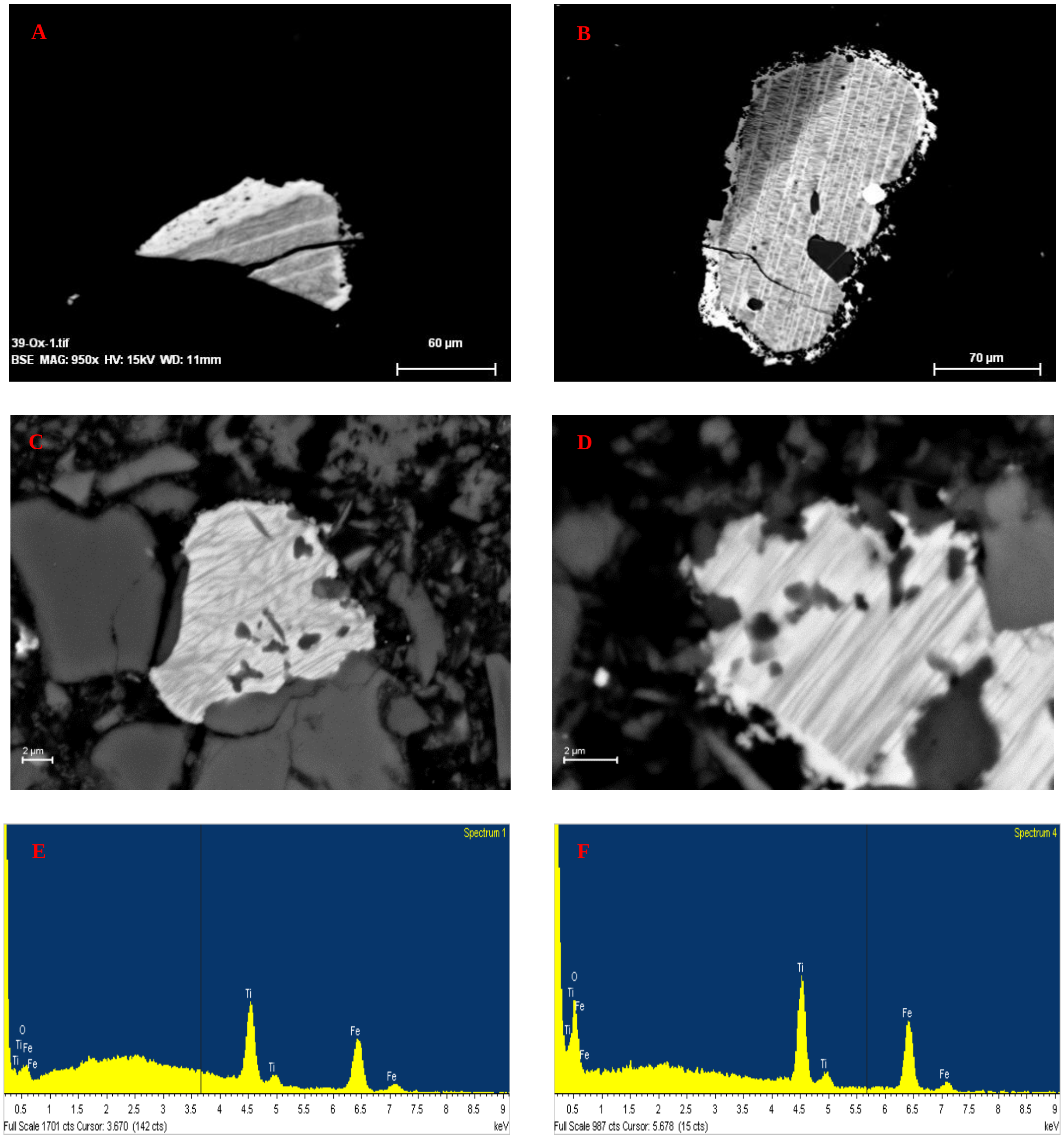

Fig.3.11. Panels A-D are scanning electron images of Fe-Ti oxides with pronounced oxidation in Section 1 of Cerro Galan. Panels E and F are X-Ray spectra of the brighter parts of the grains in panels A-C and B-D respectively. Panels A-C and B-D show very similar spectra therefore only 2 spectra are shown below. Panels A and B appear darker than C and D due to the brightness at which images were taken.

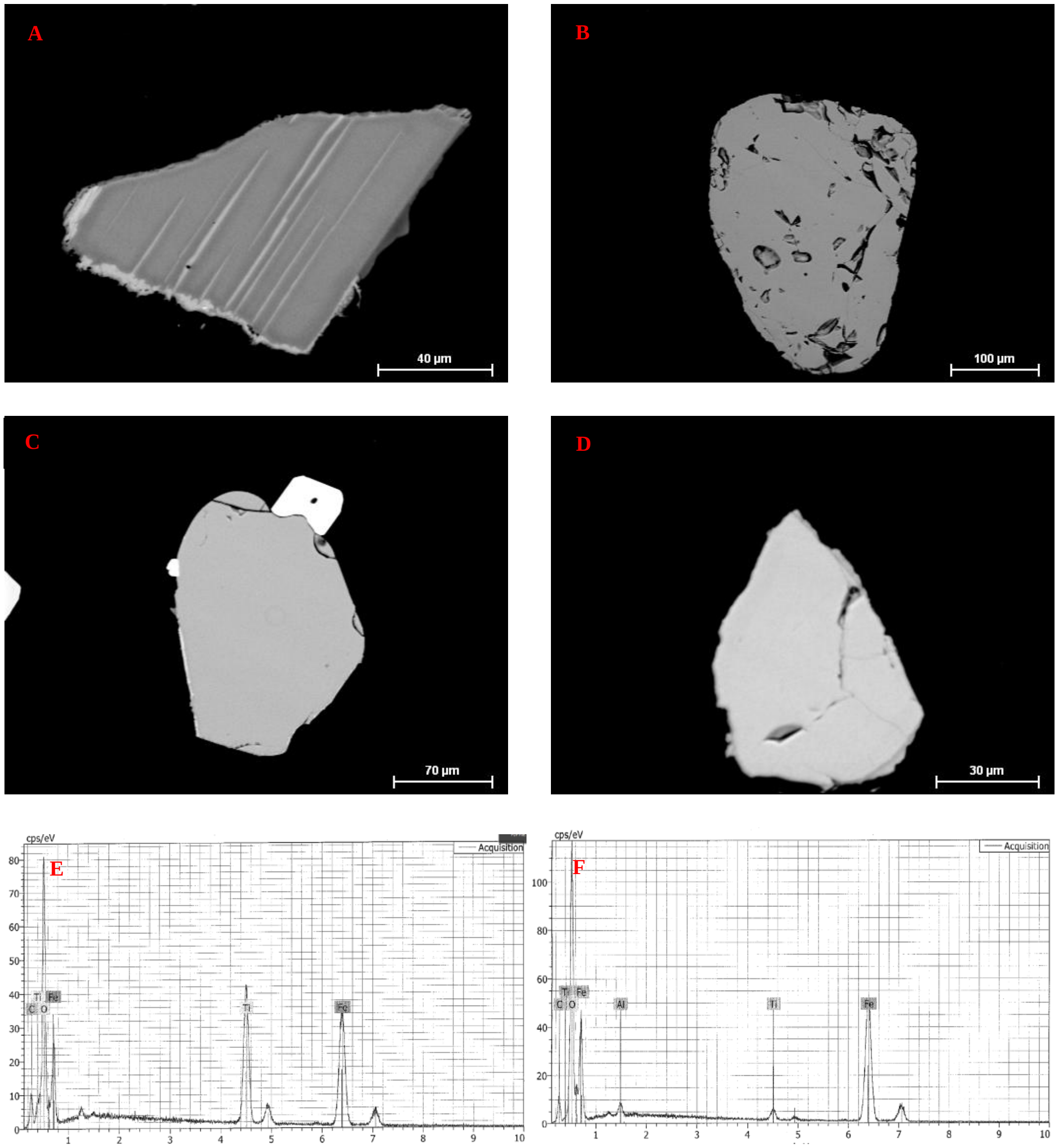

Fig.3.12. Panels A-D are scanning electron images of Fe-Ti oxides with oxidation in Section 2 of Cerro Galan. Panels E and F are X-Ray spectra taken from the 'smooth' parts of grains in panels A-C and B-D respectively (for panel A the non-exsolved parts). X-Ray spectra in panels A-B and B-D looked very similar, therefore only 2 spectra are shown below. Minerals in panels B and D are magnetites with no visible exsolution as depicted in panel F. Images were taken at different brightness and therefore panels C and D appear brighter than panels A and B.

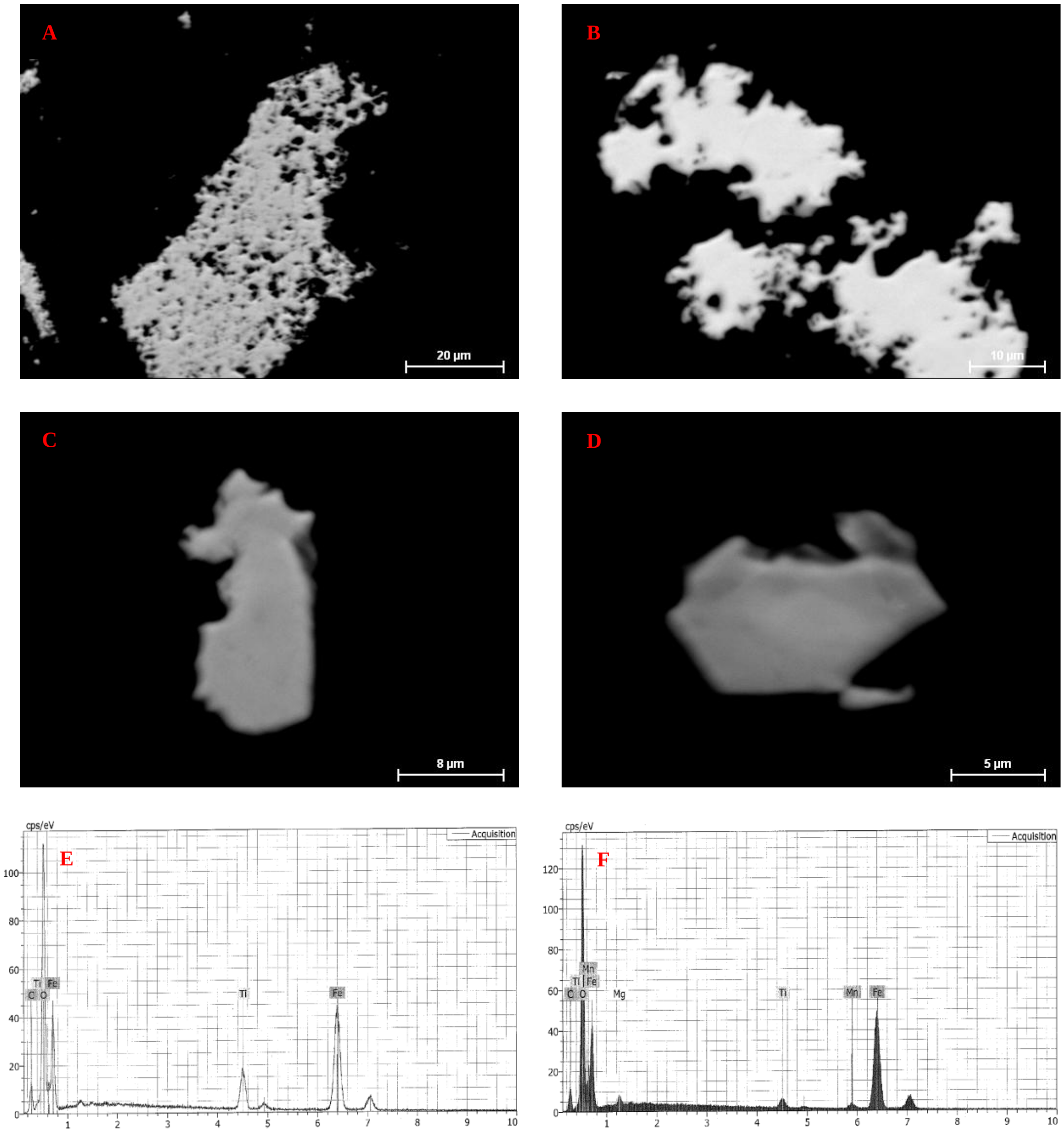

Fig.3.13. Panels A-D are scanning electron images of Fe-Ti oxides with oxidation in Cerro Blanco. Panels E and F are X-Ray spectra taken from the 'smooth' parts of grains in panels A-C and B-D respectively. X-Ray spectra in panels A-C and B-D looked very similar, therefore only 2 spectra are shown below. Minerals in panels B and D are magnetites with no visible exsolution as depicted in panel F. Images were taken at different brightness and therefore panels C and D appear brighter than panels A and B. No exsolution is visible in these grains.

Ilmenite ($FeTiO_3$) grains in this study most like were oxidized and altered to rutile (TiO_2), producing exsolution lamellae according to the reaction:

$$2FeTiO_3 + 1/2O_2 \rightleftharpoons Fe_2O_3 + 2TiO_2$$

Evidence of this can be seen in figure 3.11. Panels E and F are X-ray spectra obtained from analyzing the brighter parts (small sector of the brighter parts measuring 1µm in diameter, which defines the width of the electron beam) of the grains depicted in panels A-D. These areas are inferred to be the least altered parts of grains because they usually cover a greater surface area than the inferred exsolution lamellae, which are distinguishable by a darker color. X-ray spectra indicate that the brighter parts are likely ilmenite as observed from the near equal parts of Fe and Ti observed by the peaks in the spectra.

The darker color of the lamellae correlates to what is expected from a BSE image of a phase with a higher ratio of Ti to Fe than ilmenite, which is likely to be rutile. Rutile has a lower average atomic weight than ilmenite; therefore it should appear darker than the ilmenite because the higher the average atomic weight the brighter the mineral will appear on BSE images. The occurrence of this strong exsolution in the Fe-Ti minerals—referred to as alteration in this study—explains the wide ranging variations in the Fe-Ti oxides because cation concentrations represent alteration of grains to different degrees and they no longer represent equilibrium cation concentration of the minerals before the eruption.

Factors Contributing to Post-Emplacement Alteration of Fe-Ti Oxides

Some of the factors that may have contributed to the above-surface re-equilibration and alteration of the Fe-Ti oxides include the volume of the erupted magma, the presence of O_2 in the system at high temperatures, the style of eruption, plus circulation of fluids. The total volume of the erupted Cerro Galan Ignimbrite (CGI) is approximately 630 km^3 (Cas, et al. 2011). This volume is comparable to other large volcanic deposits such as the Valles caldera (approximately 600 km^3) of New Mexico, as reported by Goff and Shevenell (1987). Due to the large volume of magma being erupted it is likely that magma cooling was slow. Calculation of a diffusive cooling time for a 30 m ignimbrite (which is the minimum thickness of the CGI) to ambient temperature is about 28 years. This is further supported by Wright et al. (2011) who used thermal remanent magnetization of entrained lithic clasts in the CGI along with cooling rate models in order to estimate emplacement temperatures and cooling times of the CGI. These investigators claim that a 30 meter thick flow sheet would have taken at least 10 years to cool down by 200 ^{0}C. These calculations indicate that the deposits in the CGI would have been exposed to oxygen while being at temperatures above 400 ^{0}C—using Lesti et al.'s (2011) estimated emplacement temperature of 620 ^{0}C—for at least 10 years. This slow cooling would have been a favorable factor in allowing fluid circulation in the ash flow to last long enough to promote alteration of the Fe-Ti oxide minerals.

Moreover, as asserted by Cas et al. (2011) and Folkes et al. (2011), the absence of plinian fall deposits beneath the CGI , and development of welding in proximal to medial parts of the CGI indicate that the eruption column was never high, and that it collapsed almost immediately limiting the cooling of the pyroclasts in the column. The welding of the CGI also indicates high temperature emplacement of the deposits. This is further supported by Lesti (2011) who estimated the emplacement of the CGI at temperatures equal to or higher than 620°C based on thermal remanent magnetization of lithic clasts embedded within the CGI deposits.

No literature is available on emplacement temperatures or cooling times for Cerro Blanco, nonetheless, due to the presence of plinian deposits below the ash flow and a thinner ash flow, it is inferred that cooling time was less than that of Cerro Galan. Moreover, based on figs. 3.5, 3.6, 3.10, and SEM images in fig. 3.13 we can say that oxidation in the Cerro Blanco ignimbrite lasted long enough to disrupt equilibrium cation concentrations in the Fe-Ti oxides (as observed from a similar erratic trend in cation concentrations and ilmenite variability as in Cerro Galan plots).

Finally, from the above discussion it is clear that abnormally low temperatures obtained from Fe-Ti oxide thermometry can be attributed to alteration of ilmenites to different degrees after the eruption. Thermodynamic calculations as seen in tables 3.7—3.9 indicates that the closest temperatures to an estimated magmatic temperature of 700 ^{0}C (refer to feldspar section) are 624 & 580 ^{0}C at 1kb and 637 and 592 ^{0}C at 5kb (present only in two sets of Fe-Ti oxide grains). It is inferred that the grains that show the highest temperatures were not as oxidized as the rest of the grains. However, given the wide variability of sub-magmatic temperatures that arise from oxide calculations and given that most grains were within millimeters, it is likely that this happened by chance. This technique is unable to confirm nor refute the thermodynamic conditions inferred from feldspar thermometry.

CHAPTER 4

Halogens

Introduction

Water and the halogens have important roles in various planetary processes. Despite their low bulk abundance in our planet they influence magmatic composition and densities, mantle melting temperatures, the composition of oceans and atmospheres, and the occurrence of life (Patino Douce and Roden 2006). Understanding the volatile budgets in volcanic systems is of great importance because they may help us better understand how these species are affected by magma chamber conditions and the effects they have on the development of felsic magmas such as those of Cerro Galan and Cerro Blanco.

Compositions of volatile elements (found in apatite and biotite), Fe-Ti oxide pairs, and feldspars as a function of vertical location within a stratigraphic section allows us to use thermodynamic phase equilibria in order to make inferences about the presence or lack of magma chamber gradients (gradients in P, T, and fluid fugacities) prior to eruption. This in turn allows us to compare the pre-eruptive conditions of both magma chambers and to discern similarities and differences of these calderas (Cerro Galan and Cerro Blanco) prior to eruption. Thus, it is of interest to determine the pre-eruptive distribution of these volatiles in silicic to intermediate magma chambers.

Some of the minerals that are suitable for calculating volatile budgets are apatite, biotite, and hornblende. However, only apatite and biotite are found in the above-mentioned volcanic calderas, therefore only these two minerals were used in this study. Apatite and biotite are suitable for calculating volatile budgets in this investigation because these minerals incorporate F, Cl, and OH in their structures and are found in both systems. One of the main goals of this investigation was the use of coexisting apatite and biotite phases at equilibrium in order to investigate the variation of the fluid species as a function of vertical location.

Water and the halogens F and Cl can be expected to fractionate in large magma chambers, by virtue of their different molecular weights and melt vs. mineral vs. fluid affinities. In general, Cl and OH partition into hydrous fluid whereas F partitions into the melt (Carroll and Webster 1994; Patino Douce and Roden 2006). This study attempted to elucidate the degree to which fractionation of halogens took place in both Cerro Galan and Cerro Blanco volcanic calderas. Preliminary expectations are that the halogens fractionated as the magma evolved in a predictable pattern. According to Mathez and Webster (2004), the content of F in melt and apatite co-vary linearly, and F is weakly dependant on melt composition. Similarly, the distribution of Cl an OH between apatite and melt follows a linear path (Cl and OH concentrations in apatite increases as their availability in the melt increases). In the case of Cl this linear variation is observed at concentrations less than or equal to 3.8% in the melt (as determined by experiment) and depends weakly on OH concentration (Mathez and Webster 2004).

Based on the behavior of the volatiles described above, if the halogens followed an 'ideal' fractionation behavior, one could expect to see an increase in F in apatite from the bottom to the top of the magma chamber. Conversely, a decrease in Cl from the bottom to the top of the sampled stratigraphic sections is expected (or in the very least a non-monotonous trend). This would be the case if we assume a simple scenario in which the bottoms of the sampled sections represent the first deposits that came out of the eruption, representing the highest levels of magma in the sub-volcanic chambers. This is based on the notion that F would be preferentially incorporated into apatite in the early stages of crystallization—ideally correlating to deeper levels of the magma chamber—and become depleted as the magma evolves (crystallizing more apatite grains) at which point apatite would ideally incorporate more chlorine and hydroxyl into its structure. The preferential incorporation of F into apatite is reflected by the high abundance of fluorapatite relative to chlorapatite and hydroxyapatite in natural systems (Piccoli and Candela 2002).

Moreover, it is expected that if both magmatic systems were at equilibrium and processes such as degassing or magma recharge occurred, apatite and biotite volatile concentrations would reflect this. In the case of degassing, apatite and biotite grains would record a decrease in Cl and OH concentrations relative to F (Cl and OH preferentially stay in the fluid phase). This is supported by Villemant and Boudon (1999), who indicate that H_2O and Cl behave similarly during magma degassing (both of them being depleted in the magma chamber during degassing), while F is not involved in any processes related to magma degassing. In contrast, magma recharge would show the opposite trend with an increase in Cl and OH relative to F. The previously described trend would be dependent on the composition of the recharging magma (recharging magma should contain Cl, F, and OH). Therefore, magma degassing processes (if they occurred) may be expected to present a more discernible signature than magma recharging processes.

Analytical Procedures

Electron Microprobe analyses

Tables 4.1—4.6 show apatite and biotite compositions and mole concentrations for the volatile elements for sections 1 & 2 of Cerro Galan and Cerro Blanco. The analytical methods described in Sarafian (2012) and Schrader (2009) were followed in the analysis of apatites and biotites. Typical electron microprobe operating conditions were a 15kV accelerating voltage and a 5nA beam current. Grain size permitting, a 5µm defocused electron beam was used. For apatites that were smaller than 5µm a focused electron beam (~1µm) or a beam raster (~1-3µm) was used (biotites were always much larger than 5µm so the electron beam used in these minerals was always 5µm in diameter). To ensure accurate analyses the halogens were measured first to minimize halogen migration as described in Sarafian (2012).

Apatite Formulae Calculations

Oxide concentrations for apatite were recalculated to 25 charges and 8 cations based on the structural formula of apatite $Ca_5(PO_4)_3(F, Cl, OH)$ solid solution (figs 4.1—4.3). Apatite analyses used for estimation of halogen and water budgets along with thermodynamic calculations were selected on the basis of three main parameters: oxide total obtained from microprobe close to 100 % (+/- 1), cation total close to 8 (+/- 0.1), and positive OH concentrations (Sarafian, 2012). Hydroxide mole fractions were estimated by difference, assuming that $X_F + X_{Cl} + X_{OH} = 1$, in accordance with the three end-members fluorapatite (FAp), chlorapatite (ClAp), and hydroxyapatite (OHAp) of the apatite solid solution.

Table 4.1. Section 1 Cerro Galan apatite compositions obtained by microprobe analyses. O = F + Cl is the oxygen weight% equivalent of the F + Cl compositions assumed to be present during microprobe analyses, this value was subtracted from the total, yielding the total-eq (equivalent).

	Sample							
Wt%	A07 45-1	A07 43-4	A07 42-7	A07 41-4	A07 40-2	A07 39-2	A07 38-C	A07 37-A
SiO2	0.14	0.17	0.25	0.14	0.03	0.18	0.27	0.41
FeO	0.00	0.00	4.10	0.00	5.80	0.49	0.33	0.55
MgO	0.00	0.00	0.00	0.00	0.13	0.00	0.00	0.14
CaO	53.71	53.45	51.49	55.20	51.94	53.14	54.48	53.27
SrO	0.00	0.00	0.00	0.00	0.00	0.00	0.05	0.04
Ce2O3	0.00	0.00	0.00	0.00	0.00	0.00	0.37	0.41
Y2O3	0.00	0.00	0.00	0.00	0.00	0.00	0.05	0.10
Na2O	0.00	0.00	0.00	0.16	0.00	0.20	0.06	0.16
P2O5	41.05	41.62	38.80	41.57	40.54	40.55	41.34	41.63
SO3	0.00	0.00	0.00	0.00	0.00	0.00	0.14	0.27
F	2.66	3.25	3.12	2.76	3.20	3.29	2.78	3.08
Cl	0.43	0.65	0.54	0.31	0.50	0.50	0.52	0.74
Total	97.98	99.14	98.30	100.15	102.13	98.35	100.41	100.81
O=F+Cl	1.21	1.51	1.43	1.23	1.46	1.50	1.29	1.46
Total-eq	96.76	97.62	96.86	98.92	100.67	96.85	99.12	99.35
Ions recalculated to 12 oxygen atoms + 1 volatile anion (F+Cl+OH)								
Si	0.01	0.01	0.02	0.01	0.00	0.02	0.02	0.03
Fe	0.00	0.00	0.30	0.00	0.41	0.04	0.02	0.04
Mg	0.00	0.00	0.00	0.00	0.02	0.00	0.00	0.02
Ca	4.97	4.91	4.88	5.01	4.75	4.95	4.95	4.83
Sr	0.00	0.00	0.00	0.00	0.00	0.00	0.00	0.00
Ce	0.00	0.00	0.00	0.00	0.00	0.00	0.01	0.01
Y	0.00	0.00	0.00	0.00	0.00	0.00	0.00	0.00
Na	0.00	0.00	0.00	0.03	0.00	0.03	0.01	0.03
P	3.00	3.02	2.91	2.98	2.93	2.99	2.97	2.98
S	0.00	0.00	0.00	0.00	0.00	0.00	0.01	0.02
Cation total	7.98	7.95	8.12	8.03	8.11	8.02	7.99	7.95
F	0.73	0.88	0.87	0.74	0.86	0.90	0.75	0.82
Cl	0.06	0.09	0.08	0.04	0.07	0.07	0.07	0.11
Halogens	0.79	0.98	0.95	0.78	0.93	0.98	0.82	0.93
OH Difference	0.21	0.02	0.05	0.22	0.07	0.02	0.18	0.07
Wt% OH	0.37	0.04	0.08	0.38	0.11	0.04	0.32	0.12

Table 4.2. Section 2 Cerro Galan apatite compositions obtained by microprobe analyses. O = F + Cl is the oxygen weight% equivalent of the F + Cl compositions assumed to be present during microprobe analyses, this value was subtracted from the total, yielding the total-eq (equivalent).

	Sample						
Wt%	A07 07-1	A07 06-1	A07 05-2	A07 04-5	A07 03-4	A07 02-3	A07 01-4
SiO2	0.256	0.372	0.235	0.197	1.825	0.279	0.276
FeO	0.199	0.251	0.057	0.086	0.148	0.175	0.140
MgO	0.000	0.000	0.000	0.000	0.000	0.000	0.000
CaO	54.830	54.490	53.910	53.640	54.010	54.110	54.310
SrO	0.073	0.000	0.070	0.063	0.027	0.050	0.084
Ce2O3	0.403	0.315	0.809	0.135	0.000	0.626	0.134
Y2O3	0.223	0.035	0.190	0.206	0.000	0.137	0.171
Na2O	0.111	0.086	0.126	0.164	0.404	0.106	0.079
P2O5	39.910	41.440	39.970	40.650	34.000	41.440	41.640
SO3	0.096	0.029	0.104	0.261	0.128	0.158	0.101
F	2.845	3.210	2.780	2.525	3.170	3.080	2.689
Cl	0.442	0.490	0.511	0.436	0.328	0.371	0.507
Total	99.389	100.717	98.762	98.363	94.039	100.532	100.131
O=F+Cl	1.298	1.462	1.286	1.161	1.409	1.381	1.246
Total-eq	98.091	99.254	97.476	97.201	92.630	99.151	98.885
Ions recalculated to 12 oxygen atoms + 1 volatile anion (F+Cl+OH)							
Si	0.022	0.032	0.020	0.017	0.170	0.024	0.023
Fe	0.014	0.018	0.004	0.006	0.011	0.012	0.010
Mg	0.000	0.000	0.000	0.000	0.000	0.000	0.000
Ca	5.076	4.951	5.018	4.955	5.386	4.919	4.929
Sr	0.004	0.000	0.004	0.003	0.001	0.002	0.004
Ce	0.013	0.010	0.026	0.004	0.000	0.019	0.004
Y	0.010	0.002	0.009	0.009	0.000	0.006	0.008
Na	0.019	0.014	0.021	0.027	0.073	0.017	0.013
P	2.920	2.975	2.940	2.967	2.679	2.977	2.986
S	0.006	0.002	0.007	0.017	0.009	0.010	0.006
Cation total	8.078	8.001	8.042	7.989	8.321	7.977	7.978
F	0.777	0.861	0.764	0.688	0.933	0.826	0.720
Cl	0.065	0.070	0.075	0.064	0.052	0.053	0.073
Halogens	0.842	0.931	0.839	0.752	0.985	0.880	0.793
OH Difference	0.158	0.069	0.161	0.248	0.015	0.120	0.207
Wt% OH	0.274	0.121	0.278	0.431	0.024	0.212	0.366

Table 4.3. Cerro Blanco apatite compositions obtained by microprobe analyses. O = F + Cl is the oxygen weight% equivalent of the F + Cl compositions assumed to be present during microprobe analyses, this value was subtracted from the total, yielding the total-eq (equivalent).

	Sample					
Wt%	A07 68-2	A07 67-2	A07 66-2	A07 65-2	A07 64-2	A07 63-2
SiO2	0.877	0.242	1.625	1.673	0.515	0.211
FeO	0.699	0.286	0.434	0.585	0.206	0.559
MgO	0.000	0.000	0.000	0.000	0.000	0.000
CaO	53.170	54.580	52.150	52.290	52.230	52.630
SrO	0.015	0.032	0.126	0.083	0.061	0.059
Ce2O3	1.157	0.215	1.328	0.818	0.722	0.337
Y2O3	0.173	0.156	0.157	0.155	0.103	0.000
Na2O	0.313	0.363	0.175	0.391	0.169	0.436
P2O5	41.450	41.070	37.370	41.030	42.170	41.100
SO3	0.607	0.888	0.810	0.296	0.223	0.606
F	1.690	3.230	2.032	2.082	2.166	2.676
Cl	1.096	0.336	1.169	0.999	0.805	1.032
Total	101.247	101.398	97.375	100.401	99.370	99.647
O=F+Cl	0.959	1.436	1.119	1.102	1.094	1.360
Total-eq	100.288	99.963	96.256	99.299	98.276	98.287
Ions recalculated to 12 oxygen atoms + 1 volatile anion (F+Cl+OH)						
Si	0.073	0.020	0.144	0.141	0.044	0.018
Fe	0.049	0.020	0.032	0.041	0.015	0.040
Mg	0.000	0.000	0.000	0.000	0.000	0.000
Ca	4.763	4.914	4.936	4.720	4.739	4.819
Sr	0.001	0.002	0.006	0.004	0.003	0.003
Ce	0.035	0.007	0.043	0.025	0.022	0.011
Y	0.008	0.007	0.007	0.007	0.005	0.000
Na	0.051	0.059	0.030	0.064	0.028	0.072
P	2.934	2.922	2.795	2.927	3.024	2.974
S	0.038	0.056	0.054	0.019	0.014	0.039
Cation total	7.915	7.951	7.993	7.929	7.879	7.936
F	0.447	0.858	0.568	0.555	0.580	0.723
Cl	0.155	0.048	0.175	0.143	0.116	0.150
Halogens	0.602	0.906	0.743	0.697	0.696	0.873
OH Difference	0.398	0.094	0.257	0.303	0.304	0.127
Wt% OH	0.712	0.167	0.436	0.538	0.538	0.223

Biotite Formulae Calculations

Tables 4.4—4.6 show compositions of selected biotite analyses along with mole fractions calculated after Schrader (2009) based on 12 anions (22 charges): OH was calculated by difference as 2-(F+Cl), X_F = F/(F+Cl+OH), X_{Cl} = Cl/(F+Cl+OH), and X_{OH} = OH/(F+Cl+OH). All iron in the structure was assumed to be ferrous iron (Fe^{2+}). Biotite analyses used for estimation of halogen and water budgets along with thermodynamic calculations were selected mainly on oxide total. When possible analyses selected presented a weight % total above 95.

Table 4.4. Section 1 Cerro Galan biotite compositions obtained by microprobe analyses

	Sample							
Wt %	A07 45B2	A07 43B3	A07 42B1	A07 41B1	A07 40B3	A07 39B1	A07 38B1	A07 37B1
SiO2	35.98	36.97	36.67	36.32	36.42	36.87	36.38	36.14
TiO2	3.80	4.01	4.00	4.19	4.21	4.23	4.22	4.16
Al2O3	14.81	14.10	14.15	13.97	14.05	14.31	14.08	14.26
MgO	11.00	12.28	13.15	12.57	12.46	12.80	12.85	12.69
FeO	20.76	19.82	17.85	18.88	18.66	18.28	18.07	18.23
CaO	0.06	0.00	0.00	0.05	0.03	0.05	0.05	0.00
MnO	0.21	0.21	0.33	0.16	0.21	0.20	0.26	0.29
K20	9.13	8.91	8.69	9.11	9.09	8.78	8.88	9.14
Na2O	0.18	0.26	0.36	0.32	0.35	0.32	0.30	0.34
F	1.34	1.07	1.09	1.18	1.00	1.43	1.32	1.10
Cr	0.03	0.00	0.00	0.00	0.00	0.00	0.00	0.00
Ba	0.00	0.00	0.00	0.00	0.00	0.00	0.00	0.00
Cl	0.11	0.21	0.16	0.15	0.14	0.20	0.21	0.18
Total	97.54	97.83	96.45	97.13	96.82	97.97	96.61	96.72
Atoms recalculated								
Sites (T) 4 & 6								
Si	2.75	2.79	2.78	2.76	2.77	2.78	2.77	2.75
Al4	1.25	1.21	1.22	1.24	1.23	1.22	1.23	1.25
Al6	0.08	0.04	0.05	0.02	0.03	0.05	0.03	0.03
Ti	0.22	0.23	0.23	0.24	0.24	0.24	0.24	0.24
Mg	1.25	1.38	1.49	1.43	1.41	1.44	1.46	1.44
Fe	1.33	1.25	1.13	1.20	1.19	1.15	1.15	1.16
Mn	0.01	0.01	0.02	0.01	0.01	0.01	0.02	0.02
Cations sites 4 &6	6.90	6.91	6.91	6.89	6.88	6.88	6.90	6.89
Vacancies sites 4 &6	0.10	0.09	0.09	0.11	0.12	0.12	0.10	0.11

Site (T) 12								
K	0.890	0.857	0.841	0.884	0.882	0.843	0.862	0.888
Na	0.026	0.039	0.052	0.047	0.051	0.046	0.044	0.050
Ba	0.000	0.000	0.000	0.000	0.000	0.000	0.000	0.000
Cations site 12	0.916	0.895	0.893	0.931	0.933	0.889	0.906	0.938
F	0.323	0.254	0.262	0.283	0.240	0.341	0.318	0.266
Cl	0.015	0.026	0.021	0.019	0.018	0.025	0.027	0.024
OH (diff)	1.662	1.719	1.717	1.698	1.742	1.633	1.655	1.711
Volatile mole fractions recalculated to one anion								
X_F	0.162	0.127	0.131	0.141	0.120	0.171	0.159	0.133
X_{Cl}	0.007	0.013	0.010	0.009	0.009	0.013	0.013	0.012
X_{OH}	0.831	0.860	0.858	0.849	0.871	0.817	0.827	0.855

Table 4.5. Section 2 Cerro Galan biotite compositions obtained by microprobe analyses

	Sample						
Wt %	A07 02B3	A07 03B2	A07 04B4	A07 05B2	A07 06B3	A07 07B2	A07 01B3
SiO2	35.66	36.37	36.00	35.99	35.28	36.43	36.03
TiO2	4.17	3.93	4.04	4.04	3.76	4.10	4.39
Al2O3	14.30	14.07	14.51	13.92	14.34	14.23	15.08
MgO	12.09	13.28	13.32	12.47	12.71	12.69	13.93
FeO	18.91	18.38	18.01	18.29	17.12	18.50	17.85
CaO	0.02	0.03	0.04	0.02	0.07	0.08	0.02
MnO	0.26	0.32	0.17	0.33	0.18	0.23	0.36
K20	9.39	9.35	8.87	9.16	8.82	9.21	9.24
Na2O	0.30	0.36	0.34	0.37	0.37	0.39	0.30
F	0.39	0.40	0.59	0.49	0.55	1.01	0.57
Cr	0.00	0.00	0.00	0.00	0.00	0.00	0.00
Ba	0.10	0.12	0.47	0.29	0.19	0.00	0.07
Cl	0.15	0.18	0.15	0.17	0.14	0.18	0.17
Total	95.75	96.79	96.50	95.53	93.54	97.04	98.01
Atoms recalculated							
Sites (T) 4 & 6							
Si	2.74	2.75	2.73	2.77	2.75	2.76	2.69
Al4	1.26	1.25	1.27	1.23	1.25	1.24	1.31
Al6	0.03	0.01	0.03	0.03	0.07	0.03	0.01
Ti	0.24	0.22	0.23	0.23	0.22	0.23	0.25
Mg	1.38	1.50	1.51	1.43	1.48	1.43	1.55
Fe	1.21	1.16	1.14	1.18	1.12	1.17	1.11
Mn	0.02	0.02	0.01	0.02	0.01	0.01	0.02

Cations sites 4 &6	6.89	6.91	6.92	6.88	6.89	6.91	6.94
Vacancies sites 4 &6	0.11	0.09	0.08	0.12	0.11	0.09	0.06
Site (T) 12							
K	0.920	0.903	0.858	0.898	0.877	0.891	0.879
Na	0.045	0.053	0.050	0.054	0.056	0.057	0.043
Ba	0.003	0.004	0.016	0.010	0.007	0.000	0.002
Cations site 12	0.968	0.960	0.924	0.962	0.939	0.948	0.924
F	0.096	0.095	0.140	0.118	0.136	0.241	0.134
Cl	0.020	0.023	0.020	0.022	0.019	0.024	0.021
OH (diff)	1.885	1.882	1.840	1.860	1.845	1.735	1.845
Volatile mole fractions recalculated to one anion							
X_F	0.048	0.047	0.070	0.059	0.068	0.120	0.067
X_{Cl}	0.010	0.011	0.010	0.011	0.009	0.012	0.011
X_{OH}	0.942	0.941	0.920	0.930	0.923	0.868	0.922

Table 4.6. Cerro Blanco biotite compositions obtained by microprobe analyses

	Sample					
Wt %	A07 68B4	A07 67B5	A07 66B2	A07 63B2	A07 64B2	A07 65B4
SiO2	38.31	37.55	36.57	37.41	37.66	36.17
TiO2	4.96	4.84	5.01	4.77	5.02	5.04
Al2O3	14.21	14.30	15.35	14.35	14.06	14.37
MgO	13.74	13.43	13.49	14.13	14.35	13.28
FeO	17.12	17.34	17.30	17.09	16.75	17.23
CaO	0.00	0.06	0.00	0.00	0.00	0.00
MnO	0.32	0.18	0.25	0.25	0.33	0.38
K20	8.54	8.27	8.36	8.65	8.92	8.93
Na2O	0.49	0.51	0.47	0.49	0.39	0.47
F	0.20	0.44	0.29	0.00	0.00	0.00
Cr	0.00	0.00	0.00	0.00	0.00	0.00
Ba	0.58	0.29	0.75	0.51	0.00	0.61
Cl	0.16	0.13	0.16	0.12	0.09	0.12
Total	98.64	97.34	98.01	97.77	97.57	96.61
Atoms recalculated						
Sites (T) 4 & 6						
Si	2.80	2.79	2.70	2.76	2.77	2.72
Al4	1.20	1.21	1.30	1.24	1.23	1.28
Al6	0.03	0.04	0.04	0.01	0.00	0.00
Ti	0.27	0.27	0.28	0.26	0.28	0.29
Mg	1.50	1.49	1.49	1.55	1.57	1.49

Fe	1.05	1.08	1.07	1.05	1.03	1.08
Mn	0.02	0.01	0.02	0.02	0.02	0.02
Cations sites 4 &6	6.86	6.88	6.89	6.89	6.91	6.89
Vacancies sites 4 &6	0.14	0.12	0.11	0.11	0.09	0.11
Site (T) 12						
K	0.796	0.782	0.789	0.814	0.837	0.857
Na	0.070	0.074	0.068	0.070	0.056	0.068
Ba	0.018	0.009	0.024	0.016	0.000	0.020
Cations (site 12)	0.885	0.866	0.881	0.900	0.894	0.945
F	0.047	0.104	0.068	0.000	0.000	0.000
Cl	0.020	0.016	0.020	0.015	0.011	0.015
OH (diff)	1.933	1.881	1.913	1.985	1.989	1.985
Volatile mole fractions recalculated to one anion						
X_F	0.024	0.052	0.034	0.000	0.000	0.000
X_{Cl}	0.010	0.008	0.010	0.008	0.006	0.008
X_{OH}	0.966	0.940	0.956	0.992	0.994	0.992

Apatite Composition Plots

Apatite plots for F, Cl, and OH molar concentrations were made against stratigraphic position. Error for halogen analyses was calculated based on the analytical error calculated from standard apatite minerals. The analytical error for F and Cl was added and subtracted from the concentration of each analysis in order to define the high and low values of the analysis. These high and low values define the high and low error bars in concentrations depicted below. The analytical precision for OH was calculated using standard error propagation according to the following (Sarafian, 2012),

$$[(F_{error})^2 * (Cl_{error})^2]^{1/2}$$

F_{error} and Cl_{error} are the values of the analytical errors of fluorine and chlorine respectively

Plots for each of the sections (sections 1and 2 of Cerro Galan and Cerro Blanco) were made separately utilizing molar concentration found in tables 4.1—4.3. In order to aid visualization plots for each of the volatiles were color coded and graphs for each section were split.

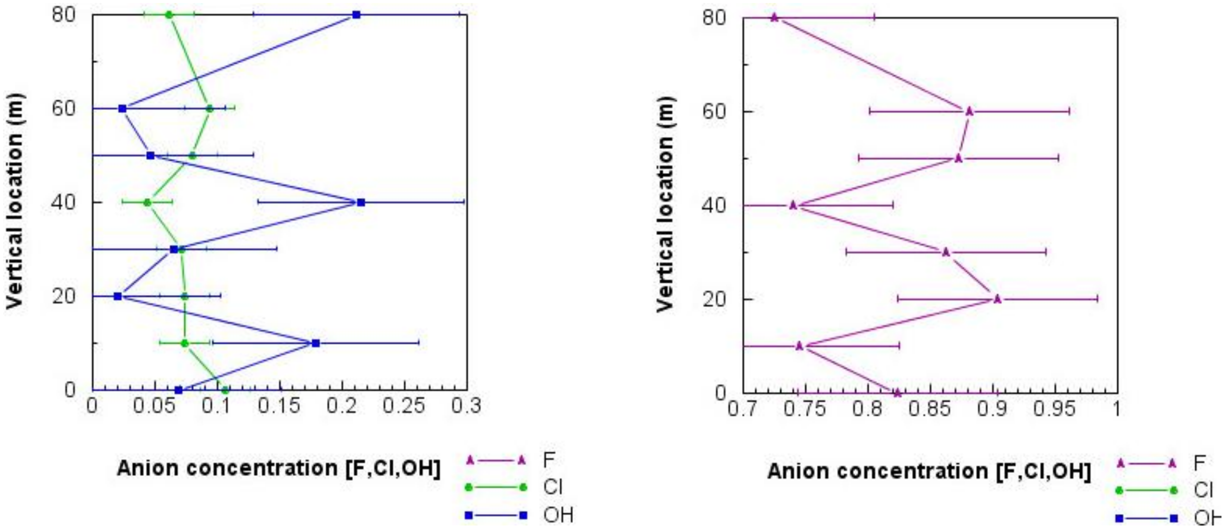

Fig.4.1. Section 1 Cerro Galan apatite anion concentration vs. vertical location

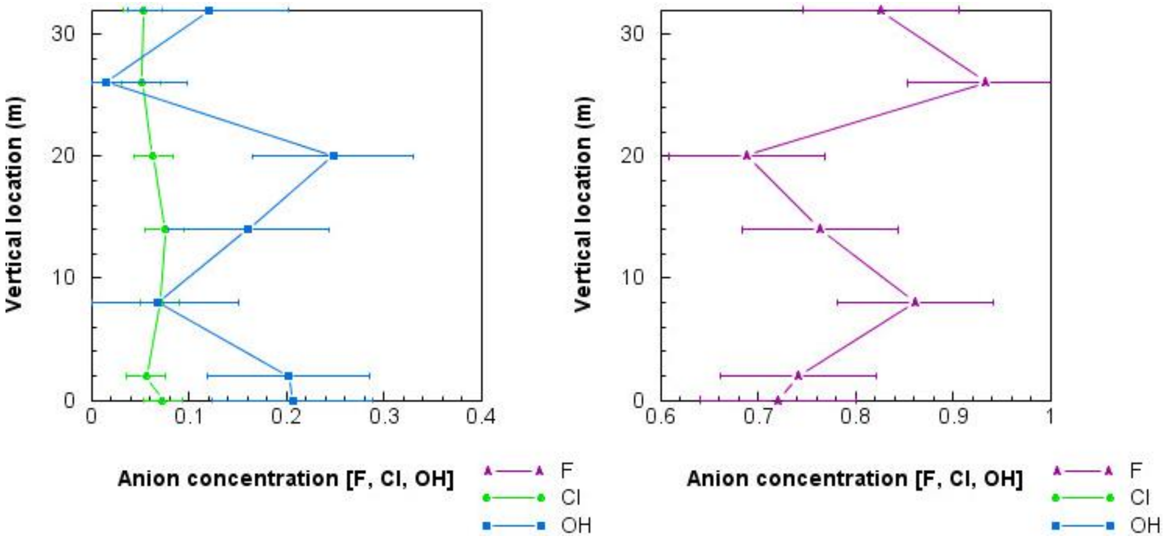

Fig.4.2. Section 2 Cerro Galan apatite anion concentration vs. vertical location

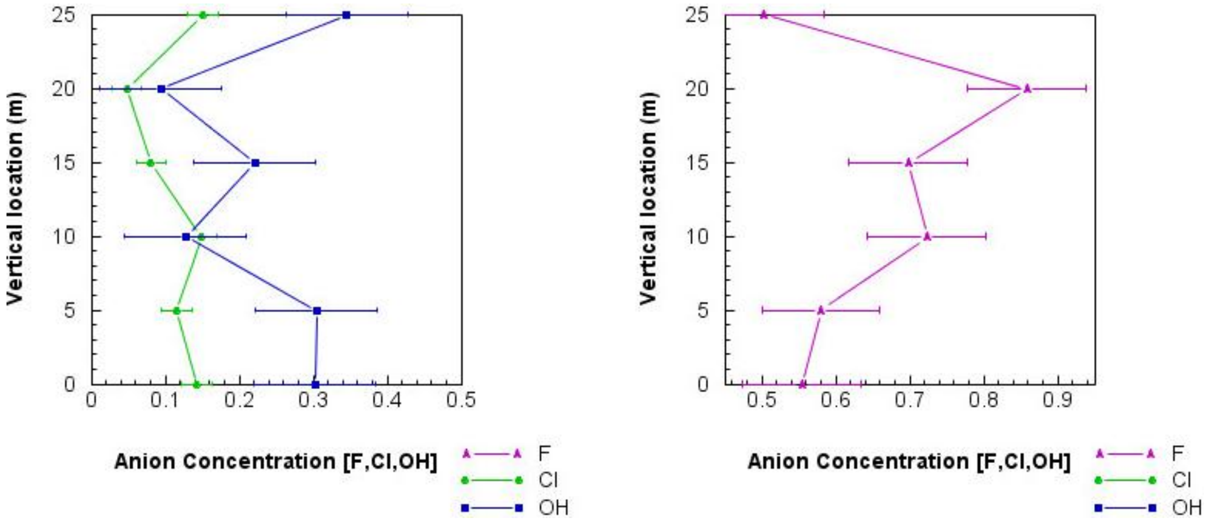

Fig.4.3. Cerro Blanco apatite anion concentration vs. vertical location

Biotite Composition Plots

Biotite plots of F, Cl, and OH molar fractions were made against stratigraphic position. Biotite molar fraction concentrations were divided by 2 in order to compare with apatite molar fraction concentrations (there are 2 anion sites in biotite compared to 1 in apatite). Errors for the halogens in biotite were calculated based on the same procedure used for the apatites described above. Plots for each of the sections (sections 1and 2 of Cerro Galan and Cerro Blanco) were made separately utilizing molar concentration found in tables 4.4—4.6. In order to aid visualization plots for each of the volatiles were color coded and graphs for each section were split.

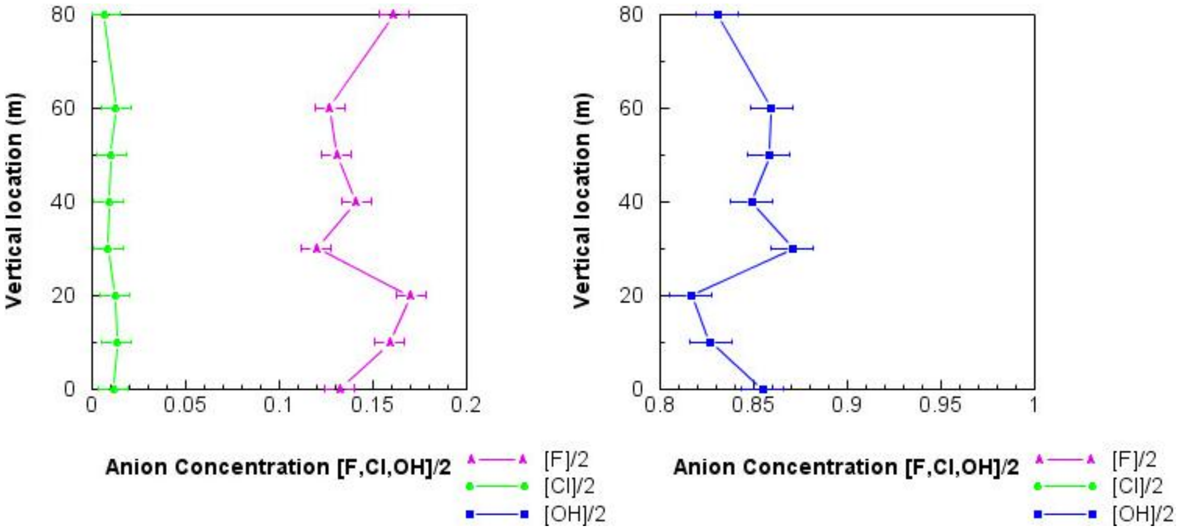

Fig.4.4. Section 1 Cerro Galan biotite anion concentration vs. vertical location

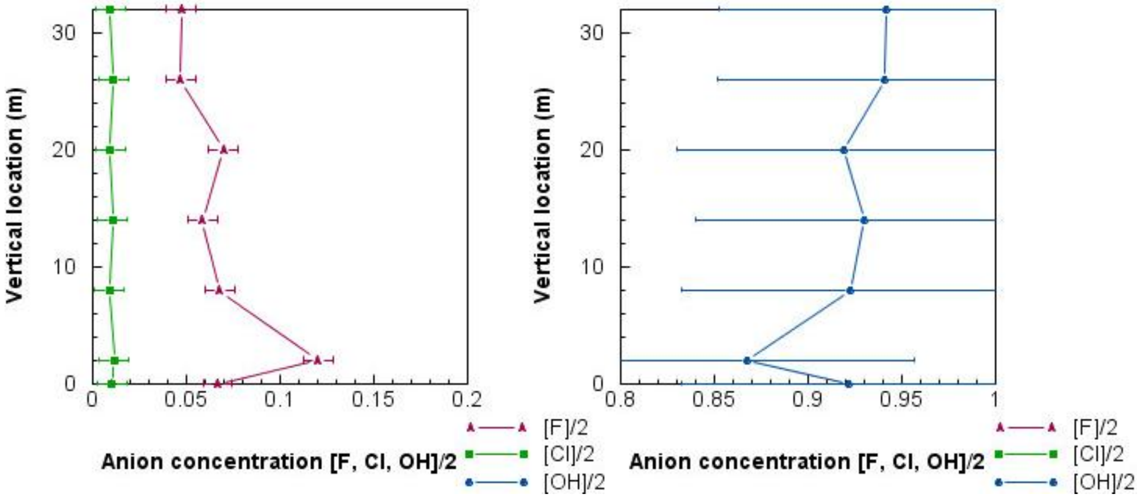

Fig.4.5. Section 2 Cerro Galan biotite anion concentration vs. vertical location

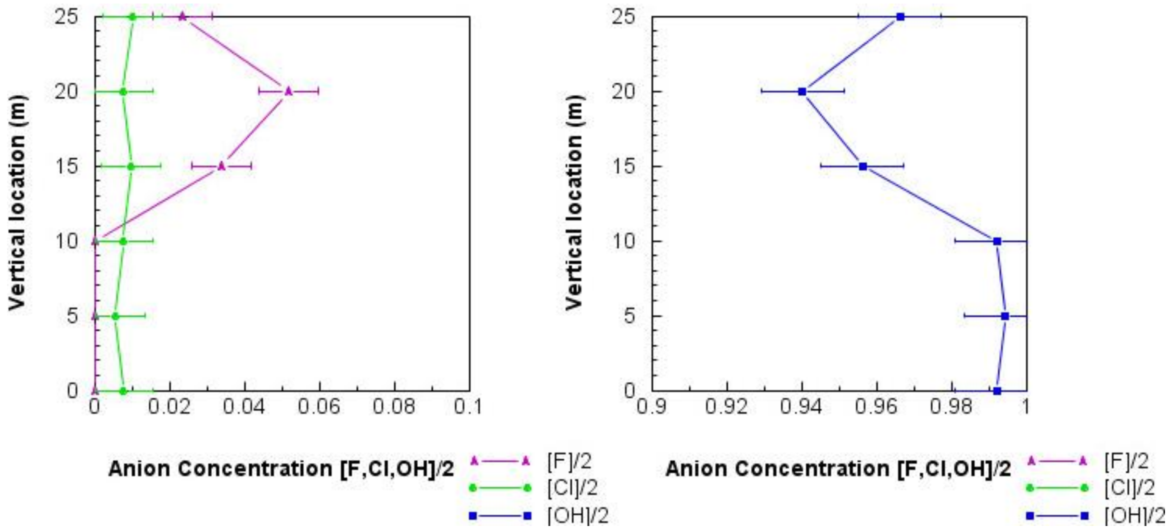

Fig.4.6. Cerro Blanco biotite anion concentration vs. vertical location

Thermodynamic Framework

In order to determine whether the apatite and biotite compositions analyzed in this study represent equilibrium compositions—meaning they were not affected by post-emplacement alteration—the values of lnK (the logarithm of the equilibrium constant K) were calculated utilizing the same volatile concentrations that were used for making plots with respect to vertical location according to the following equilibrium phase assemblages:

(1) $2\ Ca_5(PO_4)_3Cl + KMg_3AlSi_3O_{10}(F)_2 \rightleftharpoons 2\ Ca_5(PO_4)_3F + KMg_3AlSi_3O_{10}(Cl)_2$

Chlorapatite F-phlogopite Fluorapatite Cl-phlogopite

(2) $2\ Ca_5(PO_4)_3OH + KMg_3AlSi_3O_{10}(F)_2 \rightleftharpoons 2\ Ca_5(PO_4)_3F + KMg_3AlSi_3O_{10}(OH)_2$

Hydroxyapatite F-phlogopite Fluorapatite OH-phlogopite

(3) $2\ Ca_5(PO_4)_3OH + KMg_3AlSi_3O_{10}(Cl)_2 \rightleftharpoons 2\ Ca_5(PO_4)_3Cl + KMg_3AlSi_3O_{10}(OH)_2$

Hydroxyapatite Cl-phlogopite Chlorapatite OH-phlogopite

If we assume the system was at equilibrium (given we only have solid phases), then

(4) $\Delta G = \Delta G^0_{1,T} + (P-1)^* \Delta V_{solids} + RT\ln K = 0$

Where G = Gibbs free energy change for reactions (1-3); $G^0_{1,T}$ = standard state Gibbs free energy at 1bar and temperature T; P = pressure(where the -1 in the equation is the result of integration of pressure from 1 bar—standard state—to the pressure of interest); R = ideal gas constant; T = temperature; and K = equilibrium constant;

In addition, from eqns. 1-3 we can define K in terms of molar concentration as follows,

$K1 = [(X_{Cl})^2_{ClPh} * (X_F)^2_{FAp}]/[(X_F)^2_{FPh} * (X_{Cl})^2_{ClAp}]$

$K2 = [(X_{OH})^2_{OHPh} * (X_F)^2_{FAp}]/[(X_F)^2_{FPh} * (X_{OH})^2_{OHAp}]$

$K3 = [(X_{OH})^2_{OHPh} * (X_{Cl})^2_{ClAp}]/[(X_{Cl})^2_{ClPh} * (X_{OH})^2_{OHAp}]$

The key assumption for the preceding definitions is that the system was at equilibrium. If this was the case, then K values would remain constant within error for the 3 analyzed sections assuming temperature and pressure variations across the magma chamber can be neglected. If temperature and pressure variations cannot be neglected and the ash flow deposits represent the inverted stratigraphy of the magma chamber, then at the very least it is expected that K values would vary monotonically with vertical location rather than in a random pattern.

Moreover, if the Cerro Galan and Cerro Blanco systems were at equilibrium and processes such as degassing or magma recharge occurred, apatite and biotite volatile concentrations would adjust accordingly as described above, however, K values would remain constant (assuming pressure and temperature variations across the magma chamber can be ignored as described above). In other words, as defined above in K1-K3, the ratio of the product-to-reactant concentrations of the volatiles in eqns.1-3 remains constant if the systems is at equilibrium. Therefore, changes in the absolute concentration in the volatiles may be recorded in the apatites and biotites but the value of K would be the same.

Moreover, as pointed out by Mathez and Webster (2004) and Boyce and Hervig (2009) apatite rapidly equilibrates with its surroundings with respect to the halogens; therefore K values for the above described equilibrium reactions can be expected to be particularly good equilibrium indicators in the case that both minerals were at equilibrium and not altered by post-emplacement processes. Nonetheless, if these minerals were subjected to alteration, apatite is not as vulnerable as the micas to subsolidus Cl-OH exchange (Piccoli and Candela 1994), therefore, it is expected that apatites present less alteration of the original volatile concentrations than biotite.

Results and Discussion

Figures 4.7—4.9 are plots of lnK vs. vertical location for the three sections analyzed in this study. In order to aid visualization plots for each of the sections were color coded and graphs for each section were split.

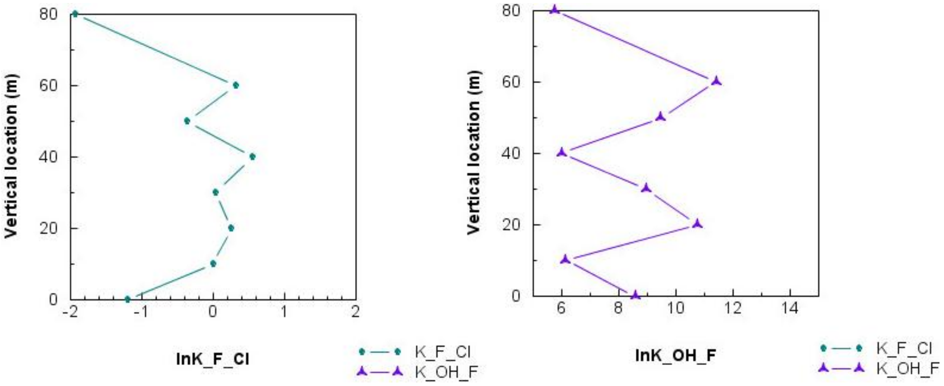

Fig.4.7. Section 1 Cerro Galan lnK values vs. vertical location

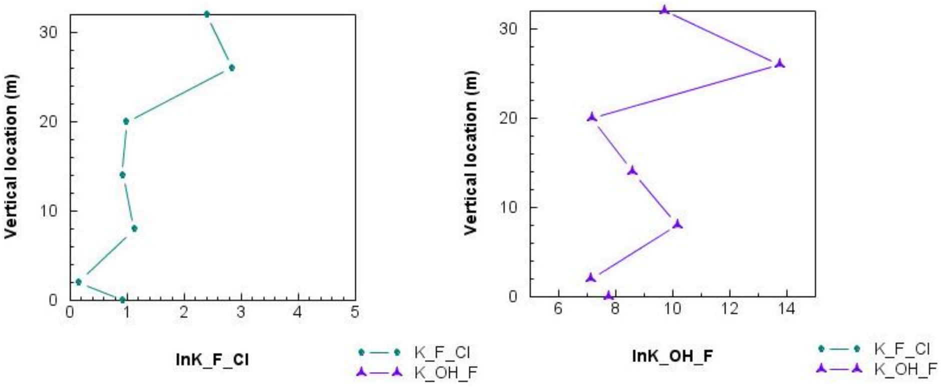

Fig.4.8. Section 2 Cerro Galan lnK values vs. vertical location

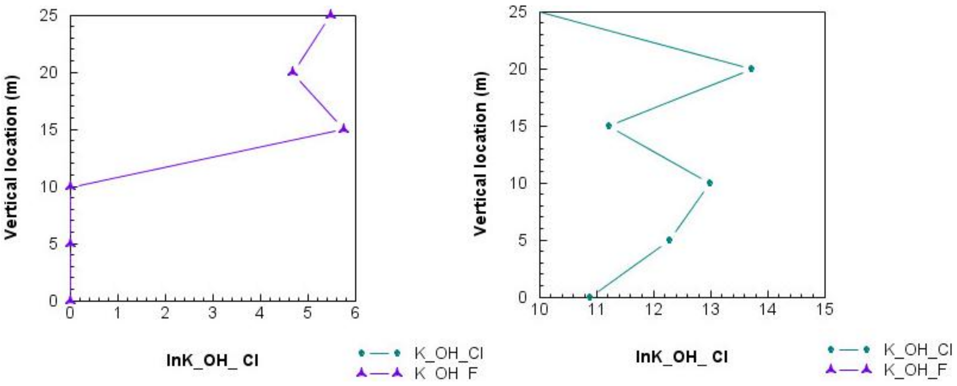

Fig.4.9. Cerro Blanco lnK values vs. vertical location

From figs. 4.7—4. 9 it is observed that the values of the equilibrium constant show great variability. This implies that volatile concentrations obtained in this investigation from apatites and biotites do not represent equilibrium concentrations. As previously mentioned, if the apatites and biotites were at equilibrium lnK values at the different vertical locations would have remained constant within error or would have varied monotonically, reflecting temperature and/or pressure trends in the magma chamber. The variations in the minerals analyzed here most likely reflect post-magmatic alteration; therefore volatile budgets cannot be applied to infer pre-eruptive conditions in the magma chambers of Cerro Galan and Cerro Blanco. This notion is supported by figs. 4.10—4.15 below, which show strong exsolution in the apatites. This exsolution defines what is referred to in this study as alteration.

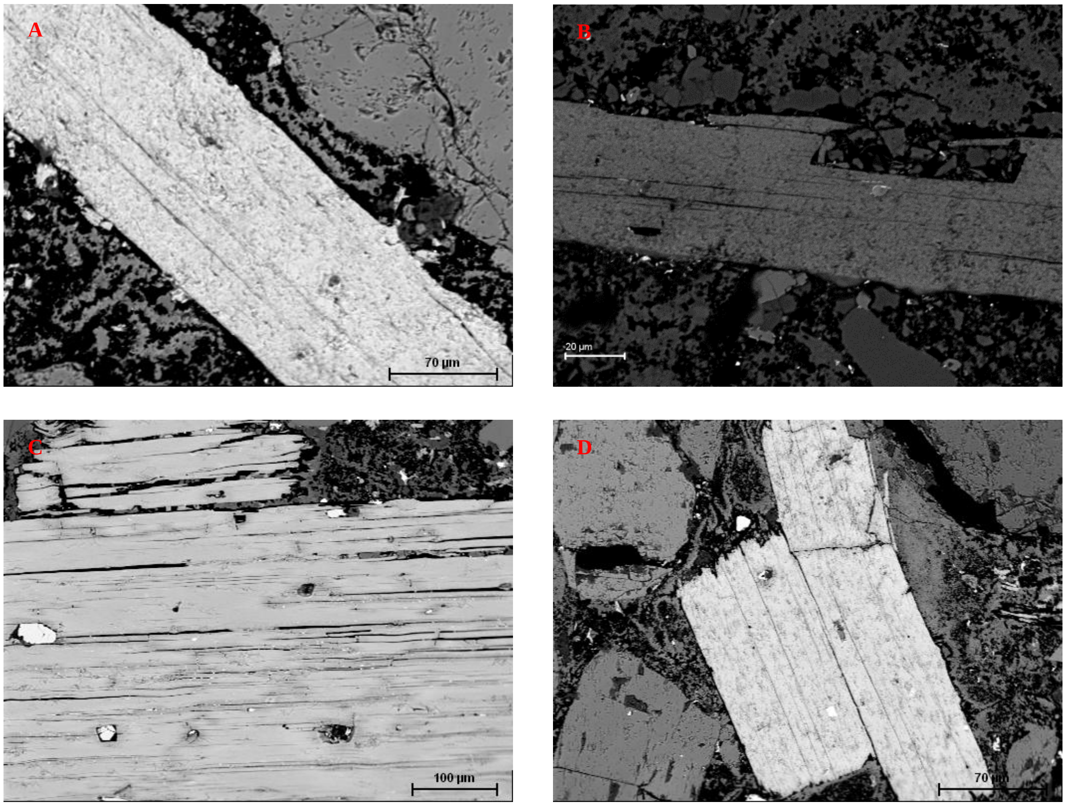

Fig.4.10. Panels A-C are SEM images of altered biotite grains from section 1 of Cerro Galan

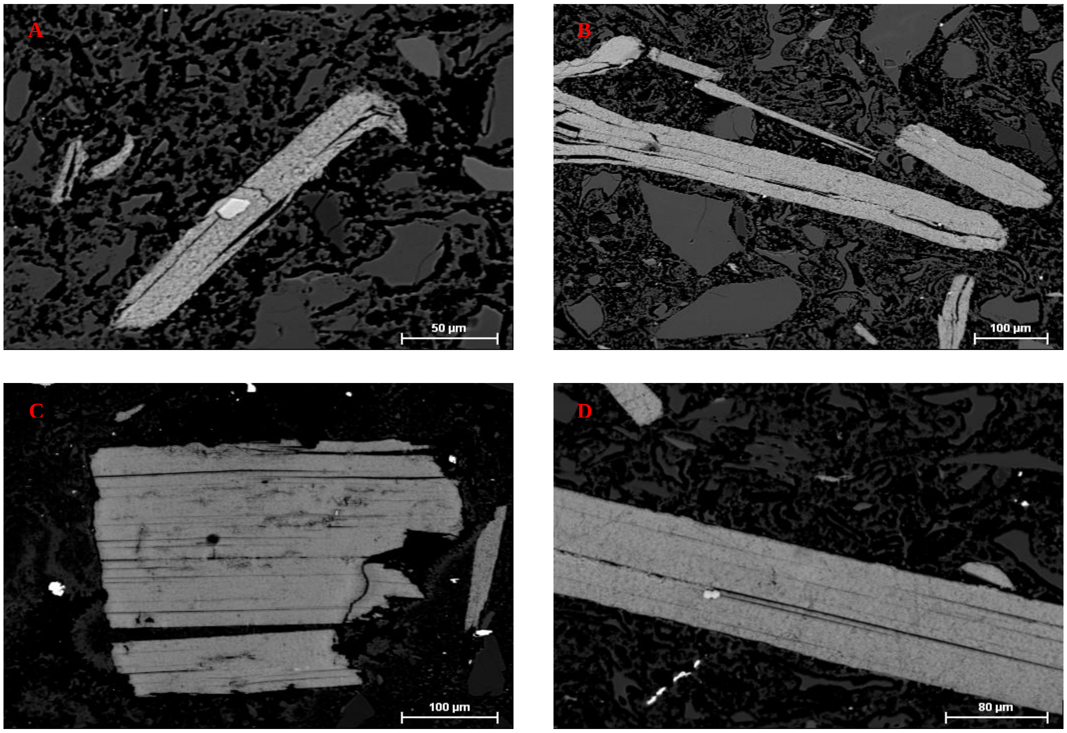

Fig.4.11. Panels A & B are SEM images of altered biotite grains from section 2 of Cerro Galan

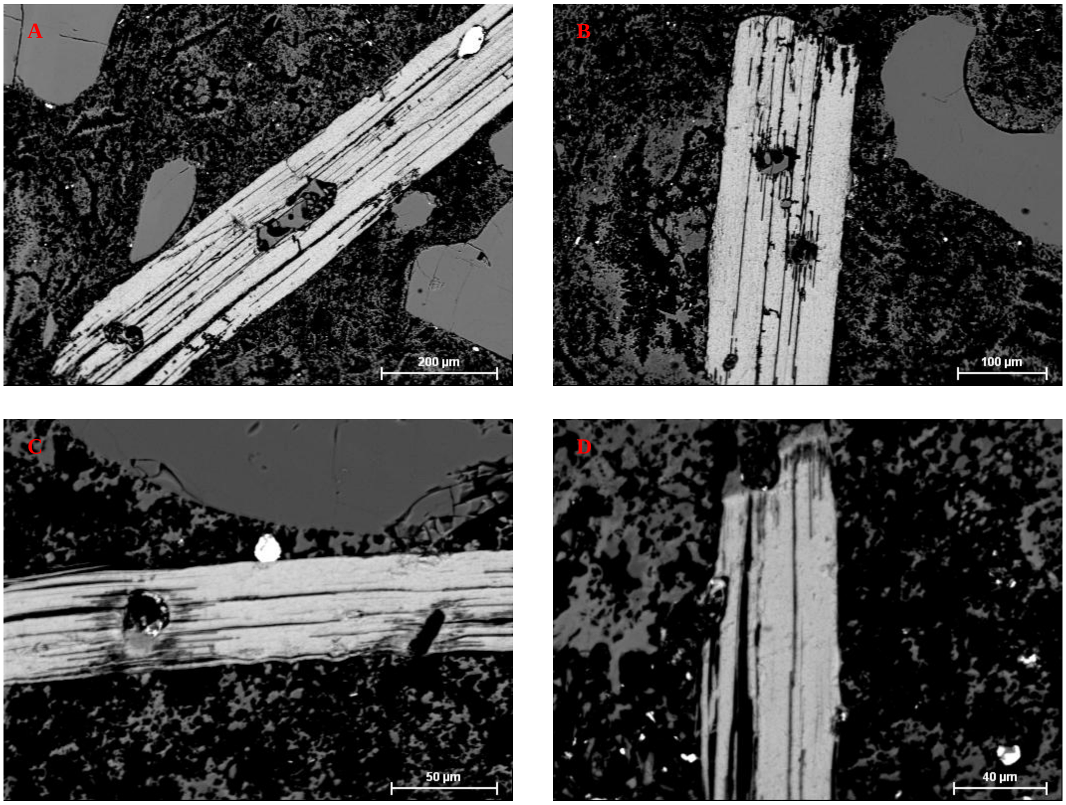

Fig.4.12. Panels A-C are SEM images of altered biotite grains from Cerro Blanco

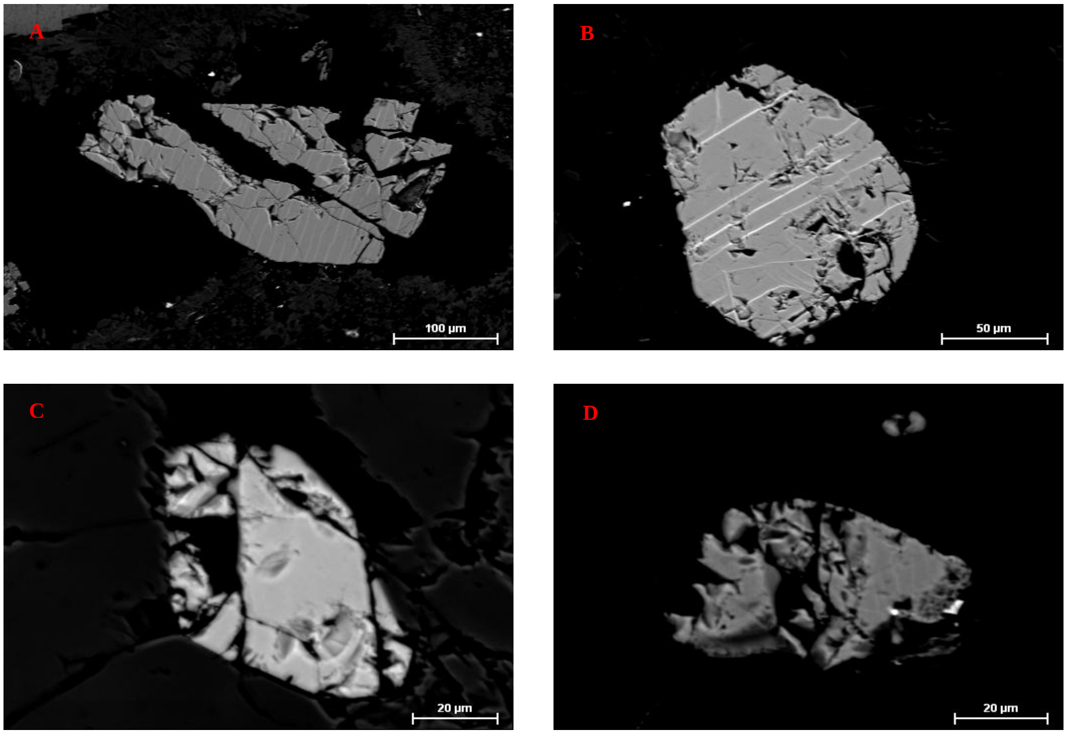

Fig.4.13. Panels A-D are SEM images of exsolved apatite grains from Section 1 of Cerro Galan

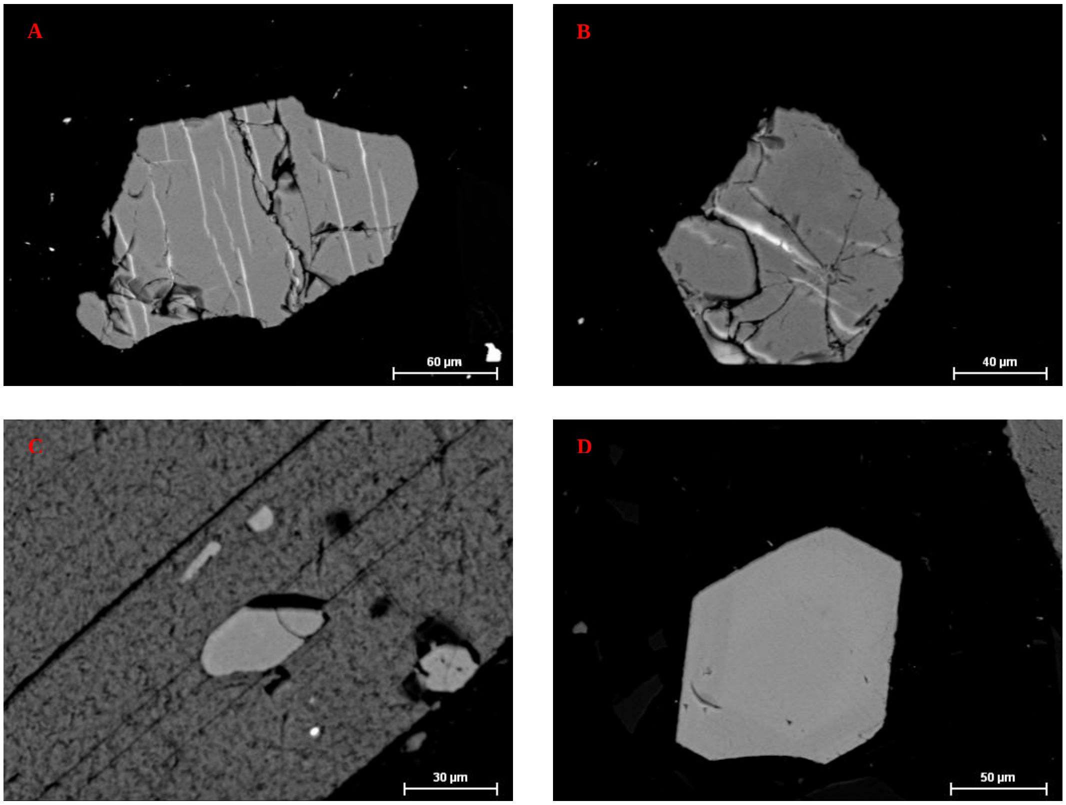

Fig.4.14. Panels A-D are SEM images of exsolved apatite grains from Section 2 of Cerro Galan

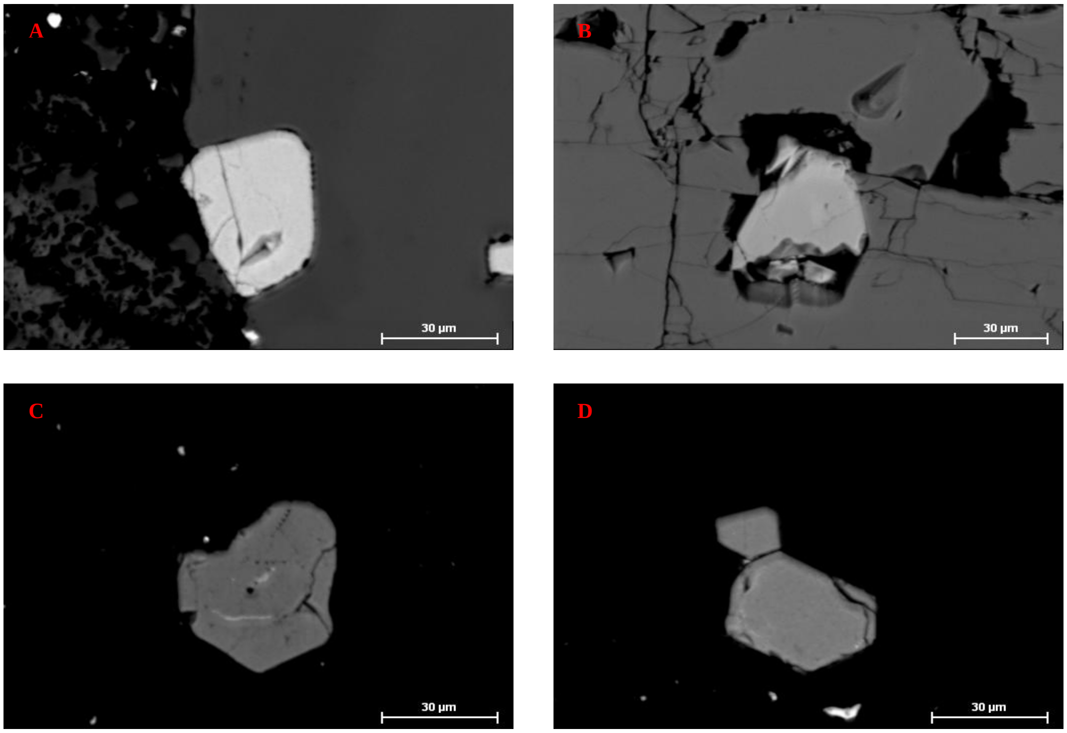

Fig.4.15. Panels A-D are SEM images of exsolved apatite grains from Cerro Blanco

In order to get a better idea of the exsolved phase an X-ray map was obtained by microprobe analysis. This X-ray map is depicted in fig. 4.16 below.

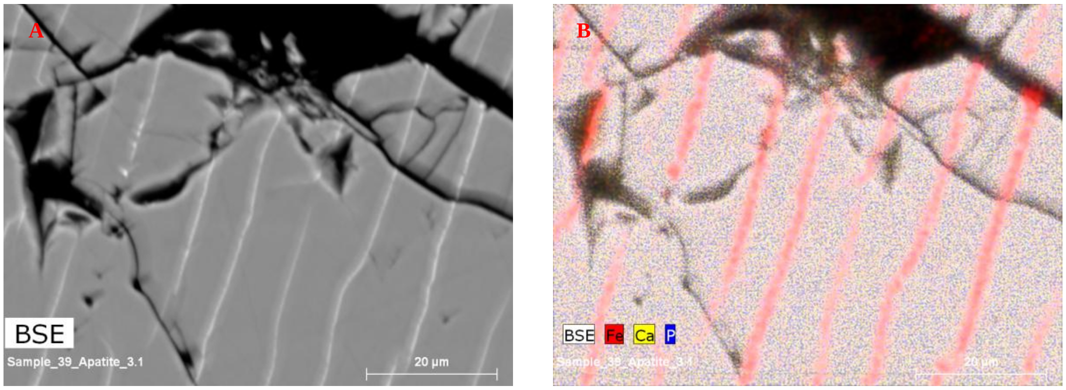

Fig.4.16. Panels A and B are backscatter image and X-ray map respectively from an apatite grain in Section 1 of Cerro Galan

The identity of the exsolved phase was not conclusively determined due to technological limitations. The size of the lamellae is too small compared to the size of electron beam and also the composition of the apatite grain is mixed with the composition of the lamellae when conducting analysis. These factors prevent an unequivocal identification, however, as seen in panel B of fig.4.16 the lamellae are iron rich, possibly indicating exsolution of an Fe-sulfide or Fe-oxide phase.

Volatile budget comparison between Cerro Galan and Cerro Blanco

As suggested by Stormer and Carmichael (1971) and Piccoli and Candela (1994) apatite is more resilient than biotite to subsolidus volatile exchange. These authors indicate that in natural assemblages the mica is more likely to be affected by late-stage exchange at low temperature with aqueous fluids. Based on this, if we assume that apatite retained anion concentrations that reflect conditions close to equilibrium in the magma chambers we can qualitatively compare the anion concentrations of both calderas as a function of vertical location.

This comparison is depicted below in fig. 4.17 (figure 4.17 is simply a side by side comparison of figures 4.1 and 4.3 which are plots for section 1 of Cerro Galan and Cerro Blanco respectively).

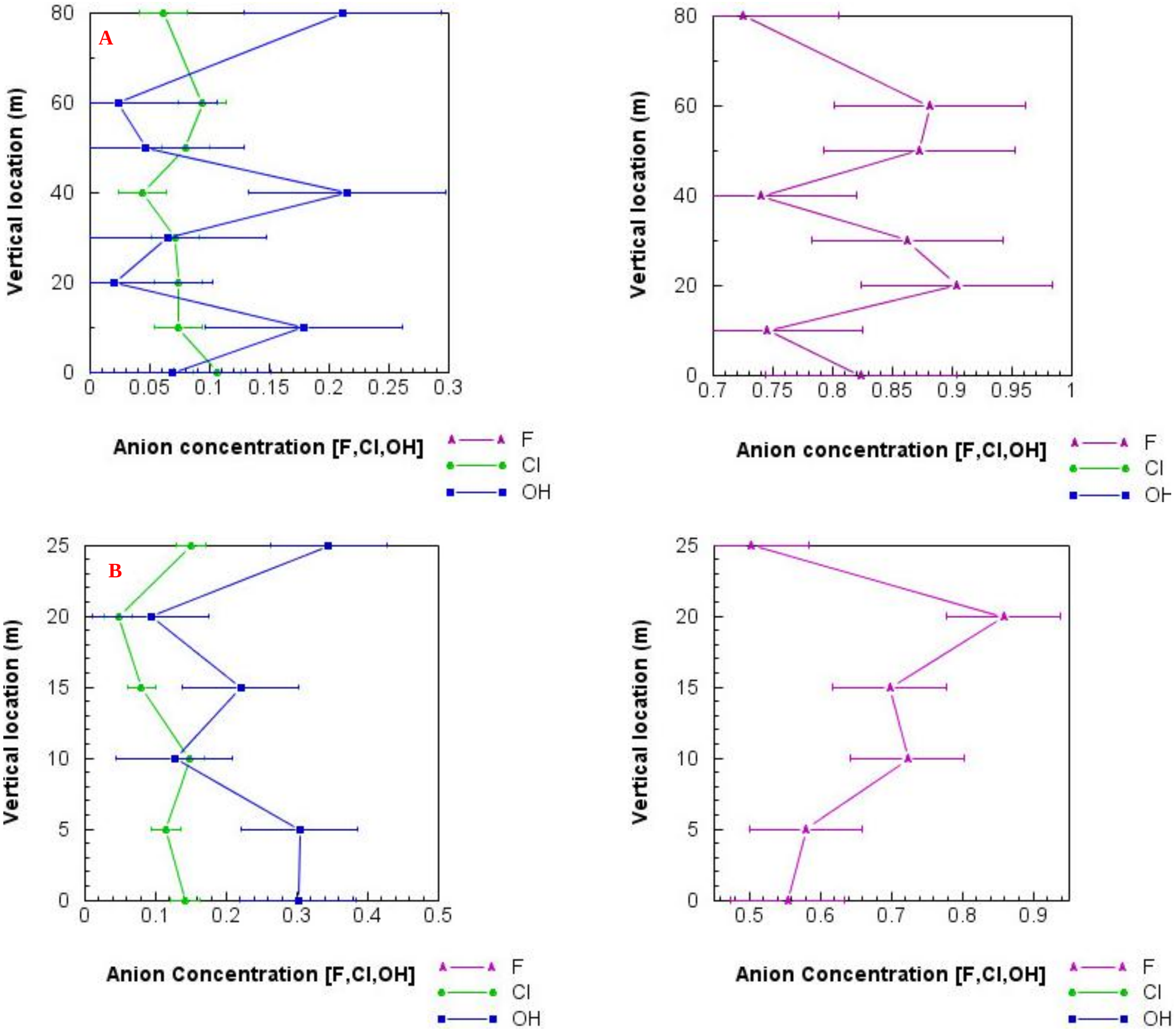

Fig.4.17. Comparison of anion concentrations between (A) Section 1 of Cerro Galan and (B) Cerro Blanco

From fig.4.17 it is observed that the majority of F, Cl, and OH concentrations in both calderas are the same within error. This may suggest that both calderas were under the same conditions prior to eruption and that magma composition in both calderas may have been very similar. This is further supported by the similar magmatic equilibrium temperatures recorded by the feldspars (refer to appropriate section).

Finally, based on the erratic trend seen from plots of volatile concentration vs. vertical location, plots of lnK vs. vertical location and strong exsolution (only present in apatite) it is inferred that apatite and biotite most likely were altered after the emplacement of the CGI and the Cerro Blanco ignimbrite. This alteration is supported by the strong exsolution and erratic trends in compositions seen in the Fe-Ti oxides (see appropriate chapter). Thus, apatite and biotite compositions neither support nor refute the equilibrium conditions for Cerro Galan and Cerro Blanco inferred from feldspar thermometry.

CHAPTER 5

Closing Remarks

In this study halogens vs. vertical location, feldspar thermometry, and Fe-Ti oxide geothermometry were used in order to infer the pre-eruptive conditions in the magma chambers of Cerro Galan and Cerro Blanco. Results indicate that only the feldspars recorded plausible magmatic equilibrium temperatures. Due to their homogeneous appearance, the lack of visible chemical alteration, and the small variation in compositions it is inferred that these phases recorded equilibrium conditions representative of both calderas prior to eruption. Feldspar thermometry indicates that both Cerro Galan and Cerro Blanco sub-volcanic chambers were at a minimum pressure of 2 kb, based on an equilibrium temperature of about 700 ^{0}C and 4% H_2O saturation.

Moreover, based on the abnormally low non-magmatic temperatures obtained from Fe-Ti oxide thermometry, the erratic trends in composition as a function of vertical location, and the strong exsolution in these phases (present mainly in the ilmenite minerals) it is inferred that titanomagnetites and titanohematites investigated in this study were altered to different degrees after the eruption. Similarly, based on the erratic trend seen from plots of volatile concentration vs. vertical location, plots of lnK vs. vertical location, and strong exsolution (only present in apatite) it is inferred that apatite and biotite most likely were oxidized after the emplacement of the CGI and the Cerro Blanco ignimbrite. Thus, Fe-Ti oxides, apatite, and biotite compositions analyzed in this study cannot be used for thermodynamic calculations and the results obtained from the analyses of these minerals neither support nor refute the equilibrium conditions for Cerro Galan and Cerro Blanco inferred from feldspar thermometry.

References

Allmendinger Richard W. et al.., 1997, The evolution of the Altiplano-Puna plateau of the central Andes. Annual Reviews of Earth and Planetary Sciences, Vol. 25, pp 139-174.

Armstrong, J.T., 1988, Quantitative analysis of silicate and oxide materials: comparison of Monte Carlo, ZAF, and phi-rho-z procedures. Microbeam Analysis, 239-246

Boyce, Jeremy W., Hervig, Richard L., 2008, Magmatic degassing histories from apatite volatile stratigraphy. The Geological Society of America, Vol. 36, pp 63-66.

Boyce, Jeremy W., Hervig, Richard L., 2009, Apatite as a monitor of late-stage magmatic processes at Volcan Irazu, Costa Rica. Contributions to Mineralogy and Petrology, Vol. 157, pp 135-145.

Cas, Ray A.F. et al.., 2011, The flow dynamics of an extremely large volume pyroclastic flow, the 2.08-Ma Cerro Galan Ignimbrite, NW Argentina, and comparison with other flow types. Bulletin of Volcanology, Vol. 73, pp 1583-1609.

Deer, FRS W.A., 1992, An introduction to the rock-forming minerals (2nd ed.). Harlow, England: Longman

Elkins, Linda T., Grove, Timothy L., Ternary feldspar experiments and thermodynamic models. American Mineralogist, Vol. 75, pp 544-559.

Folkes, Chris B. et al., 2011, Geochemical homogeneity of a long-lived, large silicic system; evidence from the Cerro Galan Caldera, NW Argentina. Bulleting of Volcanology, Vol. 73, pp 1455-1486.

Francis, P.W. et al., 1989, Petrology and geochemistry of volcanic rocks of the Cerro Galan caldera, northwest Argentina. Geological Magazine, Vol. 126, pp 515-547.

Francis, P.W., Hawkesworth, C.J., 1994, Late Cenozoic rates of magmatic activity in the Central Andes and their relationships to continental crust formation and thickening. Journal of the Geological Society, Vol. 151, pp 845-854.

Frost, Ronald B. 1991. Introduction to oxygen fugacity and its petrologic importance. In Lindsley, Donald

H., Oxide minerals: petrologic and magnetic significance (pp 1-9). Blacksburg, Virginia: BookCrafters, Inc.

Fuhrman, Miriam L. Lindsley, Donald H., 1988. Ternary-feldspar modeling and thermometry. American Mineralogist, Vol. 73, pp 201-215

Ghiorso, Mark S., Evans, Bernard W., 2008, Thermodynamics of rhombohedral oxide solid solutions and revision of the Fe-Ti two-oxide gothermometer and oxygen-barometer. American Journal of Science, Vol. 308, pp 957-1039.

Ghiorso, M.S., Sack, R.O., 1991. Thermochemistry of the oxide minerals. In Lindsley, Donald H., Oxide minerals: petrologic and magnetic significance (pp 221-262). Blacksburg, Virginia: BookCrafters, Inc.

Goff, Fraser., Shevenell, Lisa., 1987, Travertine deposits of Soda Dam, New Mexico, and their implications for the age and evolution of the Valles caldera hydrothermal system. Geological Society of America Bulletin, Vol. 99, pp 292-302.

Harrison, Richard J. et al., 2000, Thermodynamics of the R3 to R3c phase transition in the ilmenite-hematite solid solution. American Mineralogist, Vol. 85, pp 1694-1705.

Hokada, Tomokazu, 2001, Feldspar thermometry in ultrahigh-temperature metamorphic rocks: evidence of crustal metamorphism attaining 1100 ^{0}C in the Archean Napier Complex, East Antarctica. American Mineralogist, Vol. 86, pp 932-938

Holland, T.J.B., Powell, R., 1998, An internally consistent thermodynamic data set for phases of petrologic interest. Journal of Metamorphic Geology, Vol. 16, pp 309-343.

Isacks, Brian L., 1988, Uplift of the Central Andean plateau and bending of the Bolivian orocline. Journal of Geophysical Research, Vol. 93, pp 3211-3231.

Lesti, Chiara., et al., 2011, High-temperature emplacement of the Cerro Galán and Toconquis Group ignimbrites (Puna plateau, NW Argentina) determined by TRM analyses. Bulletin of Volcanology, Vol. 73, pp 1535-1565.

Liu, Yang., Zhang, Youxue., Harald, Behrens., 2005, Solubility of H2O in rhyolitic melts at low pressures and a new empirical model for mixed H2O–CO2 solubility in rhyolitic melts. Journal of Volcanology and Geothermal Research, Vol. 143, pp 219– 235.

Mathez, Edmond A., Webster, James D., 2004, Partitioning behavior of chlorine and fluorine in the system apatite-silicate melt-fluid. Geochimica et Cosmochimica Acta, Vol. 69, pp 1275-1286.

Nekvasil, Hanna, 1994, Ternary feldspar/melt equilibria: a review. NATO Advanced Study Institute Series C: Mathematical and Physical Sciences, volume 421, pp 195-219
Ternary feldspar/melt equilibria: a review

Patino Douce, Alberto E., Roden, Michael., 2006, Apatite as a probe of halogen and water fugacities in the terrestrial planets. Geochimica et Cosmochimica Acta, Vol. 70, pp 3173-3196.

Patino Douce, Alberto., 2011, Thermodynamics of the earth and planets. Cambridge, New York: Cambridge University Press.

Piccoli, Philip., Candela, Philip., 1994, Apatite in felsic rocks: a model for the estimation of initial halogen concentrations in the Bishop Tuff (Long Valley) and Tuolumne intrusive suite (Sierra Nevada Batholith) magmas. American Journal of Science, Vol. 294, pp 92-135.

Piccoli, Philip., Candela, Philip A., 2002, Apatite in igneous systems. Reviews in Mineralogy and Geochemistry, Vol. 48, pp 255-292.

Sarafian, Adam R., 2012, Apatite as a tool to determine the volatile content of eucrite meteorites (Master's thesis). The University of Georgia, Athens, GA.

Schrader, Christian M., 2009, Petrology and F and Cl systematics of Rattlesnake Mountain and Bone Srings sills, Trans-Pecos magmatic province, Texas (Doctoral dissertation). The University of Georgia, Athens, GA.

Skewes, Alexandra M., Stern, Charles R., 1995, Genesis of the giant late Miocene to Pliocene copper deposits of Central Chile in the contest of Andean magmatic and tectonic evolution. International Geology Review, Vol. 37, pp 893-909.

Sparks, R.S.J. et al., 1985, Ignimbrites of the Cerro Galan Caldera, NW Argentina. Journal of Volcanology and Geothermal Research, Vol. 24, pp 205-248.

Stormer, J.C., Carmichael, I.S.E., 1971, Fluorine-hydroxyl exchange in apatite and biotite: a potential igneous geothermometer. Contributions to Mineralogy and Petrology, Vol. 31, pp 121-131.

Winter, John D., 2001, Principles of igneous and metamorphic petrology (2nd ed). Upper Saddle River, New Jersey: Prentice Hall.

Wright, Heather M.N., et al., 2011, Columnar jointing in vapor-phase-altered, non-welded Cerro Galan Ignimbrite, Paycuqui, Argentina. Bulleting of Volcanology, Vol. 73, pp 1567-1582.

Zoltai, Tibor., Stout, James H., 1984, Mineralogy: concepts and principles. Minneapolis, Minnesota: Burgess Publishing Company.